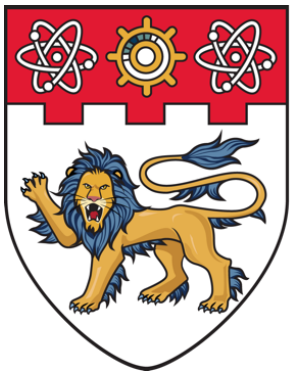

NANYANG TECHNOLOGICAL UNIVERSITY
SINGAPORE

Toroidal Resonances in Terahertz Metamaterials

Manoj Gupta

SCHOOL OF PHYSICAL AND MATHEMATICAL SCIENCES

2019

Toroidal Resonances in Terahertz Metamaterials

Manoj Gupta

SCHOOL OF PHYSICAL AND MATHEMATICAL SCIENCES

A thesis submitted to the Nanyang Technological University in partial fulfilment of the requirement for the degree of Doctor of Philosophy

2019

Statement of Originality

I hereby certify that the work embodied in this thesis is the result of original research done by me except where otherwise stated in this thesis. The thesis work has not been submitted for a degree or professional qualification to any other university or institution. I declare that this thesis is written by myself and is free of plagiarism and of sufficient grammatical clarity to be examined. I confirm that the investigations were conducted in accord with the ethics policies and integrity standards of Nanyang Technological University and that the research data are presented honestly and without prejudice.

. . .21-12-2018 . . . . .
Date

. . . . . .
Manoj Gupta

Supervisor Declaration Statement

I have reviewed the content and presentation style of this thesis and declare it of sufficient grammatical clarity to be examined. To the best of my knowledge, the thesis is free of plagiarism and the research and writing are those of the candidate's except as acknowledged in the Author Attribution Statement. I confirm that the investigations were conducted in accord with the ethics policies and integrity standards of Nanyang Technological University and that the research data are presented honestly and without prejudice.

. . . .21-12-2018 . . . .
Date

. . . . . Ranjan Singh . . . . . .
Prof. Ranjan Singh

Authorship Attribution Statement

This thesis contains material from 4 paper(s) published in the following peer-reviewed journal(s) where I was the first author.

Chapter 3 is published as M. Gupta, V. Savinov, N. Xu, L. Cong, G. Dayal, S. Wang, W. Zhang, N. I. Zheludev, and R. Singh, "Sharp Toroidal Resonances in Planar Terahertz Metasurfaces", *Advanced Materials*, 28(37), 8206-8211 (2016). DOI:10.1002/adma.201601611

This chapter also includes the conference paper published as M. Gupta, V. Savinov, N. Xu, L. Cong, G. Dayal, S. Wang, W. Zhang, N. I. Zheludev, and R. Singh, "Planar Toroidal Metamaterials", *2016 International Conference on Optical MEMS and Nanophotonics (OMN)*, Singapore, 2016. DOI: 10.1109/OMN.2016.7565896

The contributions of the co-authors are as follows:

- Prof. N. I. Zheludev, Prof. Weili Zhang provided the initial project direction.
- I prepared the manuscript drafts. The manuscript was revised by Dr Longqing Cong, Dr. Vassili Savinov and Dr. Shuang Wang.
- I, together with Dr. Ningning Xu, Dr Govind Dayal and Dr. Vassili Savinov developed Matlab codes for multipole analysis.
- All microscopy, including sample preparation, was conducted by me in the Facility for Analysis, Characterization, Testing and Simulation.
- Prof. Ranjan Singh supervised the whole work and edited the manuscripts drafts.

Chapter 4 is published as M. Gupta, and R. Singh (2016), "Toroidal versus Fano Resonances in High Q planar THz Metamaterials", *Advanced Optical Materials*, 4(12), 2119-2125 (2016). DOI:10.1002/adom.201600553.

The contributions of the co-authors are as follows:

- I conceived the idea and prepared the manuscript drafts. All microscopy, including sample preparation, was conducted by me in the Facility for Analysis, Characterization, Testing and Simulation.

- Prof. Ranjan Singh supervised the whole work and edited the manuscripts drafts.

Chapter 5 is published as M. Gupta, Y. K. Srivastava, and R. Singh, "A Toroidal Metamaterial Switch", *Advanced Materials*, 30(4), 1704845 (2018). DOI:10.1002/adma.201704845.

The contributions of the co-authors are as follows:

- I conceived the idea and prepared the manuscript drafts.
- Dr. Yogesh Kumar Srivastava assisted me in sample fabrication, and in revising manuscripts.
- All microscopy was conducted by me in the Facility for Analysis, Characterization, Testing and Simulation.
- Prof. Ranjan Singh supervised the whole work and edited the manuscripts drafts.

Chapter 6 is published as M. Gupta, Y. K. Srivastava, M. Manjappa, and R. Singh, "Sensing with toroidal metamaterial", *Applied Physics Letters*, 110(12), 121108 (2017). DOI:10.1063/1.4978672.

The contributions of the co-authors are as follows:

- I conceived the idea, did simulations and prepared the manuscript drafts.
- Dr. Yogesh Kumar Srivastava assisted me in sample fabrication, and in revising manuscripts.
- Dr. Manukumara Manjappa assisted me in sample characterization, and in revising manuscripts.
- Prof. Ranjan Singh supervised the whole work and edited the manuscripts drafts.

. . 21-12-2018. . . . . Manoj Gupta

Date

. . . . . .

Manoj Gupta

Abstract

Toroidal modes are unique type of electromagnetic excitations that have characteristic features different from the conventional electric and magnetic multipoles. At terahertz regime, metamaterial allows an effective way to introduce toroidal excitations, as they give flexibility in tailoring loss channels which are important for modulation, sensing, and spectroscopic applications. This thesis focuses on the near field toroidal coupling of neighboring resonators in metamaterials, and its implications on device performance at terahertz frequencies.

The introduction of toroidal dipole coupling in planar metasurface excites sharp resonances, which are of high quality factor compared to resonances of well-known planar metamaterials designs at terahertz frequencies. The experimental advantage of toroidal coupling could be seen directly in case of metasurface array of asymmetric Fano resonators, where significant line narrowing together with high figure of merit is achieved by mirroring neighboring resonators in metasurface array. This approach of near field coupling through toroidal excitations enhance device performance, which is an essential criterion for the practical implementation of metadevices.

Metamaterial devices containing mirrored configuration of adjacent resonators allows active tuning of near field coupling through selective inclusion of active elements. This near field coupling could be actively switched "on" and "off" upon optical pumping, which changes the nature of electromagnetic excitation of metasurface from toroidal dipole to electric or magnetic dipole. The excitation features of toroidal dipole are always masked by dominant electric and magnetic multipoles, which are simultaneously excited in resonating elements with toroidal topology. In this regard, multipole analysis provides a numerical approach to investigate the contribution due to different multipoles, and in estimating near field toroidal coupling. Moreover, the near field toroidal coupling is sensitive to nearby environment. We have demonstrated sensing capability of toroidal metasurface for few hundred nanometers thick dielectric layers on the top of metasurface.

Future prospect of the conducted studies can be used to incorporate low loss materials with ultrafast dynamics in a recently developed planar toroidal metasurface to effectively suppress the radiative losses, as well as in switching the near field toroidal coupling on ultrafast time scales thereby lead to low-loss, ultrasensitive, frequency agile, switchable quantum photonics devices.

Acknowledgements

First and foremost, I would like to thank my adviser Professor Ranjan Singh, who guided my journey of PhD showing a lot of patience, support, and trust. Thanks for instilling confidence in me and inspiring for perfection along the way. It has been a privilege working with you. Sincere gratitude to my thesis advisory committee members Prof. Zhang Baile and Prof. Wang Qijie for their direction during the course of my thesis. I would like to acknowledge Prof. Nikolay Zheludev for providing the well-equipped environment and state-of-art facilities at the Center for Disruptive Photonic Technologies (CDPT). I also duly acknowledge all the faculty members associated with Department of Physical and Mathematical Sciences (SPMS) for the interesting sessions, discussions and support, which helped in shaping up this thesis. Just as importantly, I want to thank my parents for always standing with me and showing continuous support throughout my journey. Your values and wisdom have shaped up every aspect of my life. To my dear wife Ranjana, for your constant love and all the sacrifices you made for me along this journey. This couldn't have been possible without you. To Shashank, my son for being an epitome of happiness for me. To one of my best friend Rakesh for standing with me in all times. I extend my sincere thanks to Dr. V. Savinov, Dr. Sreekanth, Dr. Prakash, Dr. Longqing, Dr. M. Manjappa, Dr. Lim Wen Xiang, Dr. Govind, Dr. Yogesh, Han Song, Abhishek, Thomas and Piyush for their encouraging and fruitful inputs in the research area. Last but not the least, a huge thank to all my friends and well-wishers: Manish, Sandeep, Pankaj, Argh and many, many more. Thank you, I look back with great fondness upon the times we have shared.

Table of Content

Table of Figures

List of Tables

Chapter 1

Introduction

1.1 Introduction to metamaterials

Electromagnetic waves have facilitated realization of state-of-the-art techniques, such as enhancing optical activity, stimulating nonlinearity, and holography, by exploiting the novel features of naturally existing or artificially designed materials.[1-4] Frequency dependent electromagnetic properties could be used for optical imaging, or in introducing birefringence in crystals, or in probing free carrier absorption and transport properties of semiconducting materials.[5-9] Propagation of electromagnetic wave in a medium is determined by Maxwell equations, which are governed by the effective permittivity and permeability of medium. Following section introduces brief discussion in this context where different class of materials have been distinguished on the basis of permittivity and permeability of the medium.

In general, the response of an incident electromagnetic wave in a material medium is governed by the Maxwell's equation:

$$\vec{\nabla}.\vec{D} = \rho \qquad \ldots\ldots\ldots 1.1\ (a)$$

$$\vec{\nabla}.\vec{B} = 0 \qquad \ldots\ldots\ldots 1.1\ (b)$$

$$\vec{\nabla} X \vec{E} = -\frac{\partial \vec{B}}{\partial t} \qquad \ldots\ldots\ldots 1.1\ (c)$$

$$\vec{\nabla} X \vec{B} = \mu \vec{J} + \epsilon\mu \frac{\partial \vec{E}}{\partial t} \qquad \ldots\ldots\ldots 1.1\ (d)$$

where $\vec{E}$ and $\vec{B}$ are the electric field intensity and magnetic flux density, respectively, while ϵ and μ represents the relative permittivity and permeability of medium. The current density and volume charge density induced in medium in presence of electromagnetic waves are represented by $\vec{J}$ and ρ. Any material medium could be classified in four categories, based on the effective permittivity (ε) and effective permeability (μ) of medium. Figure 1.1 shows ε-μ diagram, which indicates the behaviour of any material medium depending on the positive or negative values of both ε and μ.[10] First quadrant of ε-μ diagram represents region where both $\varepsilon > 0$ and $\mu > 0$, which corresponds to right-handed medium as the electromagnetic radiation could propagate through these medium (forward wave propagation). Most of the dielectrics, and metals above plasma frequency fall in this category. Second quadrant represents the region where $\varepsilon < 0$ and $\mu > 0$, which indicates that electromagnetic radiation decay evanescently and no propagation could be sustained inside the medium. Metals and doped semiconductor below plasma frequency (minimum frequency of EM wave that could travel through plasma without attenuation) fall in this category. Similarly, forth quadrant again represents region of evanescent electromagnetic wave as $\varepsilon > 0$ and $\mu < 0$ in medium (ferrite materials). Metamaterials response to electromagnetic radiation falls in third quadrant of ε-μ diagram where both $\varepsilon < 0$ and $\mu < 0$.[11] As a consequence of negative value of both ε and μ, these mediums exhibit unusual electromagnetic properties, such as negative refraction, backward wave propagation, which are not found in naturally existing materials.

Metamaterials are array of artificially designed structures to excite desired electromagnetic response in the entire range of frequency spectrum.[12-14] In contrast to naturally existing material, the constituent blocks of metasurface are known as meta-atoms.[15] Each meta-atom also corresponds to one unit cell which could be repeated in 2D or 3D space to give planar or three

dimensional metasurface.[16,17] Each meta-atom corresponds to one resonator that resonates at some specific frequency of electromagnetic radiation, unit cell containing more than one resonator are known as meta-molecules. The electromagnetic properties of metamaterial arises due to geometry of individual resonator in unit cell of metasurface. These resonators are sub-wavelength in nature, and their shape and design parameters could be

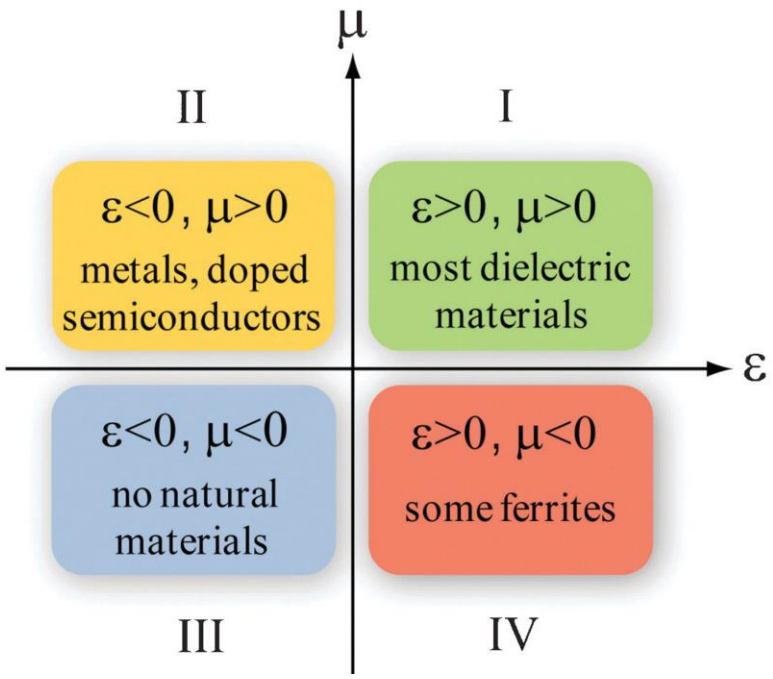

Figure 1.1: Material classification based on the effective permittivity (ε) and permeability (μ) of medium.[10]

tailored to excite electromagnetic response at frequencies ranging from microwave, infrared to optical regime.[18] Due to subwavelength nature of individual resonator entire metasurface behaves as a homogeneous medium with respect to incoming radiation.[19] At macroscopic level, this allows us to characterize the composite medium in terms of frequency dependent electric permittivity ε(ω) and magnetic permeability μ(ω) of the metasurface.[20]

The word 'Metamaterial' has widely grown in research community over the years, but historically they were no known terminologies for these kinds of artificial medium. In 1898, J. C. Bose demonstrated polarization rotation at microwave by a twisted-jute structure (see figure

1.2a), which in today's terminology is known as artificial chiral material.[21] He was also able to realize polarizer by inserting tinfoil between the book pages (see figure 1.2b). Later in 1968, V. G. Veselago theoretically predicted Snell's law reversal for materials with simultaneously negative values of ε and μ.[22] He termed these theoretically predicted materials as negative index material, which are also known as left-handed material (LHM). The real breakthrough was made in 1996 by J. B. Pendry for physical realization of electric and magnetic plasmas in array of thin metallic (see figure 1.3a) wires at microwave frequency.[23] He also demonstrated effective negative permittivity and permeability below plasma frequencies by array of split-ring resonators (see figure 1.3b).[24] In 2001, using composite structure of split-ring resonators and thin wires (see figure 1.3c), D. R. Smith first experimentally realized negative refractive index.[25,26] Since then the field of metamaterials and plasmonics is tremendously getting developed in understanding, designing and realizing potential applications.[12,27,28]

Figure 1.2: Artificial material medium demonstrate by J. C Bose. a) Twisted-jute polarizer for polarization rotation, b) Linear polarizer consisting of a book pages interleaved with tinfoils.

The extraordinary advantage of these subwavelength structures is to capture and control the near field electromagnetic interaction, which devised several uncommon phenomena such as cloaking, sub-wavelength imaging, bio sensing, super lens and perfect absorption.[29-34] Over the

time, advanced fabrication techniques and cutting-edge technologies have been developed, which could be used to incorporate many exotic features, such as ultrafast dynamics, active tuning of resonance, that makes metamaterials an ideal platform for exploring light matter interaction.[35-37] Moreover, artificially engineered metal or dielectric interfaces could be prepared to stimulate unconventional electromagnetic phenomena's such as electromagnetically induced transparency (EIT), super lensing effects, negative refractive index, and wavelength selective absorption.[38-40] Metamaterial excites a specific electromagnetic response which could be coupled to different material medium to study about the phonon modes by enhanced light matter interaction, or could be used to sense a nearby environment, or could be used to generate non-linear effects, or could be used in the development of flat optics and lasing devices.[41-44] The capability of metamaterial device to capture and highly localize the income electromagnetic energy would really facilitate in building high performance electro-optic devices in near future. The underlying features of metamaterial lie in their geometry and size, rather than the composition of constituent materials

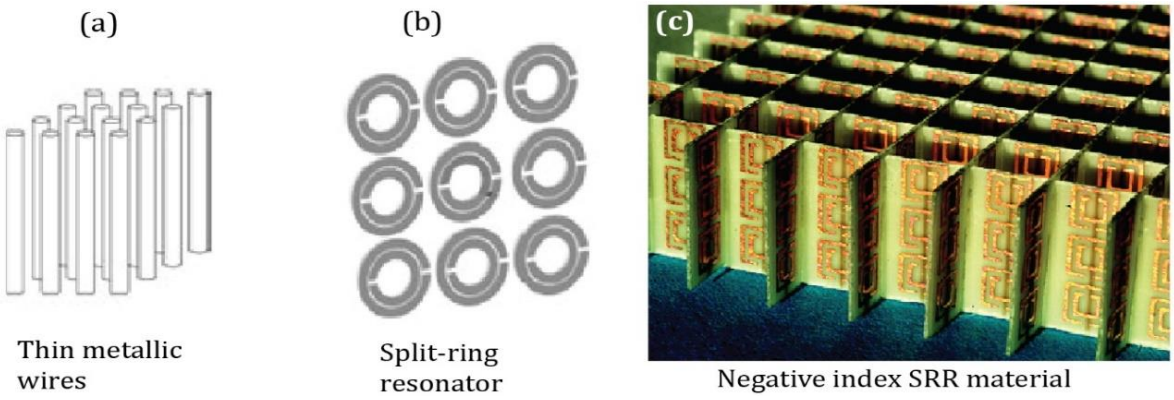

Figure 1.3: Historic breakthrough in field of metamaterials. Array of a) thin metallic wires, b) slit-ring resonator by J. B. Pendry, and c) negative index SRR material demonstrated by D. R. Smith.[25]

from which they are fabricated. The performance of any metamaterial device is affected by the radiative and non-radiative losses, which they encounter under electromagnetic excitation.[45,46]

Non-radiative losses are inherited loss due to frequency dependent material conductivity, which increases as we move from lower to higher frequencies. For metals, which are highly conducting in nature, non-radiative losses increase with increase in frequency because the skin-depth for non-radiative losses increase with increase in frequency because the skin-depth for electromagnetic radiation decreases. This confine large number of carriers to move in a small cross section, leading to increase in carrier scattering responsible for non-radiative loss. Recently, focus has been shifted to high index dielectric metamaterials, because they lack free carrier density which governs non-radiative loss.[47,48] All the works incorporated in this thesis have been demonstrated by metallic metasurfaces at terahertz frequencies. Owing to extremely high conductivity of metals at terahertz frequencies, the non-radiative losses are relatively insignificant, and the need for minimizing radiative loss becomes critical.[49] On the other hand, radiative loss channel depends on the shape and size of subwavelength structures in metasurface, which could be tailored by altering the geometrical parameters. Tailoring the radiative loss channel, which is due to coupling between metamaterial and free space, is of great importance that could be used for many novel applications. For instance, broad resonance that scatters strongly is used as antenna or for signal enhancement in MRI.[50,51] Alternatively, narrower linewidth resonance could be used as dielectric sensor or as a probe to explore resonant light-matter interaction in coupled system.[52] Further, to investigate the radiative loss channel electromagnetic excitation could be understood in terms of multipole analysis.

Multipole analysis is a powerful tool to understand electromagnetic scattering by the resonant structures in the unit cell of metasurface array. Theoretically, the overall electromagnetic scattering of any resonator could be listed as a set of multipoles that individually contribute to scattering. Generally, the dynamic electric and magnetic response of an object is seen in terms of dipole, quadrupole, octupole etc., which are considered during multipole analysis. By engineering the subwavelength resonator, one could manipulate the electromagnetic response

to be dominated by a specific multipole. For instance, two electric dipoles resonator in unit cell of metasurface could be tailored in such a manner that their radiation pattern interferes destructively to minimize the radiation loss. Section 1.3 gives an overview to different multipoles, which are important to analyses the near-field coupling and far-field radiation pattern of metasurface. Following section introduces the history of toroidal dipole and briefly discusses the static and dynamic nature of toroidal dipole excitation.

1.2 Introduction to toroidal dipole moment

Formerly, in the theory of electromagnetism, electric and magnetic moments had been considered independent family members of multipole. For long time, toroidal excitations have not been probed in the multipole expansion. In 1957, Y. Zel'dovich theoretically studied that due to weak interaction elementary particles violate parity symmetry and predicted that Dirac particle with spin-$\frac{1}{2}$ must have an 'anapole moment', which is also known as quantum toroidal dipole moment.[53] Later, in early 1970s, Dubovik et al. extended the quantum explanation of 'anapole', in the field of classical electrodynamics by establishing the term 'polar toroidal moments'.[54] The word 'Toroidal' comes from current distribution in form of circular coils known as 'toroid coil'. The toroidal dipole is the first member of toroidal multipole family, which as per their nature could be classified as magnetic (polar) or electric (axial) toroidal dipole moments. Figure 1.4 shows the pictorial representation of electric, magnetic and toroidal dipole, in terms of fundamental charge current distribution. Two separated opposite charges of equal magnitude gives electric dipole moment ($\vec{p}$ in figure 1.4a), while circular current distribution gives rise to magnetic dipole moment ($\vec{m}$ in figure 1.4b). Circular current symmetrically arranged on the surface of torus forms closed loop head to tail alignment of magnetic dipoles, known as polar toroidal dipole moment ($\vec{t}$ in figure 1.4c), while closed loop

head to tail arrangement electric dipoles forms axial toroidal dipole moment ($\vec{g}$ in figure 1.4d). Polar and axial toroidal dipole moment points upward i.e. perpendicular to the plane of circulating current density (figure 1.4c) and circular arranged electric dipoles (figure 1.4d). Several works have been done in this direction to establish the theoretical framework of toroidal electrodynamics, and it has been predicted that many exotic phenomena can be demonstrated using toroidal dynamics, such as non-reciprocal interaction, non-radiating charge- current distribution, parity-violation in atomic spectra.[55-58] Electric toroidal moments effects could be produced by magnetic charge currents distribution, conversely magnetic toroidal moments effects could be produced by electric charge currents distribution. However, the non-existence of magnetic charge current electric (axial) toroidal dipole moments are not considered in multipole analysis. Depending on charge current dynamics toroidal dipole moments could be further categorized as static and dynamic toroidal moments.

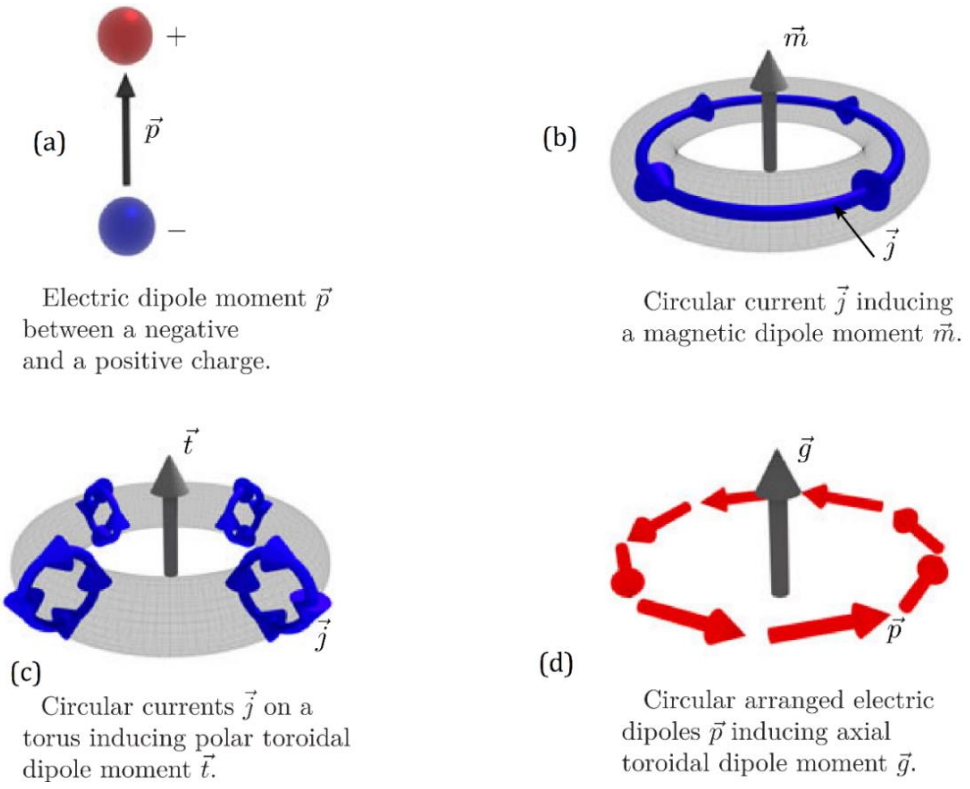

Figure 1.4: Basic charge-current distribution generating a) electric, b) magnetic c, d) polar and axial toroidal moments. [59]

1.2.1 Static toroidal dipole moment

Static currents circulating on the surface of imaginary torus is referred to static toroidal dipole. Y. Zel'dovich studied them in context of atomic, nuclear and solid-state physics (see figure 1.5).[53] As shown in figure 1.5, toroidal topology or torus have been identified in naturally or artificially occurring objects. These static currents establish a constant magnetic field inside torus, while fields outside torus is ideally zero. Since there is no electromagnetic radiation from static toroidal dipole, so they are also termed as anapole, hence they do not directly interact with electric and magnetic fields.[53,60] In 1946, Charles Kittle theoretical work on ferromagnetic domains first investigated toroidal ordering of small particles in solid state, later followed by many observations which confirmed the presence of static toroidal moments.[61-63] Ferrotoroids, medium that contains density of toroidal dipoles, can break inversion symmetry in space and time-reversal symmetry. Ferrotoroids could be electrically or magnetically polarized in presence of an external magnetic or electric field, as well as they are expected to manifest unique nature of magnetic response, and nonreciprocal dichroism and reflection.[64-66] The magnetoelectric response of ferrotoroids is believed to be applied in the areas of data storage where extrenal electric field is applied to write or read information in magnetic medium.

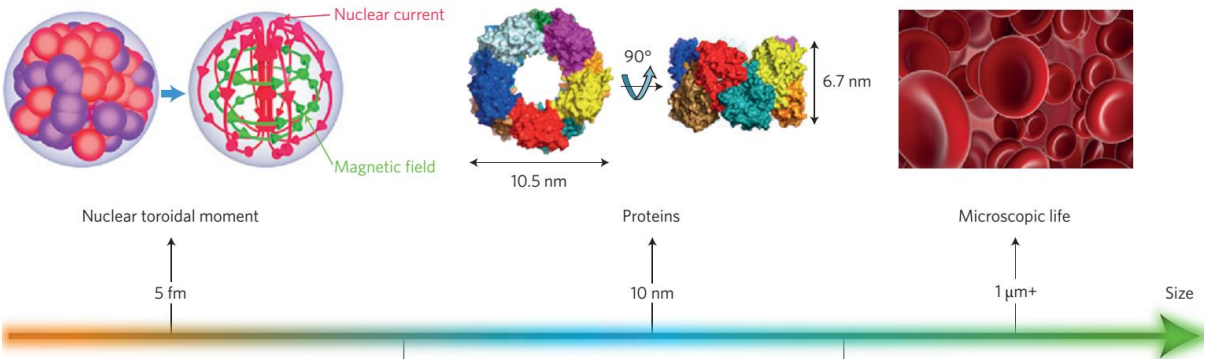

Figure 1.5: From left to right: Solenoidal currents in atomic nucleus leads to toroidal moments, proteins and blood cells takes torus like shape.[53,69]

Varoius inorganic compounds such as pyroxenes, boracites, olivines, are under study which exhibits the signature of static toroidal topology.[63,67,68] Observation of long-range order of static toroidal dipoles have proven to be challenging because of their weak interacting nature.

1.2.2 Dynamic toroidal dipole moment

In contrast to static current density flowing on the surface of torus along its meridians, dynamic toroidal dipole moment arises because of oscillating current density. Dynamic toroidal moment could interact with incoming electromagnetic field, as well as it could be included by incoming radiation.[60] The moment of toroidal dipole is given by following formula[70]-

$$\boldsymbol{T} = \frac{1}{10c}\int[(\boldsymbol{r}.\boldsymbol{J})r - 2\boldsymbol{r}^2\boldsymbol{J}]d^3\boldsymbol{r} \qquad \ldots\ldots\ldots 1.2$$

where *'$\boldsymbol{r}$'* is coordinate vector with its origin placed at the center of torus, *'$\boldsymbol{c}$'* is the speed of light and '$\boldsymbol{J}$' is the current density. Previously, it was considered to be independent family of multipoles because it was considered to have direct implications on electromagnetic excitation and optical forces in media with toroidal topology. Recently, a mathematical study of small sources (with radial current density $\boldsymbol{J}_\omega(\boldsymbol{r})$) related electric dipole and toroidal dipole, by applying small source approximation to spherical Bessel function and considered terms up to second order in expression of dipole vector of electric parity in spherical vector basis ($\boldsymbol{a}_1^\omega$).[71] Equation 1.3 represents final form of a_1^ω after approximation, in which first $(k)^0$ term indicates electric dipole moment ($\boldsymbol{e}^\omega$) and k^2 term indicate toroidal dipole moment ($\boldsymbol{t}^\omega$).

$$\boldsymbol{a}_1^\omega \approx \underbrace{-\frac{1}{\pi\sqrt{3}}\int d^3\boldsymbol{r}\boldsymbol{J}_\omega(\boldsymbol{r})}_{\boldsymbol{e}^\omega} \underbrace{-\frac{1}{\pi\sqrt{3}}k^2\int d^3\boldsymbol{r}\frac{1}{10}\{[\boldsymbol{r}^\dagger\boldsymbol{J}_\omega(\boldsymbol{r})]\boldsymbol{r} - 2r^2\boldsymbol{J}_\omega(\boldsymbol{r})\}}_{\boldsymbol{t}^\omega} \quad \ldots\ldots 1.3$$

Hence, it has been established that unlike electric and magnetic multipoles, toroidal multipole is not an independent member of multipole family. Above expression also states that if a source

contains electric and toroidal dipoles, then electromagnetic scattering outside the source boundary because both dipoles cannot be separately determined. So toroidal dipoles cannot be independently excited, rather they are always accompanied with electric dipole excitation. Mathematical method of multipole decomposition provides a solution in this regard to analyze the contribution due to toroidal multipole. Figure 1.6 shows spatial orientation of the first three members (dipole, quadrupole, octupole) of electric, magnetic, and toroidal multipole, together with their far-field power radiation pattern of oscillating multipoles. Analytical studies revealed that for similar characteristic length (R) of electric, magnetic, and toroidal dipoles, electromagnetic scattering scales as $\sim \left(\frac{R}{\lambda}\right)$, $\sim \left(\frac{R}{\lambda}\right)^2$ and$\sim \left(\frac{R}{\lambda}\right)^3$, respectively, where λ is free-space wavelength.[57,72]

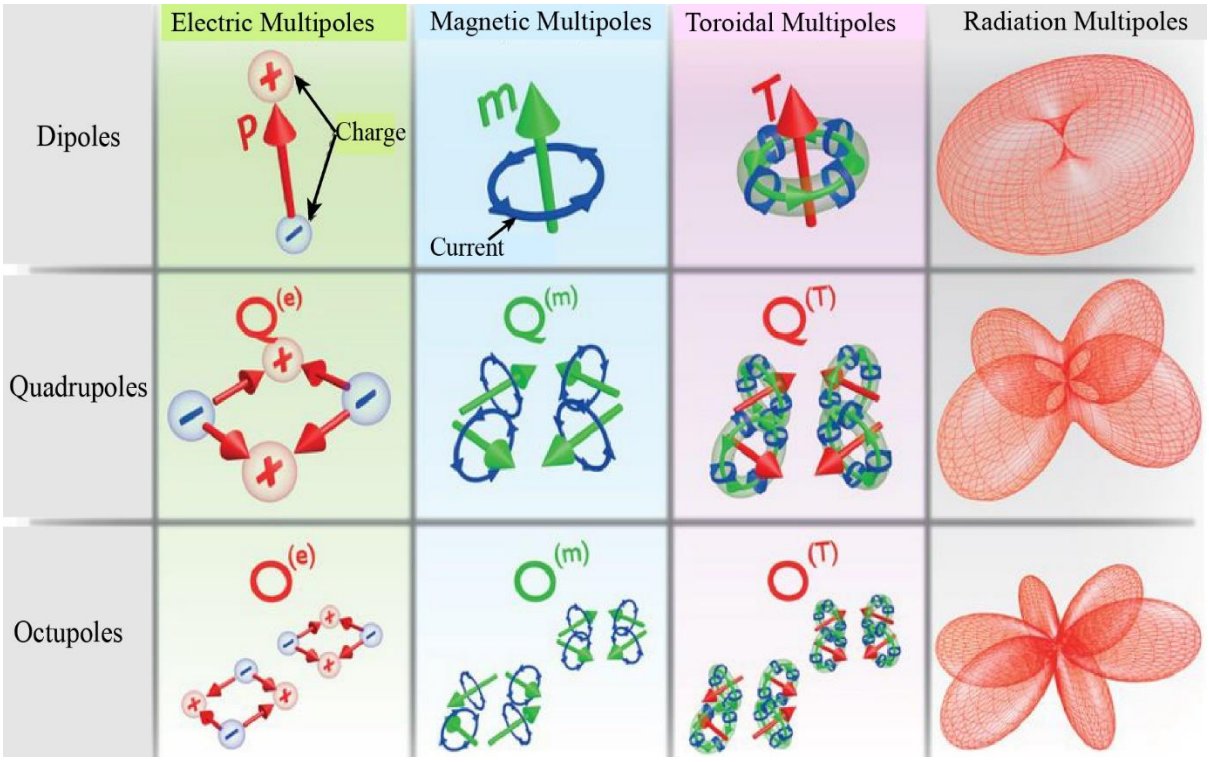

Figure 1.6: Multipole moments and far-field radiation pattern for first three members of electric, magnetic and toroidal multipoles. Same order multipole of each family has identical power radiation pattern.[70]

Analytically it is difficult to quantify toroidal dipole contribution in electromagnetic scattering originating from small particles ($R << \lambda$) because their effects are overshadowed by dominating electric and magnetic multipoles. Toroidal contributions are significant in relatively large structures with toroidal topology.[73] Therefore, as the size of molecules or structure increases, the contributions of toroidal dipoles become extremely important in comparison to standard electric and magnetic dipoles.

Even for artificially structured subwavelength meta-molecules, toroidal excitations have capability to reduce radiative losses, therefore enhancing the device performance.[74] A metamaterial with toroidal topology can be tailored in a manner to supress lower-order electric and magnetic multipoles, thus allowing the response to be dominated by toroidal dipole.[73] Next section briefly presents the development in the field of metamaterials for incorporating toroidal excitation in metasurfaces.

1.3 Multipole approach to electromagnetic scattering

If we look way back in history, multipole expansions are commonly used in the analysis of gravitational and electromagnetic fields.[75,76] Mathematically, in multipole expansion field at far away point is depicted in terms of different sources confined in a small boundary. The sources confined in small region could belong to same family or different family. Within the same family of multipoles, members could belong to different order, such as dipole, quadrupole, octupole etc., depending on their radiation pattern. Multipole decomposition provides a quantitative way to link microscopic multipole excitation within the unit cell of metasurface to far-field macroscopic metamaterial response. Microscopic response corresponds to electromagnetic scattering by the resonator (meta-atom) in the unit cell of metasurface, in which different multipoles are induced by plane wave radiation incident normally on the plane of unit cell. In this process electric and magnetic multipole moments (dipole, quadrupole,

octupole etc.) are calculated separately, which then added together with phase information to analyze the behaviour of metasurface. Multipole moments are extracted through numerical simulator, which uses induced charge or current density in resonator of known geometry. Assuming that unit cell of metasurface is isolated, scattered power from these multipoles are calculated by integrating it over all the directions. On the other hand, macroscopic response in terms of scattered power is directly obtained by the numerical simulator for entire metasurface. Radescu and Vaman derived the below given expression for radiative intensity inclusively in terms of lower order electric, magnetic and toroidal multipoles-[57]

$$I = \frac{2\omega^4}{3c^3}\left|\vec{P}\right|^2 + \frac{2\omega^4}{3c^3}\left|\vec{M}\right|^2 + \frac{2\omega^6}{3c^5}\left|\vec{T}\right|^2 + \frac{4\omega^5}{3c^4}\left(\vec{P}\cdot\vec{T}\right) + \frac{\omega^6}{5c^5}\vec{Q}^{(e)}_{\alpha\beta}\vec{Q}^{(e)}_{\alpha\beta}$$

$$+ \frac{\omega^6}{20c^5}\vec{Q}^{(m)}_{\alpha\beta}\vec{Q}^{(m)}_{\alpha\beta} + \frac{2\omega^6}{15c^5}\left(\vec{M}\cdot\left\langle\vec{R}^2_M\right\rangle\right) \qquad \ldots\ \ldots\ \ldots\ 1.4$$

Above equation had been derived to the order $\left(\frac{1}{c^5}\right)$ in which other higher order contribution to the 5th order of $\left(\frac{1}{c}\right)$ have been not considered. The terms in the expression represent the scattered power by: electric dipole $\left(\vec{P}\right)$, magnetic dipole $\left(\vec{M}\right)$, toroidal dipole $\left(\vec{T}\right)$, the interference between the electric and toroidal dipoles $\left(\vec{P}\cdot\vec{T}\right)$, electric quadrupole $\left(\vec{Q}^{(e)}_{\alpha\beta}\right)$, magnetic quadrupole $\overrightarrow{(Q^{(m)}_{\alpha\beta}}$), and the correction due to the interference between the magnetic dipole and the first-order mean-square radius $\left(\left\langle\vec{R}^2_M\right\rangle\right)$ of the magnetic dipole distribution. By integrating the charge density $\rho(r)$ or the current density $\vec{J}(r)$ distribution within the unit cell, multipole moments could be calculated in Cartesian coordinate by the equations listed below:

$$P_\alpha = \int d^3\, r\rho r_\alpha = \frac{1}{i\omega}\int d^3\, rJ_\alpha, \qquad \ldots\ \ldots\ \ldots\ 1.5\ (a)$$

$$M_\alpha = \frac{1}{2c}\int d^3\, r(\vec{r}\times\vec{J})_\alpha, \qquad \ldots\ \ldots\ \ldots\ 1.5\ (b)$$

$$T_\alpha = \frac{1}{10c}\int d^3\, r[(\vec{r}\cdot\vec{J})\, r_\alpha - 2r^2 J_\alpha], \qquad \ldots\ \ldots\ \ldots\ 1.5\ (c)$$

$$Q_{\alpha,\beta}^{(e)} = \frac{1}{2}\int d^3\, r\rho \left[r_\alpha r_\beta - \frac{1}{3}\delta_{\alpha,\beta} r^2\right]$$

$$= \frac{1}{i2\omega}\int d^3\, r[r_\alpha J_\beta + r_\beta J_\alpha - \frac{2}{3}\delta_{\alpha,\beta}(\vec{r}\cdot\vec{J})], \quad \ldots\ldots\ldots 1.5\ (d)$$

$$Q_{\alpha,\beta}^{(m)} = \frac{1}{3c}\int d^3\, r[(\vec{r}\times\vec{J})_\alpha\, r_\beta + (\vec{r}\times\vec{J})_\beta\, r_\alpha] \quad \ldots\ldots\ldots 1.5\ (e)$$

$$\langle R_M^2\rangle = \frac{1}{2c}\int d^3\, r(\vec{r}\times\vec{J})_\alpha\, r^2 \quad \ldots\ldots\ldots 1.5\ (f)$$

Here Greek letters subscripts ($\alpha, \beta = x, y, z$) denote Cartesian components of vectors, and Kronecker delta $\delta_{\alpha,\beta}$ takes value 0 or 1 ($\delta_{x,x} = \delta_{y,y} = \delta_{z,z} = 1$, otherwise $\delta_{\alpha,\beta} = 0$).

Above approach of scattered power allows a qualitative comparison between microscopic and macroscopic response of metasurface, which has some limitations depending on the strength of different multipoles. Multipole scattering which are dominated by a single multipole, microscopic and macroscopic nearly matches, but it fails to match especially in cases when there are several competing multipoles contribution to metamaterial response. V. Savinov et. al. derived a mathematical formulism to overcome the limitation of scattered power approach by multipole decomposition.[72] According to his approach, the radiation information of each multipole moment could be retrieved at a distant point in terms of electric field amplitude and phase. The vector addition of electric field components of all multipoles gives resultant electric field amplitude at that point which then could be used to calculate the far field scattered power. The scattered power calculated through this analysis is then related to transmittance or reflectance of unit cell. The advantage of calculating net electric field by this method is that it considers the interference effect between different multipoles. Following equation gives the net electric field amplitude ($\vec{E}_s$) due to different multipoles (higher order multipoles have been neglected):

$$\vec{E}_s = \frac{\mu_o c^2}{2\Delta^2}\Big[-ik\vec{p}_{||} + ik\hat{R}\times\left(\vec{m}_{||} - \frac{k^2}{10}\vec{m}_{||}^{(1)}\right) - k^2\left(\vec{T}_{||} + \frac{k^2}{10}\vec{T}_{||}^{(1)}\right) + k^2\left(\vec{Q}^{(e)}.\hat{R}\right)_{||}$$

$$-\frac{k^2}{2}\hat{R}\times\left(\vec{Q}^{(m)}.\hat{R}\right)_{||} - \frac{ik^3}{3}\left(\vec{Q}^{(T)}.\hat{R}\right)_{||} + ik^3\left(\left(\vec{O}^{(e)}.\hat{R}\right).\hat{R}\right)_{||}$$

$$-\frac{ik^3}{180}\left(\hat{R}\left(\left(\vec{O}^{(m)}.\hat{R}\right).\hat{R}\right)_{||}\right)\Big].exp(-ikR) \qquad \ldots\ldots\ldots 1.6$$

Here Δ^2 is the area of the unit cell, k is the wave number, c is the speed of light, μ_0 is the magnetic permeability, R is the perpendicular distance of observer, and $\hat{R}$ is the unit vector perpendicular to the plane of metasurface. Above equation 1.6 contains ten terms corresponding to the electric ($\vec{p}$), toroidal ($\vec{T}$) and magnetic ($\vec{m}$) dipoles, electric ($\vec{Q}^{(e)}$), magnetic ($\vec{Q}^{(m)}$) and toroidal ($\vec{Q}^{(T)}$) quadrupoles, electric ($\vec{O}^{(e)}$) and magnetic ($\vec{O}^{(m)}$) octupoles, and the lowest-order corrections, toroidal ($\vec{T}^{(1)}$) and magnetic ($\vec{m}^{(1)}$) dipoles, which accounts for the finite size of the resonator in unit cell. || sign represents projection of multipoles along metasurface plane. Among all electric, magnetic and toroidal moments that appear in equation 1.6, toroidal multipole is of great interest because of its interesting properties. Following section briefly introduce the toroidal dipole, which is lowest order toroidal multipole, and the importance of toroidal dipole excitation in metamaterials.

1.4 Toroidal excitation in metamaterials

Array of artificially structured subwavelength resonator facilitate to achieve desired electromagnetic functionality (see Sec. 1.1). Using artificially designed toroidal solenoid arrays, first investigation in the direction of toroidal dipole was made in microwave regime, where optical activity of chiral toroidal metamaterial had been discussed in terms of multipole moments.[77] However, the signature of toroidal dipole was supressed due to presence of higher

order dominant electric and magnetic multipoles. In 2010, T. Kaelberer et. al. experimentally observed absorption resonance through toroidal dipole excitation in metamaterial containing four microwave ring resonators in unit cell (see figure 1.7a).[73] In this experiment the front pair and rear pair of ring resonators were excited by in-phase and anti-phase component of magnetic field, leading to magnetic resonance (see Res. I in figure 1.7b), all magnetic dipoles in same direction) and toroidal resonance (see Res. II in figure 1.7b), head-to-tail arrangement of magnetic dipoles) in transmission (see figure 1.7c) and reflection (see figure 1.7d) spectra. The strong presence of toroidal excitation (see T_z in figure 1.7e) in four ring resonator structure was also established by multipole analysis. These initial results quickly captured attention, which lead to many works to further enhance the response of toroidal excitation, and simultaneously supressing the contribution of electric and magnetic multipoles.[78,79]

Metamaterials with 3D torus topology are challenging to be fabricated, so simple 3D designs with resonators on both sides of substrate were introduced to ease the fabrication of toroidal metamaterials (see figure 1.8a), where unit cell of metasurface constitutes a planar cross section of torus.[80] Theoretical studies have been performed to show that toroidal excitation could exist at terahertz and at optical frequencies by downsizing metamolecules made of cluster of split ring resonators (see Figure 1.8b).[81] Plasmonic core shell nano-particles also supports toroidal excitation modes in optical regime of electromagnetic spectrum, although these resonances were damped due to high ohmic losses. First time toroidal modes excitation at visible frequency was demonstrated by periodic array of oligomer nanocavities in a silver film through energy-filtering transmission electron microscopy (EFTEM) (see figure 1.8c).[82] As the device gets smaller imperfection during fabrication processes significantly effects the electromagnetic performance, which undermines the excitation of these coupled modes. Several works are still going on to relate the dynamic toroidal excitation, and macroscopic properties of material medium defined in terms of transmission, reflection, and absorption.[72]

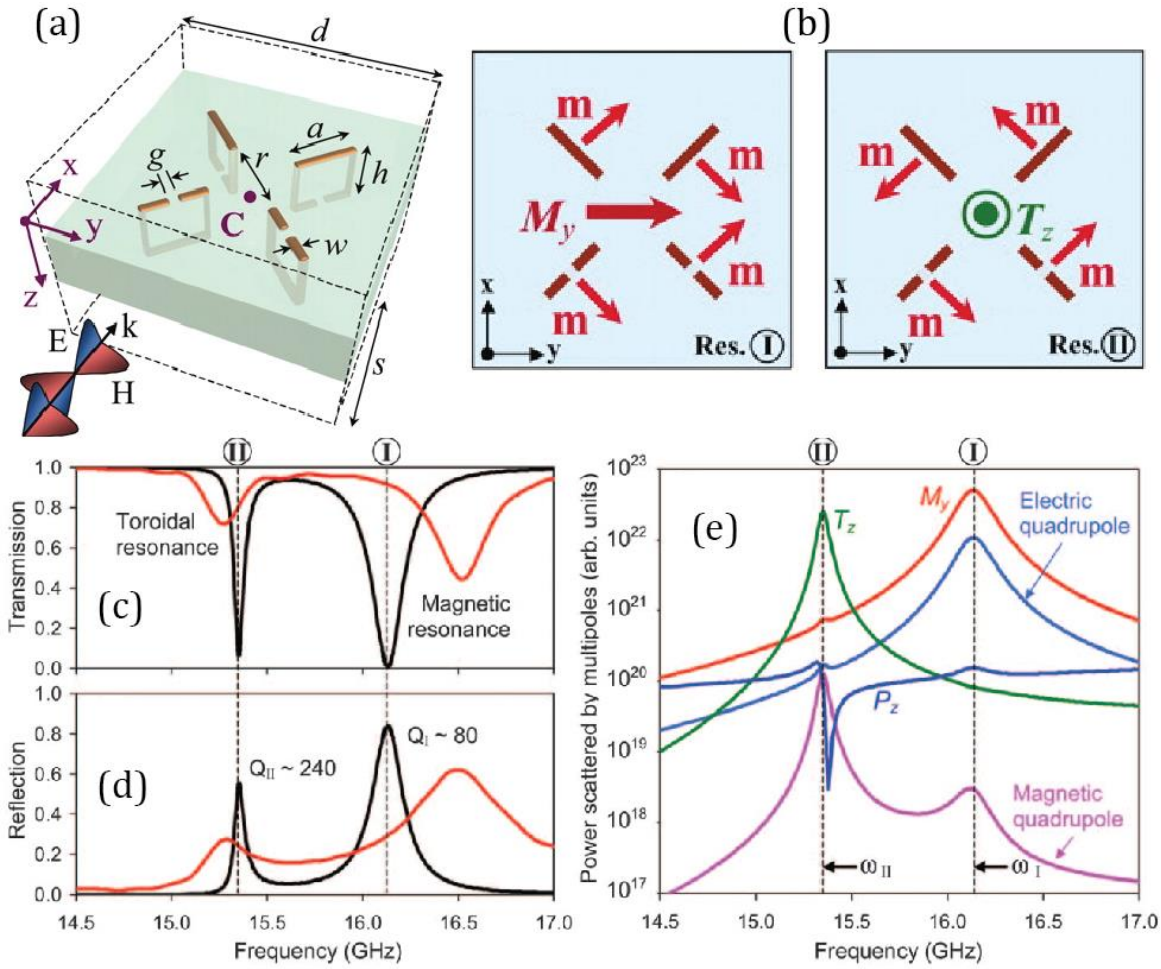

Figure 1.7: First experimental observation of dominant toroidal excitation. a) Schematic of four microwave ring resonators in presence of electromagnetic excitation. b) Arrangement of magnetic dipoles during magnetic (Res. I) and toroidal excitation (Res. II). Simulated and experimentally measured transmission (c) and reflection (d) spectra. e) Multipoles computation representing electric, magnetic and toroidal multipoles.[73]

Recent observation of toroidal dipole modes in metamaterials have further triggered to study their radiation scheme. Far field radiation pattern of toroidal dipole matches with electric dipoles, so their radiation pattern could be combined in a manner to interfere destructively. If radiation pattern toroidal and electric dipoles of equal strength interfere destructively, we could get a non-radiating anapole configuration (see figure 1.9a).[70] Some theoretical studies propose that, non-radiating configurations comprise of electric and toroidal dipoles generate

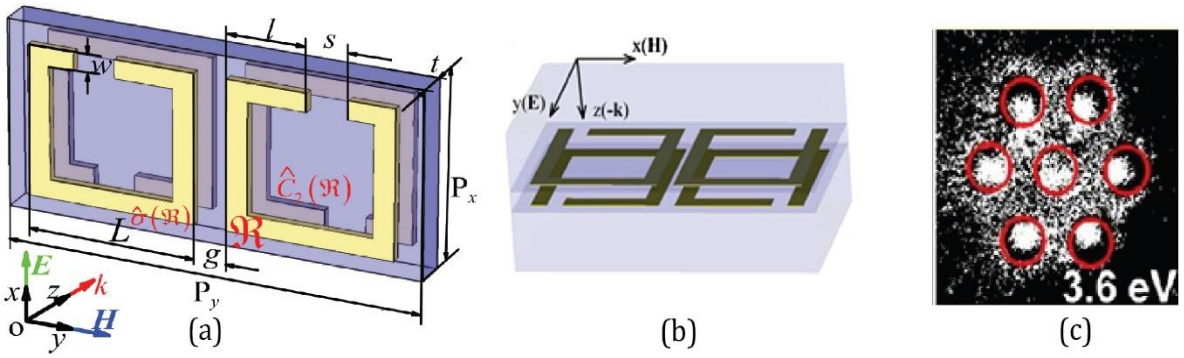

Figure 1.8: Simplified 3D metasurface for toroidal excitation at a) microwave, b) terahertz, and c) visible frequencies.[80-82]

propagating electromagnetic potentials[155] that can be used as a new channel for information transfer. In area of nanophotonics an idea of nanoscale laser has been proposed, where enhanced stimulated emission is achieved through anapole excitation (see figure 1.9b).[83]

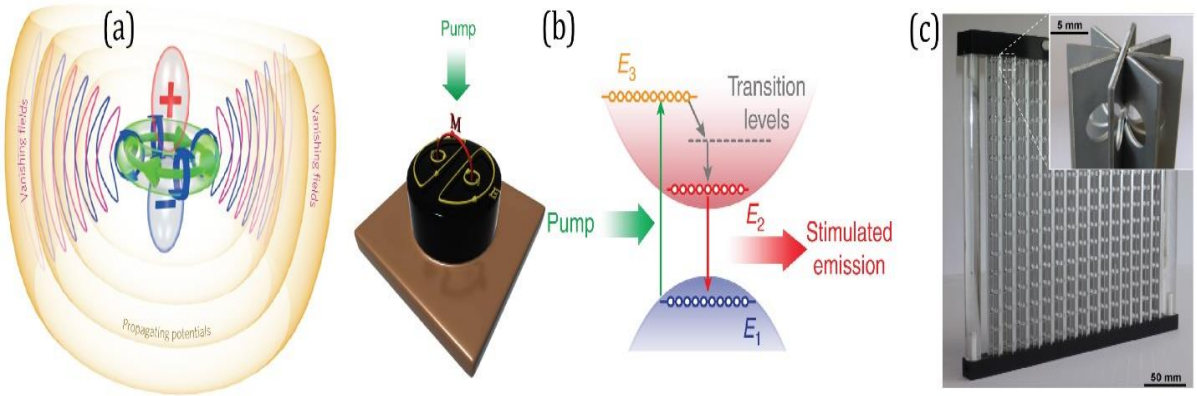

Figure 1.9: a) Schematic representation of anapole where electromagnetic fields originating from electric and toroidal dipole cancel each other.[70] b) Nanoscale laser where external pumping enhances stimulated emission by anapole excitation. [83] c) Microwave metamaterial designed to excite electric and toroidal excitation.[84]

Though it is difficult to achieve perfect anapole condition (its difficulty to simultaneously excite electric and toroidal dipoles of equal strength), yet toroidal dipole could be used to lower the radiation loss due to electric dipoles which are dominant in electromagnetic scattering of metamaterials. In one of the works, resonant transparency in a microwave metamaterial was

realized by the destructive interference between electric and toroidal dipoles (see figure 1.9c).[84] The full potential of toroidal excitation is yet to be investigated in naturally occurring materials and artificially designed structures with toroidal topology. Toroidal excitation provides a different approach to tailor the radiative loss mechanism which could be important at terahertz regime in increasing the device performance. Toroidal metamaterials can be used to confine light in optical cavity, which can be used for switching and sensing applications. Toroidal excitation remains an emerging field of study as metamaterial community is shifting from metallic to dielectric resonators, where the loss channel is entirely dominated by radiative loss.

1.5 Scope of the thesis

In the area of research, photonics has emerged as one of the most powerful tools to explore and manipulate the light matter interaction for the development of next generation electro optic devices. In entire range of electromagnetic spectrum, terahertz frequencies, particularly in the range of 0.1 THz – 4 THz; are of immense interest because they have absolutely no ionizing radiation impact, as well as they are harmless for biological entities. As compared to microwave frequencies, terahertz provides better spatial resolution necessary for imaging applications, as well as for building next generation high speed wireless communication networks. To fully exploit the advantages of terahertz radiation, it is coupled to various artificially engineered platform to achieve certain features, such as bending, enhancement, and absorption of terahertz waves, not possible with conventional materials. Aiming to efficiently couple and control the electromagnetic radiation, metamaterial provides a simple and efficient platform to potentially develop applications in diverse field of technology; such as sensing, telecommunication, nonlinear interaction, information processing, and computing. The terahertz response of the subwavelength resonating elements in the metasurface array is influenced by near field coupling, which depends on the electric and magnetic nature of

interaction between neighboring resonators. Manipulating the near field coupling in these metasurface is of great interest as they give advantage in investigating the physics behind electromagnetic interaction, and in exploring the scientific aspect of these subwavelength structures. Spatial orientation of neighboring resonators or selective inclusion of active element in resonator array are some of the straightforward techniques to manipulate near field coupling.

The signature of near field coupling between subwavelength resonators is also observed in the far field transmission spectrum of metasurface. At resonance coupling effects are quite dominant, which is reflected in terms of linewidth of resonance. At terahertz frequencies loss channels are mainly governed by radiative losses, so tuning near field coupling could tailor the linewidth of resonance and would certainly enhance the device performance necessary for practical implementation. In general, for photonic device there is requirement for high quality factor (Q) resonances, with extremely high electromagnetic field confinement for enhanced spectral resolution in spectroscopy applications and to enhance the sensitivity. Toroidal excitation has emerged as one of the schemes to reduce the radiative loss channel, as compared to the radiative loss channel of conventional electric and magnetic excitation. This thesis focuses on strategies to enhance the performance of planar metasurface, by tailoring the radiative loss channel through toroidal dipole excitation at terahertz frequencies of electromagnetic spectrum. Easy fabrication of planar metasurface further simplifies the complexities involved in tailoring the toroidal dipole, and switching the nature of metasurface excitation from toroidal dipole to electric and magnetic dipole.

So far, this chapter introduces the concept of metamaterials, toroidal dipole moment, and some preliminary demonstration of exciting toroidal dipole moment in 3D metamaterial. In addition to this, approach of multipole decomposition has been incorporated to numerically extract the contribution of dominant electric, magnetic, and toroidal dipoles.

Chapter 2 describes the CST software platform used to analyze the electromagnetic response of metasurface, and the processes involved in fabricating the planar toroidal metasurface sample. Additionally, it includes brief discussion on the exotic features of terahertz band of electromagnetic spectrum, and the experimental setup details of terahertz spectroscopy method based on photoconductive antenna and nonlinear crystal.

Chapter 3 discusses a simple planar composite resonator design to introduce the contribution of toroidal dipole, in addition to fundamental electric and magnetic multipoles, during electromagnetic resonance of the resonator array in metasurface. The signature of toroidal excitation is observed as asymmetric line shaped resonance in transmission spectra, which appears due to interference between electric dipole and toroidal dipole. This chapter also includes the discussion on tailoring the strength of toroidal dipole that could be used to passively tune the line width of asymmetric line shaped resonance, which drastically changes the amplitude and *Q* factor of resonance. The scheme discussed is one of the first work that introduces a strategy to induce toroidal coupling in planar metasurface.

Chapter 4 explains the toroidal coupling scheme for conventional asymmetric double split gap square ring resonator (Fano resonators) array, which significantly decreases the line width of asymmetric resonance. A comparative study has been performed for Fano resonator array with and without toroidal coupling, where toroidal coupling is achieved between neighboring resonators by alternatively flipping resonator along one direction in equally spaced Fano resonator array. The toroidal coupling scheme is easy to implement as it involves single step photolithography cycle for device fabrication.

In chapter 5, an active platform has been realized to switch the nature of electromagnetic excitation from toroidal dipole to electric or magnetic dipole, where individual asymmetric resonator supports electric or magnetic resonance while combination of adjacent resonators supports toroidal resonance. By selective inclusion of photoactive silicon beneath the split gaps

of one or both adjacent resonators toroidal excitation could be switched to electric or magnetic excitation. Further, the study also reveals the active tuning of toroidal coupling, which modulates the amplitude, *Q* factor and figure of merit (FoM) of electromagnetic resonance.

Chapter 6 investigates the sensing potential of toroidal coupling mediated electromagnetic resonance in planar metasurface. The detailed study explores fringing field effects which are important in estimating the thickness of dielectric layer for maximum shift in resonance frequency for sensing application. It also includes experimental analysis for estimating the sensitivity of toroidal metasurface for few hundred nanometers thick dielectric layers. Furthermore, numerical analysis has been performed to examine dependency of metasurface sensitivity on analyte and substrate thickness.

Chapter 7 gives the summary of numerical and experimental results incorporated in the thesis and presents future research directions for toroidal metamaterials.

Chapter 2

Experimental Method: Simulation, Fabrication and Characterization Techniques

This chapter describes the software platform used for the detailed analysis of metasurface, sample fabrication and characterization techniques of planar toroidal metasurface. Section 2.1 explains steps involved in the modeling of metasurface on CST software platform. Section 2.2 gives brief overview of processes involved in fabrication of physical devices. Section 2.3 describes techniques involved in experimental characterization of fabricated devices, at terahertz regime of electromagnetic spectrum.

2.1 Electromagnetic simulation of metasurface

This section briefly introduces the methods used in modelling the electromagnetic response of planar metasurface. Numerical simulation provides a powerful tool in designing, optimizing, and analyzing performance of artificially designed metasurface in high frequency range. Electromagnetic simulations performed by CST Microwave Studio (CST-MWS) basically solves Maxwell's equations for a given medium and defined boundary condition. The integral form of Maxwell's equations in a medium of volume (V) containing charge density ρ and current density $\vec{J}$ are given by-[85]

$$\oint_S \vec{D}.d\vec{S} = \int_V \rho dV \quad \ldots\ldots\ldots 2.1(a)$$

$$\oint_S \vec{B}.d\vec{S} = 0 \quad \ldots\ldots\ldots 2.1\ (b)$$

$$\oint_l \vec{E}.d\vec{l} = \int_S \left(-\frac{\partial \vec{B}}{\partial t}.d\vec{S}\right) \quad \ldots\ldots\ldots 2.1\ (c)$$

$$\oint_l \vec{H}.d\vec{l} = \int_S \left(\vec{J}.d\vec{S} + \frac{\partial \vec{D}}{\partial t}.d\vec{S}\right) \quad \ldots\ldots\ldots 2.1(d)$$

where $\vec{D}$, $\vec{E}$, $\vec{B}$, and $\vec{H}$ represents displacement field, electric field, magnetic field and magnetizing field, respectively. $\oint$ represents closed integral along line (*l*) and surface (*S*).

In metamaterial modelling, both the unit cell and complete full-scale meta-device need to be considered. CST simulation allows the calculation of transmission, reflection and absorption coefficients in a straightforward way. For metasurface modelling, *transient solver* and *frequency domain solver* are two commonly used techniques in CST platform for solving Maxwell's equations. Transient solver is best suited for electrically large structures, and it obtains broadband frequency behaviour of simulated device in a single run. On the other hand, frequency domain solver is advantageous for electrically small subwavelength structures. In this technique, simulations run step by step for each frequency point to obtain broadband behaviour. Thus, the frequency domain solver is most efficient to simulate narrow resonance features. CST-MWS software is a powerful tool in creating structures by providing 3D graphical platform, followed by fully automated meshing technique, before numerical simulator engine is launched. CST contains an extensive library of material properties for most of the commonly used materials such as metals (aluminum, gold etc.), dialectics (quartz, silicon) and other. CST gives freedom to define broad range of user defined materials by assigning material parameters in terms of frequency dependent dispersion. Depending upon some specific frequency bands, some predefined material models such as Drude model, Lorentz model etc., are also available that effectively replicates the material behaviour during

simulations. Detailed flowchart given in figure 2.1 introduces different steps involved in initializing, designing, simulating and analysing the electromagnetic modelling of the metasurface.

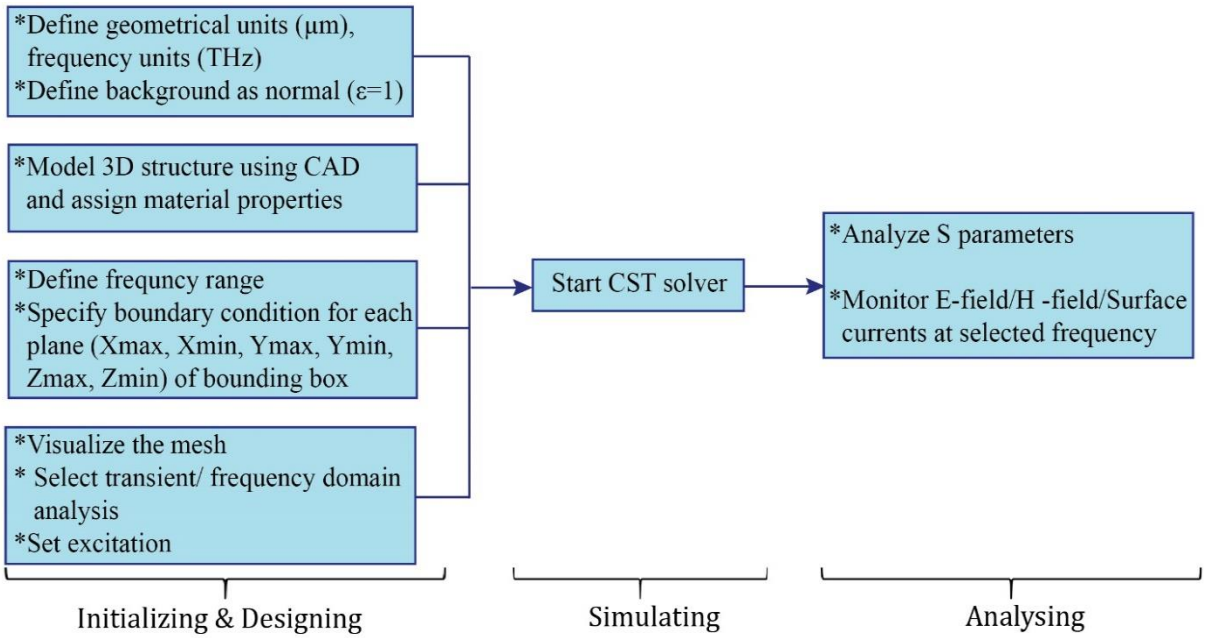

Figure 2.1: Flowchart indicating sequence of steps involved in electromagnetic modelling of metasurface.

In this thesis, frequency domain solvers have been used to numerically model the metasurface. The unit cell boundary condition best mimics the response of metamaterial. Figure 2.2 shows CST snapshots of simulated metasurface with unit cell boundary condition. Figure 2.2a shows the CST boundary condition panel showing $X_{min/max}$,$Y_{min/max}$ setting as “unit cell” to replicate metasurface along XY plane, and “open (add space)”/”open” setting in Z_{max} /Z_{min} for setting-up source/probe position. With these CST boundary conditions, figure 2.2b shows the side view of metasurface depicting source/probe position, and figure 2.2c shows front view of rectangular unit cell (enclosed by pink rectangle) metasurface array along XY plane.

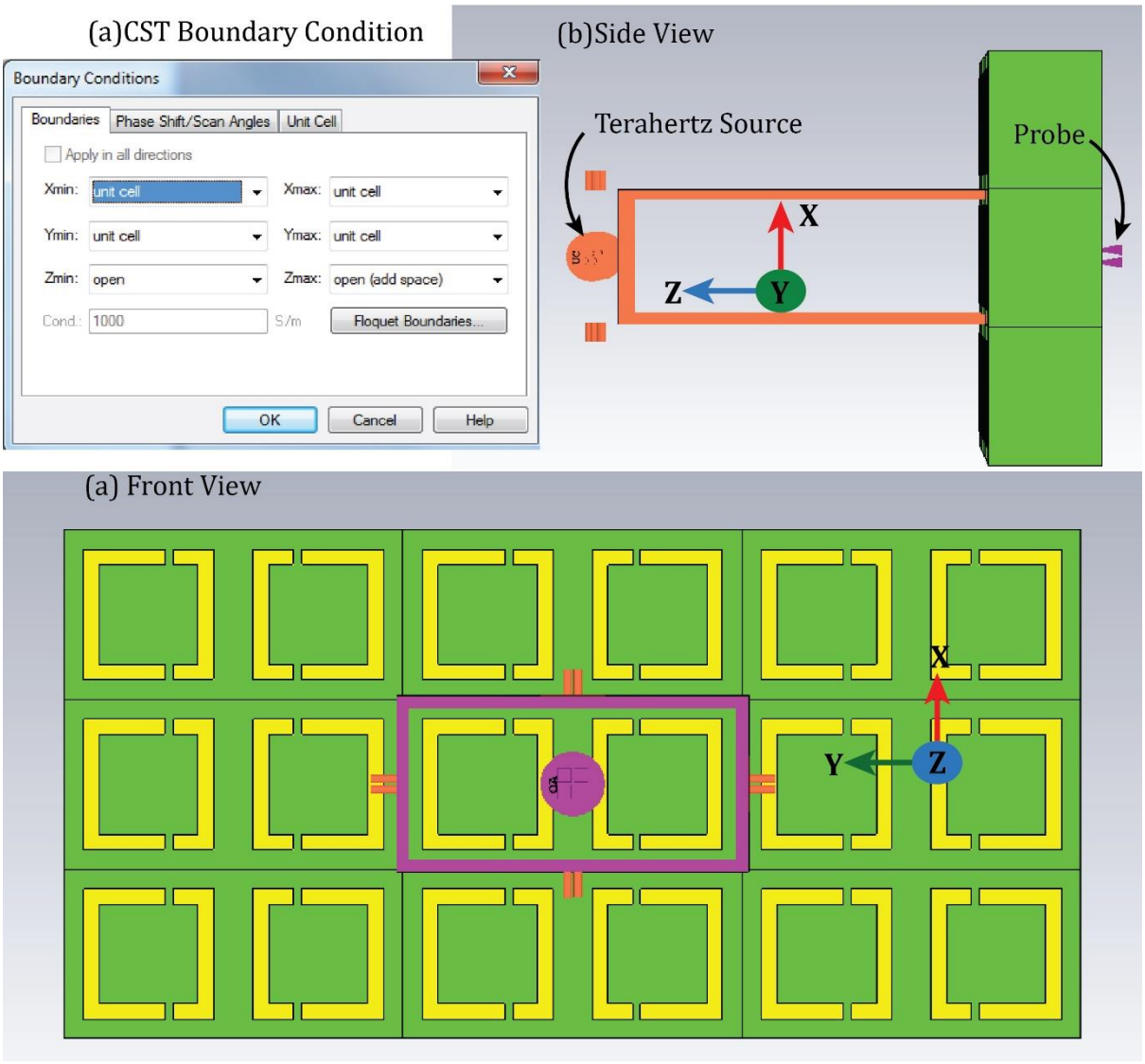

Figure 2.2: Boundary condition for frequency domain simulation. a) Unit cell configuration selected in boundary conditions panel, b) side view representing terahertz source and probe position, c) metasurface array along XY plane

Once boundaries are determined, CST solves Maxwell equations (equation 2.1) for one unit cell by dividing it into smaller tetrahedral grids, this process is known as “meshing”. Meshing procedure performed by CST is automatic in nature. Figure 2.3 represents the meshing of the unit cell with tetrahedral grids. For meshing to be optimized, the tetrahedral grid dimension needs to be smaller than the dimension of structure in design. CST also allows to manually select the minimum grid element size, during automatic meshing for ultrathin designs.

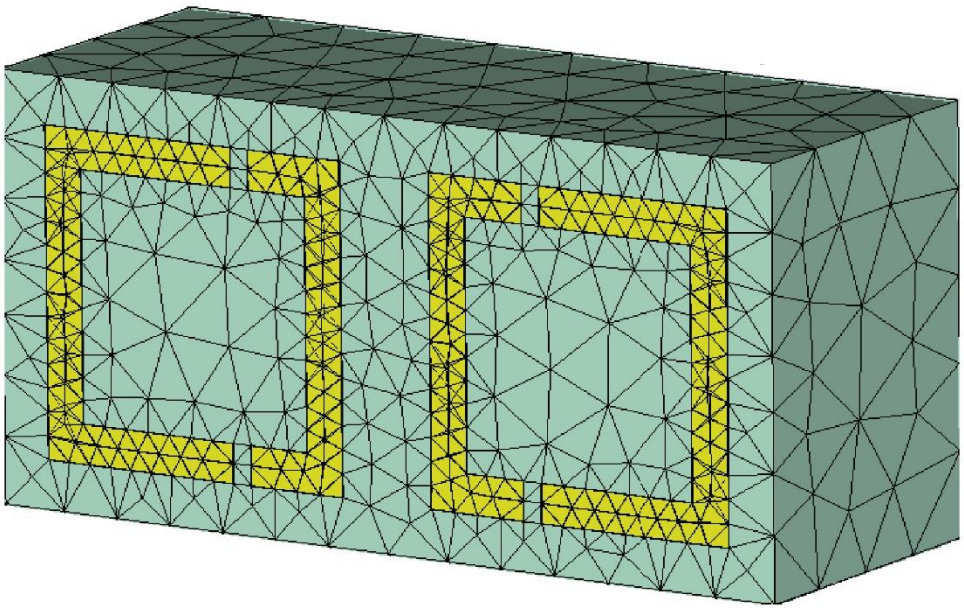

Figure 2.3: Schematic after mesh adaptation with tetrahedral grids for the unit cell containing mirrored resonators (yellow) on thick substrate (green).

In the frequency domain simulation, integral form of Maxwell equations (equation 2.1) is Fourier transformed, resulting in the replacement of time derivative operator by its Fourier equivalent:

$$\frac{\partial}{\partial t} = i\omega \qquad \ldots\ldots\ldots 2.2$$

and transformed equations are solved separately for each frequency through interpolative method. The computed complex transmission and reflection output components are stored in the scattering matrix "S Matrix" called "S-parameters" which relates outgoing wave (*O*) to the incoming wave (*I*). The complete solution can be easily obtained through a system of linear equation represented in matrix form:

$$\begin{bmatrix} O_1 \\ O_2 \end{bmatrix} = \begin{bmatrix} S_{11} & S_{12} \\ S_{21} & S_{22} \end{bmatrix} \begin{bmatrix} I_1 \\ I_2 \end{bmatrix} \qquad \ldots\ldots\ldots 2.3$$

where subscript "1" and "2" represents "port 1" and "port 2", respectively. The coefficients of S Matrix are interpreted as following

S_{11} = reflection coefficient at port 1,

S_{12} = transmission coefficient at port 1,

S_{21} = transmission coefficient at port 2

S_{22} = reflection coefficient at port 2.

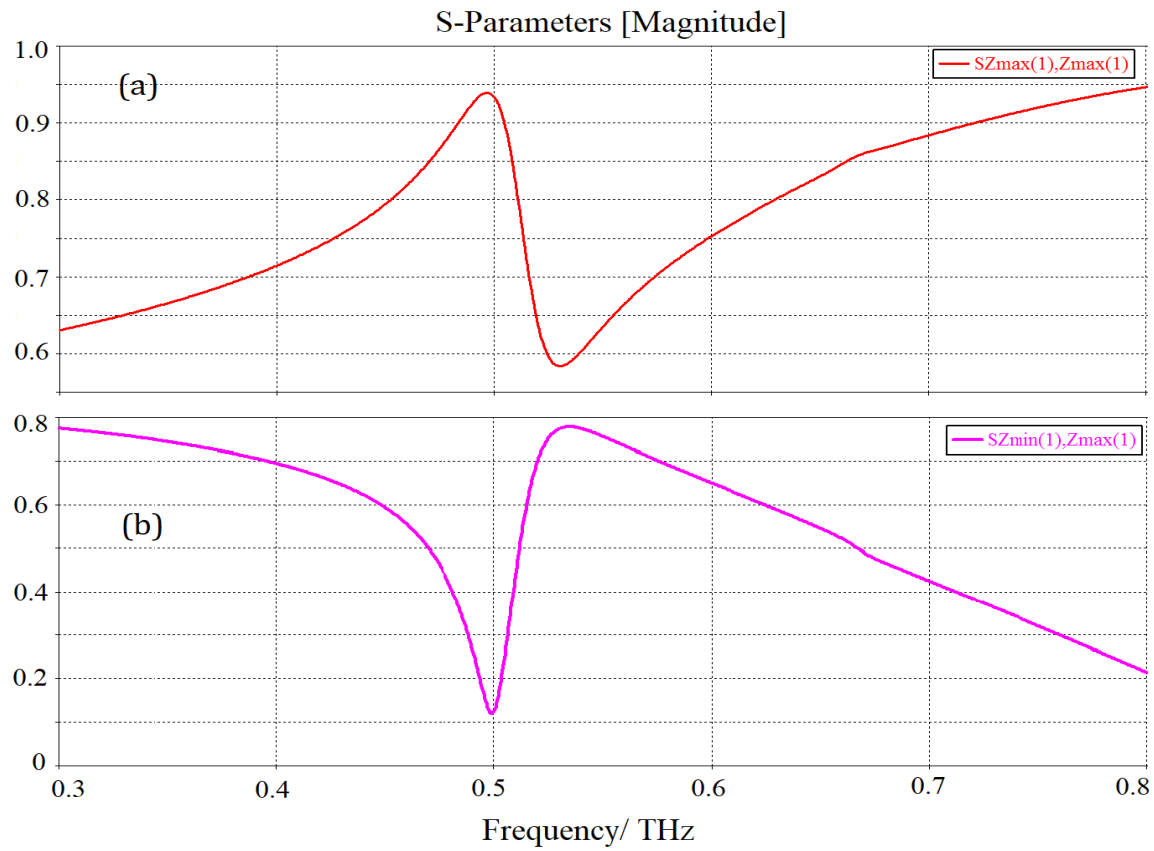

Figure 2.4: Simulated reflection (a), and transmission (b) coefficients versus frequency plots for the metasurface shown in Figure 2.2. Here "(1)" represents incident electric field polarization on the metasurface, which in this case, is along X direction.

Figure 2.4 shows S11 ($SZ_{max}(1)$, $Z_{max}(1)$) and S21 ($SZ_{min}(1)$, $Z_{max}(1)$) coefficients versus frequency plot for electromagnetic excitation at Z_{max} (port 1) and propagating towards Z_{min} (port 2) for the metasurface shown in figure 2.2 .

The CST-MWS also give information about 2D and 3D distribution of electric field, magnetic field, power and surface current densities at specific frequency of interest. The electric field, magnetic field, and charge distribution help to explain both electric and magnetic response of the metamaterial structure and provide adequate information about the nature of the resonance.

2.2 Sample fabrication

Electromagnetic response of metasurface is attributed to resonant excitation of each unit cell that constitutes the whole array. Unit cell contains metallic, or dielectric, or hybrid structures, which resonates at specific frequency. In this section, standardized cleanroom fabrication processes have been discussed for metasurfaces, which are designed to resonate in the far infrared region of the electromagnetic spectrum. The dimension of structures discussed here are on micron scale, such that their resonance frequency lies in the range of 0.2 to 1.2 THz. Metasurfaces are patterened using conventional UV-illumination based photolithography technique. Further, these metasurfaces are classified as passive and active metamaterials. Passive metasurface contains conventional metallic structure that lacks tunability, while active metasurface could be tuned by some external stimulation, for example, metal-semiconductor hybrid structure where semiconductor is excited optically. The detailed fabrication process for each of them is elaborated below.

2.2.1 Passive metamaterial sample

Planar metasurface array usually consists of micron sized periodic structures of metal on a high resistivity silicon substrate. Double side polished p-type silicon substrates of thickness 500 μm and resistivity higher than 5000 Ω-cm have been used to design passive metasurfaces. Figure 2.5 shows different processes involved in fabrication of metallic resonators on silicon substrate. These kind of metasurface require single step lithography cycle for fabrication.

The detailed fabrication steps are explained below:

1) Silicon substrates are thoroughly cleaned by using acetone solvent in ultrasonic baths, and later washed in isopropyl alcohol (IPA) to remove the traces of acetone. These cleaned substrates are then dried in the dry nitrogen flow to get rid of any remnant solvent or moisture.

2) A positive photoresist (AZ5214E) is then deposited on the silicon substrate using spin coating technique. The desired thickness of 1.5 μm of photoresist, is achieved by spin coating the photoresist at 4000 rpm speed for 40 seconds. The coated photoresist is then hardened by prebaking it on a hot plate at 105^{o}C for 60 seconds.
3) UV light is illuminated through appropriate mask on prebaked substrates by employing Mask-aligner MJB04. To obtain better resolution and clear sidewall profile pattern on photoresist, hard contact mode setting has been used for UV illumination.
4) After UV illumination, photoresist coated substrates are soaked in the developer solution (AZ developer) for 30 seconds and then rinsed in the deionized (DI) water. The developer solution dissolves the portion of the photoresist area which is exposed to UV light, and thus leaving behind the desired pattern. No traces of photoresist should remain in the exposed area, as it may spoil device during the lift-off process.
5) The aluminum metal of thickness 200 nm is deposited on substrate containing patterned photoresist using thermal evaporation technique. To ensure good quality of films, the thermal deposition have been carried out at rate of 0.5 A^{o}/sec.
6) Finally, the substrates are soaked in acetone to lift-off undesired metal and the photoresist from the substrate and thus leaving behind desired metallic metamaterial structures. The fabricated samples are again washed with isopropyl alcohol (IPA), and dried in nitrogen.

In accordance with the lithography and thermal deposition steps discussed above, figure 2.6 shows the optical microscopy image of fabricated sample, which contains array of double split gap square shaped aluminum resonators (enclosed by dotted square region) on silicon substrate.

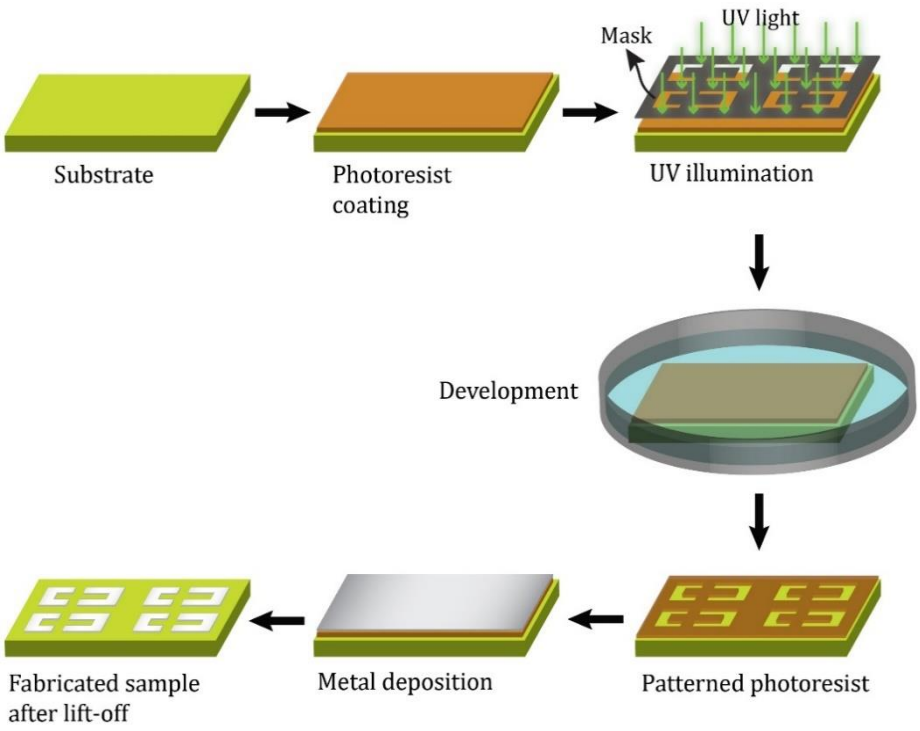

Figure 2.5: Pictorial representation of various steps (photolithography, thermal deposition, lift-off) involved in sample fabrication.

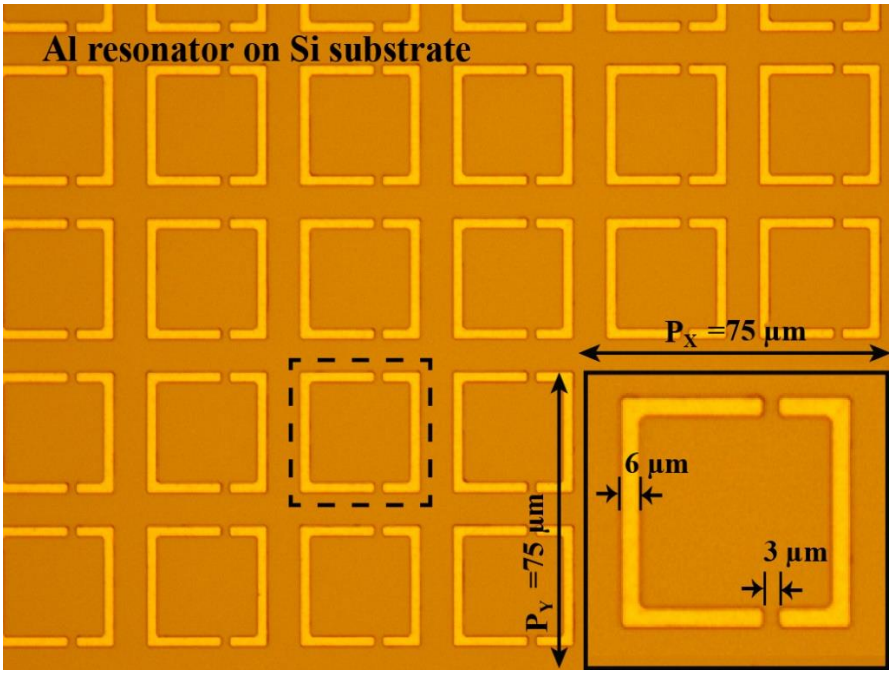

Figure 2.6: Optical microscopy (OM) images of the metallic resonator on silicon substrate. Enclosed dotted square region shows unit cell containing square shaped double split gap aluminum resonator. Zoomed unit cell depicting dimensions (periodicity (P_X, P_Y), split gap size and width of Al strip) in micron scale.

2.2.2 Active metamaterial sample

In contrast to passive metamaterial, active metamaterial (metal-semiconductor hybrid metasurface) involves two step lithography cycle for fabrication. Active metasurface has been prepared by using silicon on sapphire substrate (SoS), where silicon layer acts as active element during photoexcitation. Silicon on sapphire (SoS) substrate is composed of 600 nm thick silicon epilayer on 460 µm thick sapphire. First lithography cycle facilitates to fabricate metallic resonators on silicon on sapphire (SoS) substrate, as discussed in previous section. In second step lithography photoresist is patterned such that it remains in selected areas, where silicon is required to be present on sapphire substrate. Schematic image in figure 2.7a shows that patterned photoresist remained in areas between the split gaps of resonator. This second step is quite challenging because it requires proper overlapping of alignment marks in the predefined photomask. Finally, the sample undergoes reactive ion etching (RIE), where silicon is etched

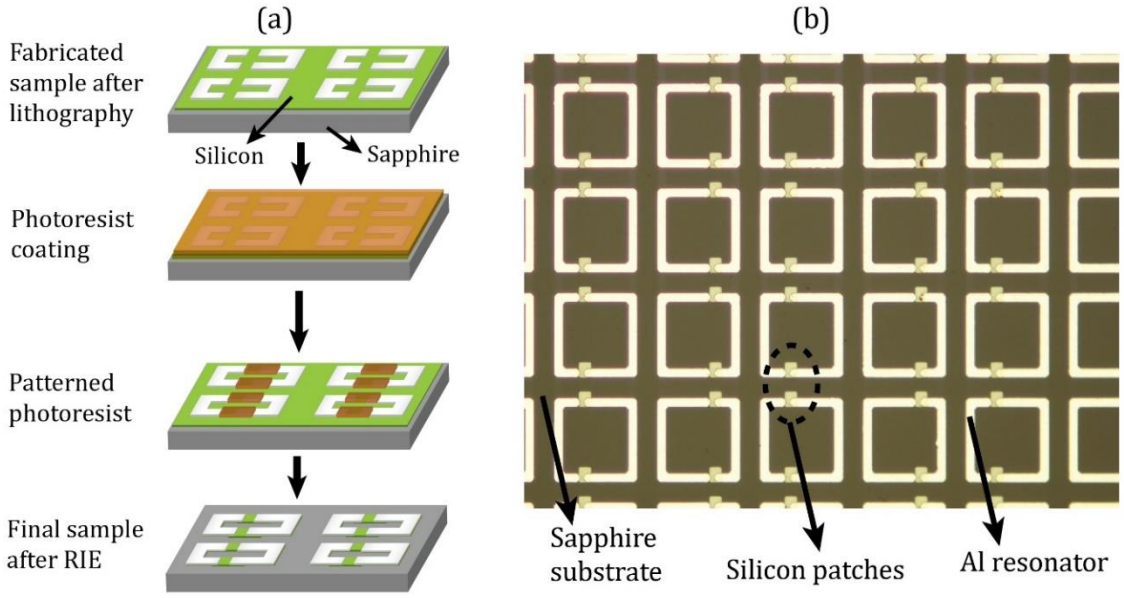

Figure 2.7: a) Graphical representation of photolithography steps for selective reactive ion etching (RIE) of silicon from metasurface. b) Optical microscopy (OM) image of active metasurface on sapphire substrate, where silicon patches (enclosed by dotted circle) lies in the split gaps of aluminum (Al) resonator.

from the exposed areas on the top of metasurface, while silicon is left beneath the metallic resonator and patterned photoresist. Thereafter, sample is washed with acetone and isopropyl alcohol (IPA) to remove traces of photoresist. Figure 2.7b shows the optical microscopy image of hybrid metal-semiconductor metamaterial sample on sapphire substrate, which contains silicon pads between the splits gaps of metallic resonator.

2.3 Terahertz (THz) spectroscopy

This portion briefly introduces the nature and potential applications of terahertz waves. It also introduces the generation and detection of pulsed terahertz waves from femtosecond laser. For spectroscopy applications mainly two types of terahertz setups: photoconductive antenna-based THz setup and nonlinear crystal-based THz setup, have been introduced in this section, which have been further employed to experimentally characterize the samples.

2.3.1 Terahertz (THz) radiation

The terahertz radiation is invisible to the naked eye and lies between the microwave and infrared regime of electromagnetic spectrum. Terahertz breaches the gap between microwave and infrared which are suitable for electronic and photonic applications, respectively (see figure 2.8). In electromagnetic spectrum ‘terahertz gap’ or ‘terahertz band’ corresponds to frequency range of 0.1 THz to 10 THz. The special feature of terahertz radiation is that it can penetrate through ceramics, plastics, paper without significant absorption. Water molecules absorbs, while metal reflects terahertz radiation, resulting in limited transmission through these environments. Because of such diverse response with respect to different environment, makes terahertz an important platform for imaging, security, and scientific applications.

Terahertz waves are mainly characterized by its wavelength and associated energy, for example photon energy of 1 THz photon is around 4.1 meV and has wavelength on the order of 300 µm. Due to its low photon energy terahertz possesses several advantages such as, non-destructive and non-ionizing, which makes them highly important for spectroscopic studies.[86] The meV energy scale of terahertz waves makes them a powerful tool in studying lattice vibrations in solids, in determining intrinsic carrier density of semiconductors and in estimating molecular vibrations.[87] For many years, the spectroscopic and imaging techniques did not cover the THz frequencies due to the lack of efficient terahertz generation and detection sources, but this gap is now aggressively investigated with the development of photoconductive antenna, Schottky diode and nonlinear frequency mixing based THz generation sources.[88-92]

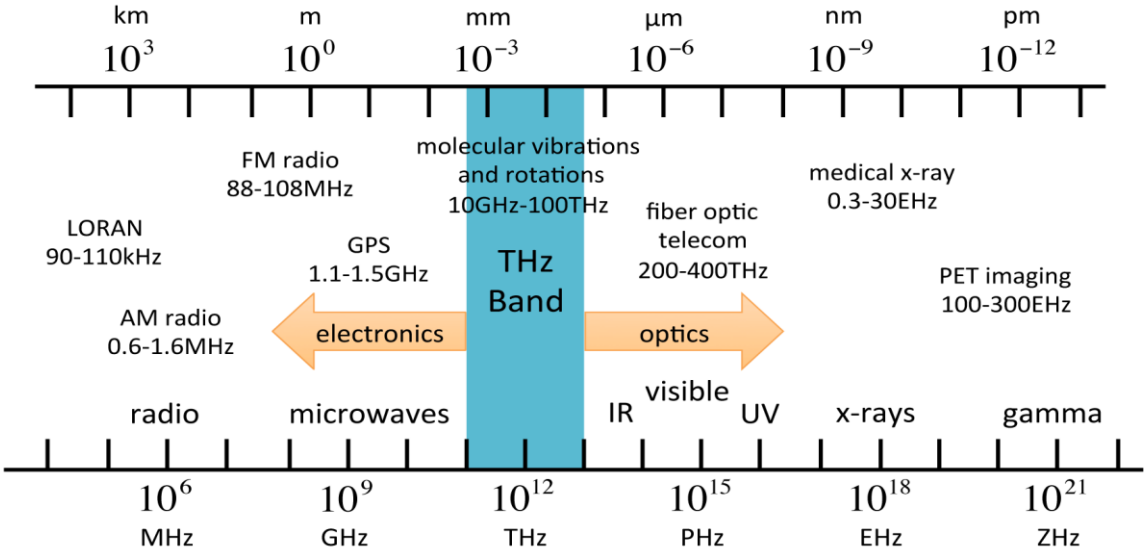

Figure 2.8: Electromagnetic spectrum depicting terahertz band between microwave and infrared regime. (source: internet)

2.3.2 Terahertz time-domain spectroscopy (THz-TDS)

The extraordinary features of terahertz wave make them a powerful platform for spectroscopy technique. THz-TDS provides direct measurement of electric field amplitude and phase information of terahertz pulse through the sample without application of Kramers-Kronig

relations that leads to direct measurement of the material parameters such as complex conductivity, complex refractive index, and complex permittivity. One of the big advantage of terahertz spectroscopy is that it is a contact free technique to measure transient mobile carrier dynamics on picosecond timescales. Terahertz radiation could be generated and detected through several mechanisms.[151-154] Here, we mainly focus on photoconductive antenna based, and non-linear crystal-based THz-TDS setup for generation and detection of terahertz pulse, which have been employed for characterization of metamaterial samples.

2.3.2.1 Photoconductive antenna-based THz-TDS setup

Photoconductive antenna is one of the most widely used component for generation and detection of terahertz pulse, which exhibits robust performance in terms of signal-to-noise ratio (10000 :1).[88,89] Figure 2.9 displays the schematic of generation and detection of terahertz pulse from pulsed femtosecond laser. An ultrafast optical pulse of wavelength 800 nm, with high repetition rate of 1 kHz, is splitted into two parts from beam splitter. With the help of mirrors, one part of beam is guided to first antenna (emitter) for terahertz generation and second part is guided to another antenna (detector) for terahertz detection. The emitter part of photoconductive antenna consists of two metallic electrodes of width (w) 10μm, separated by a distance (L) of 80 μm, on low temperature GaAs substrate. For generation of terahertz pulse, DC voltage of 70 V is applied across the electrodes, and substrate area between the electrodes is irradiated by ultrafast optical pulse. Since the energy of optical pulse is greater than the band-gap energy of semiconductor substrate (GaAs), which results in generation of photo-induced free carriers. The photo-induced carriers generated in the gap, between two metal electrodes, are accelerated by the electric field (E_b) produced by DC biasing of electrodes, which give rise to a time varying photocurrent density ($J(t)$) as given by,

$$J(t) = N(t)e\mu E_b \qquad \ldots\ldots\ldots\ 2.4$$

where *N(t)* is the density of photoinduced charges, *e* is the electronic charge and μ is the mobility of the electrons. Holes contribution could be neglected in the photocurrent because of its low mobility compared to electrons. This time varying current density (*J(t)*) generates radiates energy in form of terahertz pulse. The far-field electric field amplitude (E_{THz}) of terahertz radiation is given by below given equation

$$E_{THz} = \frac{Ae}{4\pi\varepsilon_0 c^2 z}\frac{\partial N(t)}{\partial t}\mu E_b \qquad \ldots\ldots\ldots 2.5$$

where *A* is the optically illuminated area of semiconductor substrate located between the metallic electrodes, ε_0 is the permittivity of vacuum, *c* is the speed of light, and *z* is the distance between the far-field probe and terahertz emitter. It is clear from equation 2.5 that energy of terahertz pulse is derived from the electric energy stored in illuminated area rather than the energy of ultrafast optical pulse used for illumination. The femtosecond optical pulse acts as a trigger to release the energy stored in the gap in form of teraherz pulse. The electric field polarization of the generated terahertz wave is along the biased field. Generated terahertz radiation is coupled to free space via silicon lens, because of large mismatch in the refractive index (*n*) of GaAs (*n*=3.6) and free space (*n*=1). Later, terahertz pulse is collimated and focused on the sample with one pair of gold coated parabolic mirrors. The transmitted terahertz pulse through the sample is collected by another set of parabolic mirrors, and guided toward terahertz detectors, where silicon lenses are again employed to couple terahertz radiation to detector.

The terahertz detector is also based on photoconductive antenna, which work on the similar principle as the THz emitter. On detector side incoming terahertz field acts as a bias voltage, instead of an externally applied voltage, across two metallic electrodes. The two metallic electrodes, which are deposited on a low-temperature gallium arsenide (LT-GaAs) or ion implanted silicon on sapphire (SoS) substrate, are connected to a current sensor. The duration of terahertz pulse is on the scale of picoseconds, so second part of optical pulse through beam

splitter is used as probe pulse to map the terahertz pulse. As shown in Figure 2.9, a delay stage is introduced

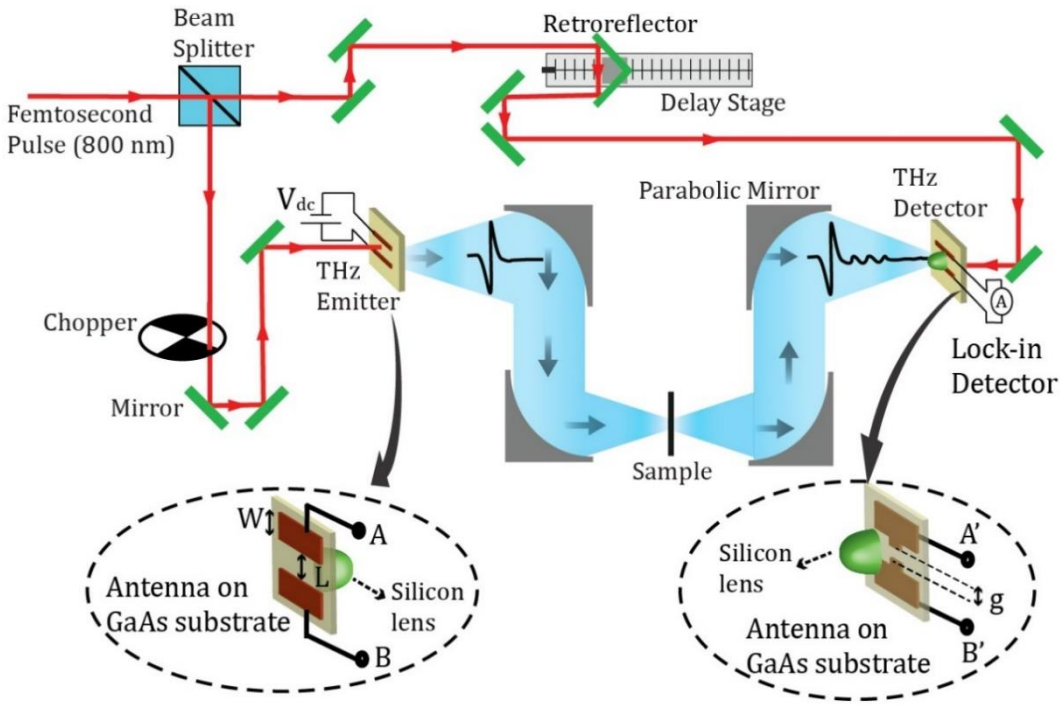

Figure 2.9: Schematic of THz-TDS setup based on photoconductive antenna. Here, zoomed image at the bottom displays terahertz emitter and detector configuration.

to control the optical time delay (τ) between terahertz pulse and optical probe pulse so that the profile of terahertz pulse could be mapped on detector side. Optical pumping the semiconducting area between the two electrodes generates photocarriers, which in the influence of terahertz field are accelerated between the two electrodes of the detector. The photocurrent ($\bar{J}$) induced by terahertz field is given by

$$\bar{J} = \bar{N} e \mu E(\tau) \qquad \ldots\ldots\ldots 2.6$$

where $\bar{N}$ is the photocarrier density, τ is the temporal delay between the optical probe and terahertz pulse and $E(\tau)$ is the temporally mapped terahertz electric field. The generated photocurrent is on the order of nanoampere, so a current amplifier is used to amplify the photocurrent. By recording $E(\tau)$ as a function of τ, THz pulse waveform can be obtained. A lock-in amplifier synchronized with an optical chopper is used to improve the signal-to-noise

ratio of the recorded data. Recorded photocurrent data gives direct mapping of E(τ) as a function of τ, through which the profile of terahertz pulse is obtained. Instead of the intensity of the terahertz waves, this THz-TDS method allows direct measurement of the amplitude and phase information and thus facilitate in obtaining complex optical parameters of the sample. Figure 2.10 depicts time-domain and corresponding frequency-domain spectra of the experimentally generated terahertz pulse from the THz emitter, which has been sampled using photoconductive antenna-based THz detector.

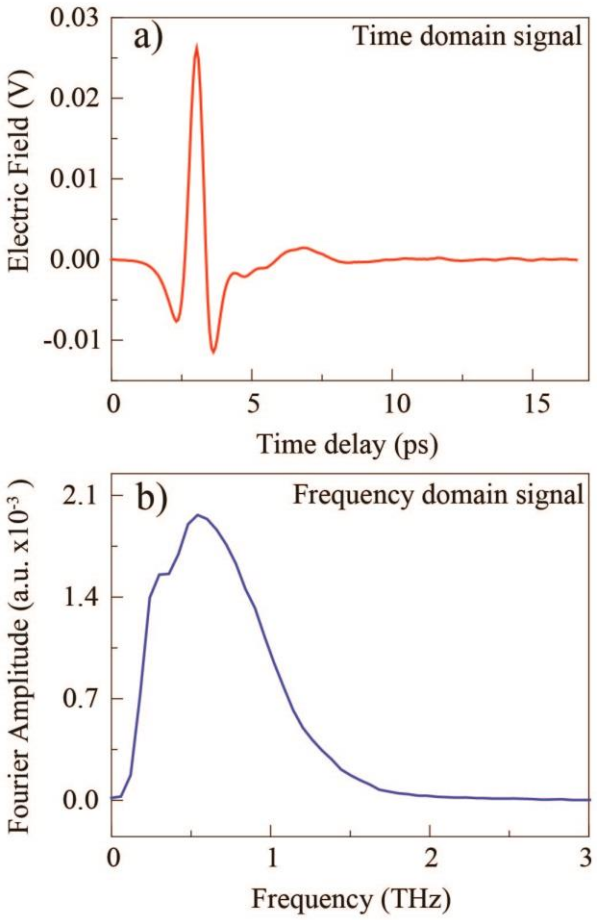

Figure 2.10: (a) Measured time-domain THz transmission signal in the dry N_2 environment using photoconductive antenna-based THz-TDS setup. (b) Corresponding frequency-domain THz transmission signal obtained using Fast Fourier transformed (FFT) of time domain signal.

Experimentally, the THz-TDS of sample is performed in two steps. First, the THz scan is carried out on the metamaterial sample (metal structures on the dielectric substrate), which is

referred to as ‘sample scan’. Then subsequently, a separate THz-TDS scan is performed with the same delay setting for the dielectric substrate that is referred to as ‘reference scan’. The normalized transmission amplitude is obtained as the ratio between the spectral field of sample $\tilde{E}_s(\omega)$ and reference $\tilde{E}_r(\omega)$, which can be given by the following expression

$$\left|\tilde{T}(\omega)\right| = \frac{\left|\tilde{E}_s(\omega)\right|}{\left|\tilde{E}_r(\omega)\right|} \qquad \ldots\ldots\ldots\ldots 2.7$$

Spectral field of sample and reference is calculated by the FFT of time domain signal. These are the complex quantities, which contains the information about the amplitude and the phase of the transmitted THz pulse. We have performed all our THz-TDS measurements in dry N_2 environment, to avoid THz absorption by water molecules that may affect the results.

2.3.2.2 Nonlinear crystal (ZnTe)-based THz-TDS setup

Although photoconductive antenna-based THz setup bring several advantages in terms of stability, low signal-to-noise ratio, and reasonable bandwidth, but have lower peak powers, which limits their capability to measure non-equilibrium dynamics of carriers in materials under the influence of optical illumination. Non-linear crystal-based THz-TDS setup has also acquired enormous interest because of their capability to generate THz pulse with high peak powers and larger bandwidths. Non-linear crystal-based generation and detection of THz waves requires high peak power amplifier laser systems with low repetition rates that also enables more robust optical-pump terahertz-probe (OPTP) spectroscopy setup. In OPTP setup optical-pump (OP) refers to optical pump pulse with high intensity and higher photon energies, which is used to optically excite carriers in materials, whereas terahertz-probe (TP) refers to low energy and lower power terahertz pulse to examine the dynamics of excited carries in materials. We have employed OPTP setup to dynamically tune the electromagnetic resonances of metal-semiconductor hybrid metasurface, where optical pump pulse is used for

semiconductor excitation, and terahertz pulse is used to stimulate metallic resonator in hybrid metasurface.

In our experimental setup pulsed terahertz signal is generated by zinc telluride (ZnTe) non-linear crystal, which generates terahertz waves by the process of optical rectification. Optical rectification is a second order process to generate low frequency or quasi DC polarization in a nonlinear medium by passing intense femtosecond pulse (optical pump beam). Once an optical femtosecond pulse is incident on a nonlinear non-centrosymmetric ZnTe crystal, it generates transient polarization in crystal, and which emits THz pulses. Optical rectification is directly associated with polarization of medium. The Maxwell's equation in a material medium of polarization *P*, magnetization *M* is given by

$$\nabla \times E = -\mu_0 \frac{\partial H}{\partial t} - \mu_0 \frac{\partial M}{\partial t} \quad \ldots\ldots\ldots 2.8\ (a)$$

$$\nabla \times H = \varepsilon_0 \frac{\partial E}{\partial t} + \frac{\partial P}{\partial t} + J \quad \ldots\ldots\ldots 2.8\ (b)$$

$$\nabla . H = -\nabla . M \quad \ldots\ldots\ldots 2.8\ (c)$$

$$\nabla . E = -\frac{1}{\varepsilon_0} \nabla . P + \frac{1}{\varepsilon_0} \rho \quad \ldots\ldots\ldots 2.8\ (d)$$

where *J* and ρ are current and charge densities, respectively. In a dielectric medium,

$$\nabla . H = 0 \quad \ldots\ldots\ldots 2.9\ (a)$$

$$\nabla . E = 0 \quad \ldots\ldots\ldots 2.9\ (b)$$

Using equation 2.8 and 2.9, the inhomogeneous wave equation for induced terahertz light can be derived as

$$\nabla \times \nabla \times E_{THz} = -\mu_0 \nabla \times \frac{\partial H}{\partial t} \quad \ldots\ldots\ldots 2.10\ (a)$$

$$\frac{\partial y}{\partial x} (\nabla \times H) = \varepsilon_0 \frac{\partial^2 E_{THz}}{\partial t^2} + \frac{\partial^2 P^{NL}}{\partial t^2} \quad \ldots\ldots\ldots 2.10\ (b)$$

$$\nabla . (\nabla . E_{THz}) - \nabla^2 E_{THz} = -\frac{1}{c^2} \frac{\partial^2 E_{THz}}{\partial t^2} - \mu_0 \frac{\partial^2 P^{NL}}{\partial t^2} \quad \ldots\ldots\ldots 2.11$$

The equation 2.11 transform to an inhomogeneous wave equation on using equation 2.8

$$\nabla^2 E_{THz} - \frac{1}{c^2}\frac{\partial^2 E_{THz}}{\partial t^2} = \mu_0 \frac{\partial^2 P^{NL}}{\partial t^2} \qquad \ldots\ldots\ldots 2.12$$

The induced polarization could be expressed as Taylor's expansion of the form

$$P(t) = \chi^{1'} E(t) + \chi^{2'} E(t)^2 \qquad \ldots\ldots\ldots 2.13$$

where χ^1 and χ^2 represent the first and second order electric susceptibility tensor. On substituting $E(t) = A(t)\cos(\omega_0 t)$ in equation 2.13, polarizability can be expressed as

$$P(t) = \chi^{1'} A(t)\cos(\omega_0 t) + \chi^{2'}\left(\frac{A(t)^2}{2} + \frac{A(t)^2\cos(2\omega_0 t)}{2}\right) \qquad \ldots\ldots\ldots 2.14$$

The coefficient of χ^2 leads to transient polarization which is responsible for the THz generation from an optical pulse of pulse width 50-150fs. Figure 2.11 shows the nonlinear crystal-based THz-TDS setup, where laser pulse of wavelength 800 nm and pulse width 120 fs is used to pump <110> axis cut ZnTe crystal (THz emitter) for generation of THz pulse. Since ZnTe crystal is transparent to incoming laser pulse, an optical filter is used to attenuate laser pulse completely. Generated terahertz travels through optical filter with negligible attenuation and guided towards the sample with the help of parabolic mirrors.

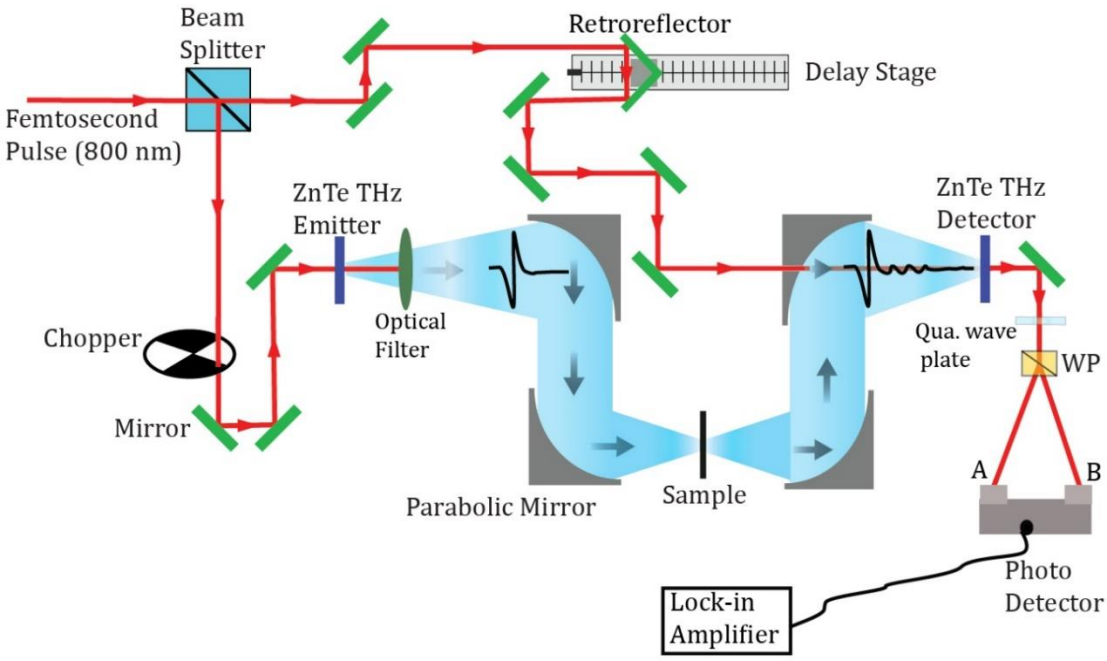

Figure 2.11: Schematic representation of ZnTe nonlinear crystal-based THz-TDS setup.

The detection of terahertz pulse through the sample is realized through electro-optic sampling, where electric field of incoming terahertz pulse influences the optical properties of a second birefringent nonlinear ZnTe crystal. This kind of detection mechanism is based on Pockel's effect, where strong terahertz field introduces anisotropy in ZnTe crystal, which in turn changes the polarization of low intense optical beam passing through the ZnTe detector crystal. In absence of terahertz pulse, optical properties of ZnTe crystal are isotropic. The terahertz wave polarized in the XY plane and oriented at an angle 45° to the X axis, modifies the index of refraction along X and Y direction, while index of refraction along Z direction remain unaffected, as per equation 2.15 given below:

$$n_x = n_0 + \frac{1}{2} {n_0}^3 r E_{THz} \qquad \ldots\ldots\ldots 2.15\ (a)$$

$$n_y = n_0 - \frac{1}{2} {n_0}^3 r E_{THz} \qquad \ldots\ldots\ldots 2.15\ (b)$$

$$n_z = n_0 \qquad \ldots\ldots\ldots 2.15\ (c)$$

where n_0 is the refractive index without terahertz electric field incidence, r is the electro-optic constant and E_{THz} is the electric field of the terahertz radiation. The changes in n_{x} and n_{y} are equal in magnitude and opposite in sign. More interestingly, the change in magnitude is proportional to the E_{THz} and thus the optical response leads to direct measurement of the electric field passing through the crystal.

The optical path length of femtosecond optical beam is matched with the generated terahertz beam, before passing them through the ZnTe detector crystal. The change in polarization of optical beam due to birefringence induced in crystal by terahertz pulse, is detected by transmitting it through a quarter-wave plate followed by a polarizing prism (Wollaston prism (WP)) which splits the beam into two orthogonal components which are measured individually by a pair of photodiodes. The change in polarization is proportional to differential current through photodiodes, thus allowing direct measurement of terahertz field. The differential

current is amplified and converted to voltage signals using pre-amplifier. Voltage signals are recorded using lock-in detection mechanism to improve the signal-to-noise ratio. The wavelength of terahertz pulse is considerably large compared to optical pulse, so by introducing time delay through delay stage terahertz pulse profile is measured at discrete intervals. Complete terahertz pulse profile could be traced by controlling the time delay between optical pulse and terahertz pulse.

Besides terahertz generation and detection in ZnTe based THz-TDS setup, a beam of laser is also used to optically pump the sample to realize robust OPTP setup. For dynamic tuning of metamaterial samples, optical pump beam of higher fluence is used to excite carries in semiconductor, which influences the terahertz excitation of samples. For OPTP setup it is important to ensure that terahertz pulse and optical pump pulse should strike the sample simultaneously. This time matching is employed by adding another delay stage in the path of optical pump, so that terahertz response could be captured at instance of maximum excitation. This additional delay stage scheme also allows the terahertz beam to probe the ultrafast dynamics at various stages of non-equilibrium excitation. In our course of work, we employed this setup to realize the switching response of toroidal metamaterial samples.

Chapter 3

Sharp Toroidal Excitation in Planar Metasurface

This chapter briefly introduces the importance of toroidal excitation for tailoring loss channels in metamaterials at terahertz frequencies. In this work, a strategy has been devised to excite toroidal resonance in planar metasurface. The importance of toroidal excitation has been experimentally demonstrated by tuning the radiative losses, which has an important role in enhancing performance of planar metadevices.

3.1 Introduction

Over the last decade, naturally occurring and artificially designed structures are of immense interest in the domain of photonics for tailoring electromagnetic radiation. Array of artificially designed structures, which are also known as metamaterials, have unit cell dimensions on subwavelength scale compared to wavelength of the incident electromagnetic waves. The unit cell contains resonating elements, which resonates at desired frequency of electromagnetic radiation. Tailoring the geometrical parameters such as shape, size of resonators, and periodicity of unit cells, many exotic features have been discovered, which have tremendous potential application such as plasmonic biosensors, plasmonic absorbers, negative index media, reconfigurable metadevices and super lensing.[27,93-95] The electromagnetic response of

metamaterials is decided by the resonating structures in individual unit cells, whose microscopic response can be related to macroscopic response of metasurface in terms of multipole decomposition (Sec. 1.3). The microscopic response of unit cell could be effectively represented as a combination of few dominant multipole excitations, such as electric and magnetic dipoles, quadrupoles, etc. of multipole family. The subwavelength feature of unit cell allows to apply homogenization principle, in which effective electromagnetic response of metamaterial is analyzed similar to the electromagnetic response of naturally occurring media. Currently, photonic community has shifted its interest to virtually little-known toroidal multipole, third family member of electromagnetic multipoles, which along with the familiar electric and magnetic multipoles are significantly important to completely understand the far-field radiation pattern of a random radiating source. The toroidal dipole could be visually understood as a circular arrangement of head-to-tail arrangement of magnetic dipoles, all densely packed into a very small domain of space.[96] In 1957, toroidal dipole was first reported by Zel'dovich in the context of particle and nuclear physics, where elementary particles violate parity symmetry.[53] In spite of having such unique current density, toroidal dipole is not a part of standard multipole expansion. The interaction energy of dynamic toroidal dipole is determined by the time derivatives of electromagnetic fields, rather than by the field themselves. Far field radiation pattern of toroidal dipole is identical to that of the electric dipole, so experimentally it is impossible to separate out the scattering contribution of toroidal dipole from electric dipole.[56] So far, toroidal dipole moments have been identified in ferroelectric systems and molecular structures.[97,98] Recently, *toroidal* dipolar *response* was demonstrated in *metasurfaces at microwave regime.*[73,78,80] It has been shown that artificial media with strong toroidal dipole response exhibits many unique electromagnetic phenomena such as unconventional optical activity,[77,99] resonant transparency,[100] and could even give rise to negative refraction.[101] Usually the response due to toroidal dipole (dynamic poloidal currents

flowing on the surface of a torus along its meridians) are too weak to be analytically observed, as compared other dominant electric and magnetic multipoles, which are simultaneously excited during electromagnetic excitation of metasurface.[102] However, the response due to toroidal dipole could be strengthened through meta-molecule design with toroidal or torus topology. Another approach aiming towards the enhancement of toroidal excitation is to suppress the excitation of fundamental as well as higher order multipoles belonging to the family of electric and magnetic multipoles. To stimulate toroidal excitation in metamolecules one should intend to confine the oscillating magnetic flux inside the metamolecules into tight loops, this spatial arrangement corresponds directly to the toroidal dipole excitation. In microwave regime, many three-dimensional (3D) metasurface have been proposed theoretically and realized experimentally which manifest dominant toroidal excitation.[84,103] Nevertheless, realization of true three dimensional structures becomes challenging during fabrication processes as the dimension of resonator approaches micro and nano-scale, as their operational frequency shifts to terahertz or optical regime. In this chapter we would show a toroidal dipole excitation in a 2D metamaterial that could be fabricated in a single step UV lithography technique.

In contrast to 3D metasurfaces with torus topology, the 2D metasurfaces offer relatively weak confinement of oscillating magnetic field in small circular region, nevertheless, by careful choice of unit cell geometry of metamaterial array, one could suppress undesired multipoles to reveal the scattering contribution of toroidal dipole. In this chapter our study is centered on toroidal dipolar response in two-dimensional (2D) metasurface structure (as depicted in figure 3.1a), whose resonant scattering response lies in the terahertz region of electromagnetic spectrum. In our metamaterial unit cell design contains composite of two metallic double split gap resonators, which are joined along one branch in mirror facing arrangement. Joining metallic resonators in this mirrored facing arrangement leaves one unit cell resonator with two

metallic loops, and with two capacitive gaps in each loop. By varying the gap location symmetrically for the left and right portion of composite resonator it is possible to excite a resonant mode by the incoming electric field polarization of the incident field, in which the currents in the two loops of each metamolecule in the unit cell oscillate in opposite directions. This mode is always accompanied by another mode in frequency spectrum, where current in all branches are parallel in nature. For the time being, we focus only on excitation mode where oscillating currents flow in opposite direction. This mode could be tailored through appropriate positioning of gaps, such that the excitation results in a suppressed electric and enhanced toroidal dipole response. This composite metamaterial is different that conventionally known ELC metamaterial, in which the counter-propagating induced currents in the two loops of the ELC resonator results in a dominant electric dipole response, which suppresses the scattering contribution of all other multipole excitations.[104]

3.2 Multipole contribution of toroidal dipole

Frequency dependent toroidal component for different position of gaps in the sample have been calculated analytically through *LiveLink*^{TM} *to Matlab* feature of Comsol Multiphysics and Matlab programs. To analyze the electromagnetic excitation analytically through multipole decomposition, it will be assumed throughout this paper that the metasurface is uniformly excited by the incident plane-wave radiation normal to the plane of metasurface. Uniform excitation ensures that all the resonators are oscillating in same phase with respect to each other. It has been previously discussed (see Sec. 1.3) that under such particular condition one could represent in-plane projections of multipolar representation of the scattering by a single unit cell as a plane-wave scattering of the whole metasurface array.[72] If the metasurface array lies in the XY-plane, we could focus our attention to component of the toroidal dipole vector lying in the plane of metasurface (XY-plane), which is given by $\mathbf{T}_{||} = T_x\hat{x} + T_y\hat{y}$(toroidal component

parallel to the plane of metasurface), where $\hat{x}, \hat{y}$ are the unit vectors in the direction of X and Y axis. The subscript $(\ldots)_{\parallel}$ denotes the projection of vector into the metasurface plane.

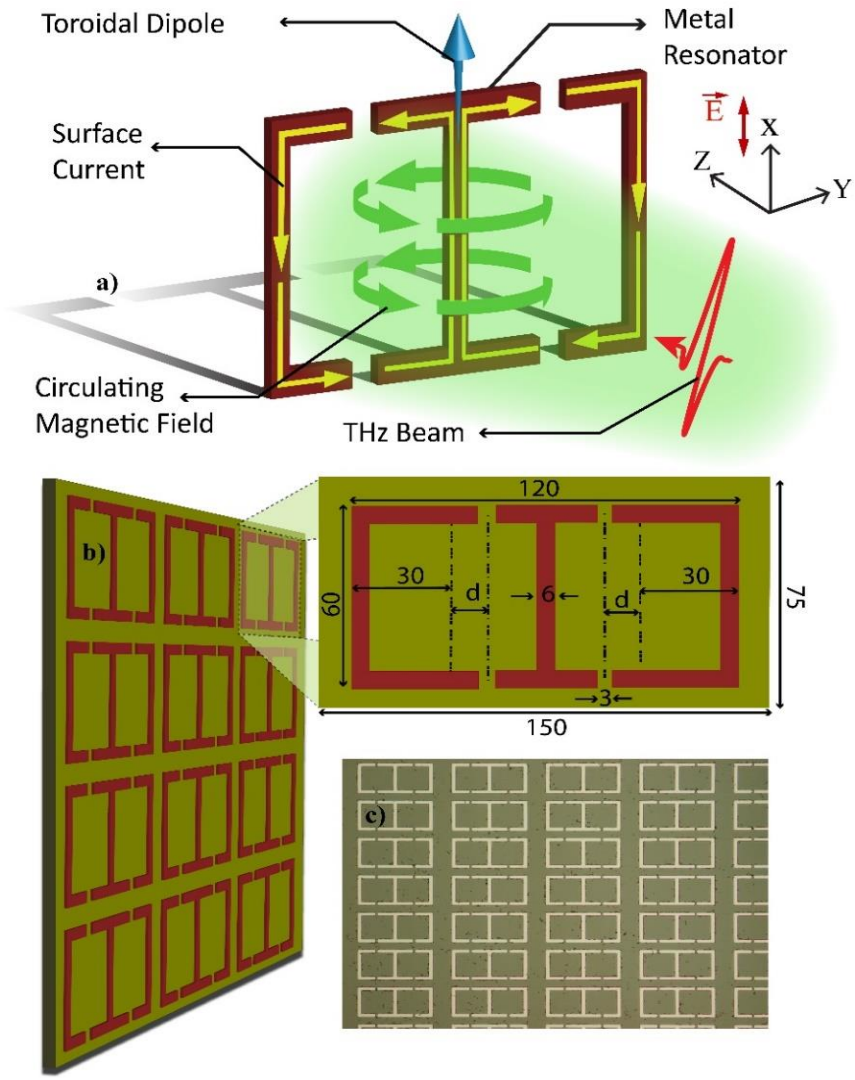

Figure 3.1: (a) Schematic of toroidal dipole vector represented by tightly confined oscillating magnetic field (around the fictitious arrow) generated by current carrying loops. (b) Schematic representation of metasurface array, where highlighted unit cell contains structure of resonator (all dimensions are in micron), *d* indicates the shift of the pair of gaps located on the left and right portion of resonator. (c) Microscopic image of the fabricated metasurface.

In below given analysis we have not considered scattering contribution perpendicular to the plane of metasurface because in case of scattering by an array of dipoles lying in the XY-plane, the z-components of the individual dipole scattering does not contribute to the net far-field

radiation from the array. Far field component of electric field ($\boldsymbol{E_{s-t}}$) scattered by an array of exactly alike toroidal dipoles is given by the equation:

$$\vec{E}_{s-t} = -\frac{\mu_o c^2 k^2}{2\Delta^2}\vec{T}_{|\ |}\, exp(-ikR) \qquad \ldots\ldots\ldots (3.1)$$

If we consider first eight dynamic multipoles, then net electric field ($\vec{E}_s$) emitted by the array with induced oscillations of charge-current density is the vector summation of field due to all contributing multipoles, which has been already discussed in chapter 1, could be related to below given equation (see Sec. 1.3, equation 1.6)

$$\vec{E}_s = \frac{\mu_o c^2}{2\Delta^2}\Big[-ik\vec{p}_{||} + ik\hat{R}\times\left(\vec{m}_{||} - \frac{k^2}{10}\vec{m}^{(1)}_{||}\right) - k^2\left(\vec{T}_{||} + \frac{k^2}{10}\vec{T}^{(1)}_{||}\right) + k^2\left(\vec{Q}^{(e)}.\hat{R}\right)_{||}$$

$$-\frac{k^2}{2}\hat{R}\times\left(\vec{Q}^{(m)}.\hat{R}\right)_{||} - \frac{ik^3}{3}\left(\vec{Q}^{(T)}.\hat{R}\right)_{||} + ik^3\left(\left(\vec{O}^{(e)}.\hat{R}\right).\hat{R}\right)_{||}$$

$$-\frac{ik^3}{180}\left(\hat{R}\times\left(\left(\vec{O}^{(m)}.\hat{R}\right).\hat{R}\right)_{||}\right)\Big].exp(-ikR) \qquad (1.6)$$

The net transmitted field of radiation by the two-dimensional array, could be calculated by adding up the scattered radiation by the array and the incident radiation.

$$\vec{\mathbf{E}}_{\text{transmitted}} = \left[\vec{\mathbf{E}}_{\mathbf{s}}\right]_{\hat{\mathrm{R}}=\hat{\mathrm{k}}} + \vec{\mathbf{E}}_{\text{incident}} \qquad \ldots\ldots\ldots (3.2)$$

where ' $\hat{\mathrm{k}}$ ' unit vector points in the direction of propagation of incoming radiation (perpendicular to the plane of metasurface).

3.3 Tuning of toroidal excitation in resonator array

In this work, we have demonstrated tailoring of toroidal dipolar response, by symmetrically moving the pair of capacitive split gaps toward the center of unit cell, which are located at left and right portion of composite resonator (see figure 3.1b), and the impact of toroidal component on the overall scattered intensity of the transmitted light. We analytically and

experimentally examine the electromagnetic response of a dimensional (2D) array of planar resonators with toroidal topology (composite of two double split SRR). The unit cell of metasurface is shown by the highlighted image in figure 3.1b, where the design parameters of resonator with planar toroidal topology have been indicated. The dimensions of the resonator are chosen to excite resonant electromagnetic response between 0.2-1.0 THz. The unit cell of metasurface consist enlarged double ring SRR with four split gaps, which could be seen as joining of two double split square shaped SRRs.

3.3.1 Device fabrication and numerical simulation

Experimentally, the array of SRRs fabricated on polished 500 μm thick high resistivity silicon (p-type) substrate, by thermally depositing 200 nm thick aluminum (Al), as depicted by the microscopic image of sample in figure 3.1c. The outermost dimension of each composite resonator is 120 μm × 60 μm and the periodicity of the unit cell in the array is 150 μm × 75 μm. The size of capacitive split-gap is 3 μm and metallic strip width of the resonator arm is 6 μm. The terahertz electromagnetic field is incident normal to the plane of resonator array sample, having its electric field component perpendicular to the gaps in the metamolecules. Initially pair of gaps on the left and right side of resonator are located at the center of each loop, which is at the distance of 30 μm (d = 0 position) measured from the side branch as indicated by the graphic image of the zoomed unit cell in figure 3.1b. All numerical simulations were carried out in commercially available software CST Microwave Studio and Comsol Multiphysics. Frequency domain analysis approach with unit cell/periodic boundary condition have been used to effectively analyze the electromagnetic response of metasurface. For accurate numerical analysis it has been ensured that material properties taken in simulations are similar to experimental samples. CST simulations followed by experiments have been performed for different configurations in which the pair of gaps are moved together by distance

d symmetrically towards the center of resonator. For simulations, aluminum metal was described using the Drude model, where frequency dependent material parameters is represented by the permittivity by given expression $\varepsilon(\omega) = \varepsilon_{\infty} - \left[\omega_p^2 \Big/ \omega(\omega + i\Gamma) \right]$, where ω_p is the plasma frequency (22.43×10^{15} rad/sec for Al) and Γ is the damping rate (124.34×10^{12} rad/sec).[105] Toroidal excitation could be stimulated by the incident terahertz field (E_x) parallel to non-gap arm of resonator.

3.3.2 Experimental analysis

Figure 3.2 shows the simulated and experimentally measured transmittance spectra of fabricated samples having different position of gaps specified by distance *d* (towards the central strip of the metamolecules). As *d* changes, the strength of toroidal excitation is modulated in terms of amplitude and line-width of resonance. The asymmetric toroidal resonance first disappears (*d*~5 μm) and then again reappears for higher values of *d*. The line-width of toroidal resonance first decreases then increases as a function of *d.* The line-width of resonance could be directly related to quality factor (*Q*) of resonance, which represents the strength of cavity in trapping the photon. Here, the *Q*-factor is calculated by the transmitted intensity curve, which is defined as the ratio of resonance frequency to the full width at half maximum (FWHM). The *Q* factor of asymmetric line shape narrow resonance has been determined by considering the lowest dip and highest peak of the transmittance spectra. There is a good correspondence between the simulated and measured transmission spectra of the metasurface. The *Q*-factor in experimental results is broader than the simulation results. This broadness of the spectrum can be attributed to the scattering or diffraction losses due to imperfections arising from the fabrication processes. Fano fit formula given by equation 3.3 has been used to determine

resonance frequency and line-width of resonance, so that *Q*-factor could be calculated precisely:[38]

$$T_{Fano} = \left|\left(a_1 + ja_2 + \frac{b}{(\omega - \omega_0 + j\gamma)}\right)\right|^2 \qquad \ldots\ldots\ldots (3.3)$$

where a_1, a_2 and b are a constant real number, ω_0 is the Fano resonance frequency, and γ is the overall damping rate of the resonance.

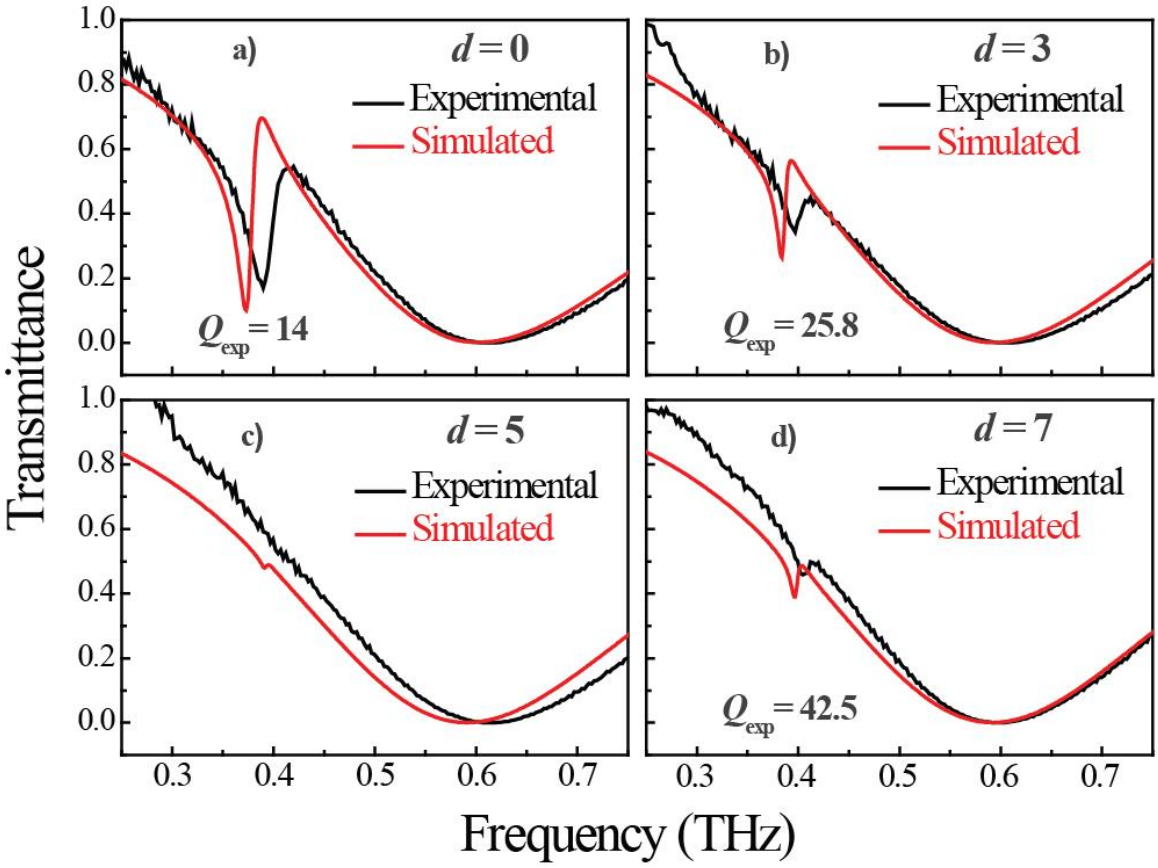

Figure 3.2: Transmittance spectra (experimental (red curve) and simulated (black)) for the resonator array having different position of split gaps specified by *d* (0, 3, 5 and 7 μm). The quality factor of the resonances in (a, b, d) is given as a subscript.

The transmittance and Fano fitted curves are shown in figure 3.3 for two different positions of split gaps indicated by *d.* The fitting has been performed over the frequency range 0.33THz to 0.39 THz, in the vicinity of asymmetric line shape, as the fitting model discussed above only encompasses the asymmetric line shape resonance and does not include the broad resonance.

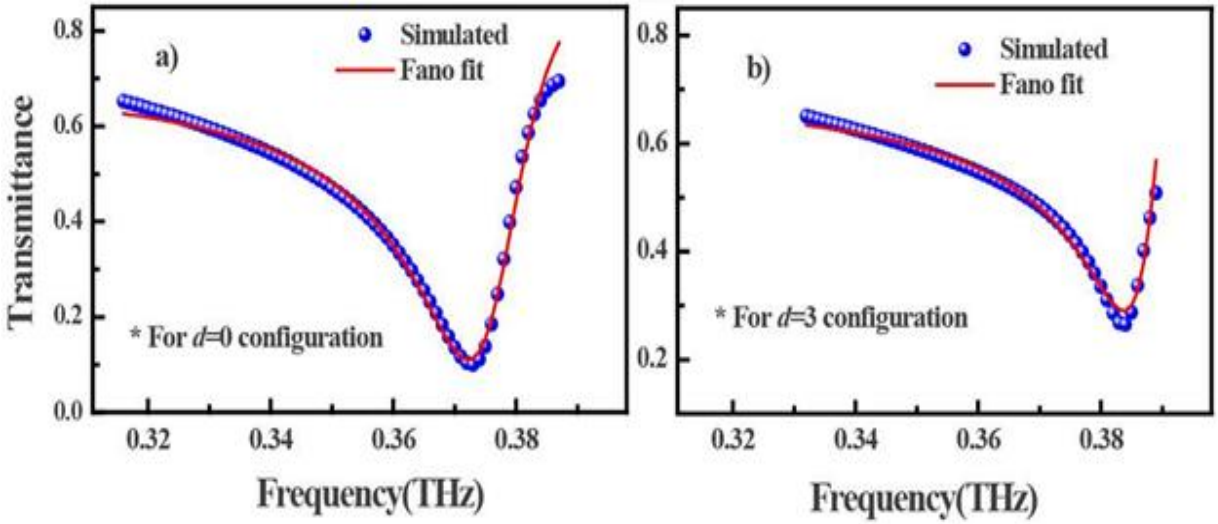

Figure 3.3: Fano fitting of transmittance spectra curves at gaps position (a) d=0 μm and (b) d = 3 μm.

3.4 Effect of toroidal dipole in far-field electromagnetic scattering

Now, we will investigate the dependence of toroidal multipoles in determining the electromagnetic response of the metasurface. For the simplification of analysis all higher order toroidal multipoles have been not taken into account. Because as we move to higher order multipoles, the strength of far-field response decreases by two orders of magnitude. So, the contribution due to toroidal dipole and toroidal quadrupole would provide a notable contribution to the metasurface far-field response. So, to simplify the analysis, all higher toroidal multipoles could therefore be ignored. Simulated transmitted intensity (transmittance) spectra in figure 3.4a shows the transmittance curve with and without toroidal multipole, computed through multipole analysis, for the metasurface sample for gap position (d) of 3 μm. Multipole computation (see section 1.3 for more details) clearly reveals that toroidal dipole excitation enhances transmission at frequencies below 0.4 THz and diminishes the transmission above 0.4 THz. Since in all resonator electric dipole dominates the transmission spectra, so we conclude that below frequency of 0.4 THz the toroidal dipole interferes constructively with

electric dipole, while for frequencies above 0.4 THz it destructively interferes with electric dipole. The unit cell of metasurface is designed to dominate toroidal excitation along the incoming electric field polarization. X-component of the toroidal dipole (T_x) excitation for metasurface with different position of gaps *d* (metamaterial design has dominant toroidal dipole component along X-axis) is depicted in figure 3.4b. The relationship between the strength of toroidal excitation and the position of the gap is non-trivial: from *d*=0 μm to *d*=3μm, the toroidal dipole excitation is suppressed, whilst from *d*=5μm and *d*=7 μm there is enhancement in the strength of toroidal dipole moment.

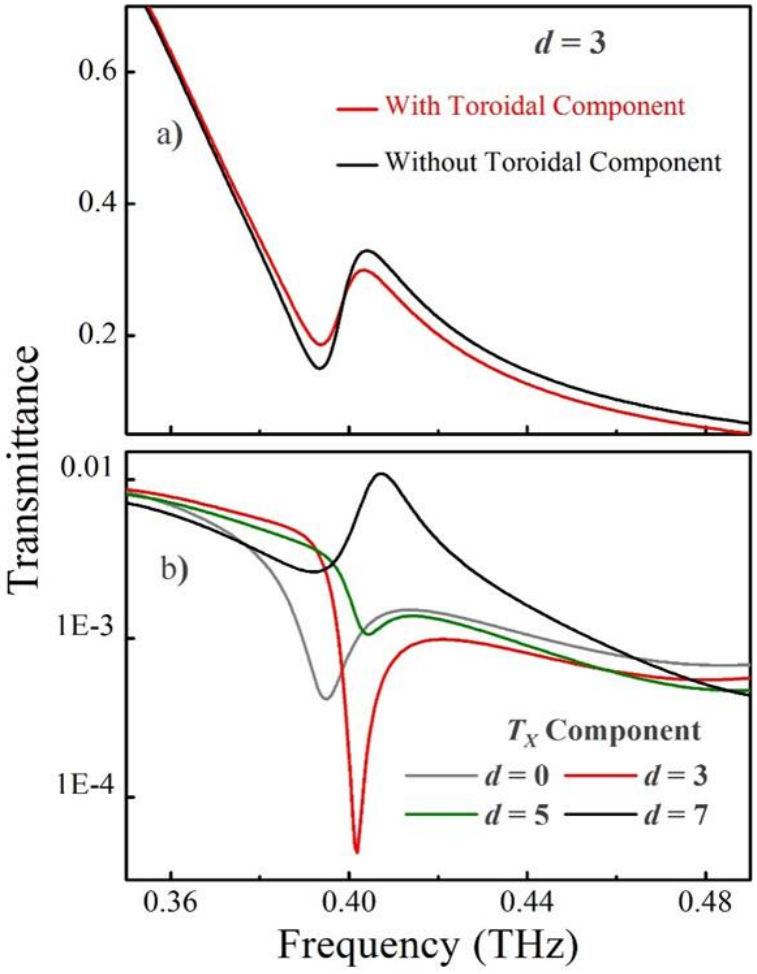

Figure 3.4: (a) Transmitted intensity calculated via multipole analysis, in presence and absence of toroidal component for sample with split gap position specified by *d* = 3 μm. (b) Variation in X-component of toroidal dipole ($\mathbf{T_x}$) computed by multipole decomposing for different split gap location (d) in the sample.

3.5 Role of substrate in toroidal excitation

To highlight the dependence of T_x on d, figure 3.5 highlights the strength/amplitude of toroidal dipole at resonance for different gap locations. This non-trivial dependence reveals the impact of the substrate on electromagnetic response of metasurface. Since, the substrate is 0.5 mm thick high-resistivity p-type silicon, which, at radiation frequency of 0.4 THz corresponds to slightly more than two wavelengths of radiation along the length of substrate (using refractive index 3.4).[106] This feature is deliberate, in fact using only planar currents it is unfeasible to excite dominant toroidal dipole response, because it has to compete with magnetic quadrupole excitation. By carefully choosing the thickness of substrate, the electromagnetic response of the metasurface is augmented by the Fabry-Perot type cavity resonance in the substrate. Two co-planar counter-propagating current carrying loops correspond to a mixture of toroidal dipole and magnetic quadrupole excitation, however the displacement currents engaged in the substrate of the

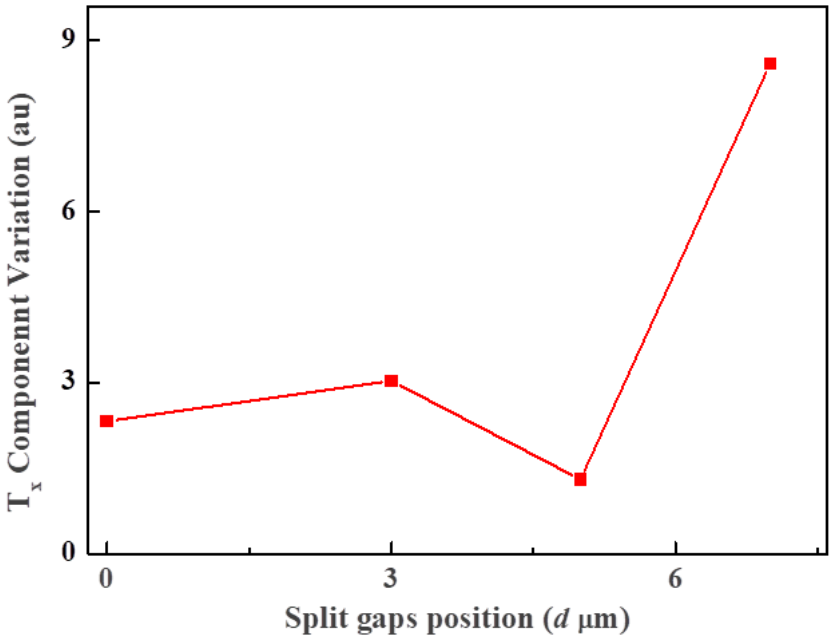

Figure 3.5: Numerically calculated toroidal dipole component ($\mathbf{T_x}$) as a function of split gap position (d), at frequencies of electromagnetic resonance.

metasurface add to an extra magnetic dipole that could be supportive to toroidal dipole or magnetic quadrupole. If this extra magnetic dipole is in accordance with other two magnetic dipoles to create circular head-to-tail arrangement of magnetic dipoles conditions, then the toroidal dipole excitation is dominant. Since the standing-wave mode in the dielectric substrate with array of metallic resonators on one of its faces cannot be described precisely, we must numerically optimize the toroidal dipole response, which is achieved by choosing a favorable gap position *d*, as shown in figure 3.4b and figure 3.5.

3.6 Surface current and magnetic field

Further, to verify the impact of toroidal excitation in terms of excitation of SRRs, figure 3.6 shows the current density and magnetic field induced for different location of split gaps in the unit cell of metasurface. Magnetic field plot shows the amount of circulating magnetic flux established between two loops of resonator responsible for toroidal excitation. For d=0 μm and d=3 μm T_x is weak, and for these positions of split gaps we see the current is stronger in the central metallic strip compared to antiparallel current on edge-strips (figure 3.6a, 3.6c). This antiparallel current distribution establishes circulating current in each loop, which flows in opposite direction that induces toroidal excitation. The large imbalance in current density weakens the toroidal dipole, due to weaken anti-aligned set of magnetic dipoles, while it makes dominant contribution of electric dipole. The weakening of toroidal excitation could be understood by looking circulating magnetic field between loops (figure 3.6b, 3.6d) which is not uniformly distributed (more concentrated at center). At d is equal to 5 μm, induced currents density in central branch and side branches of the resonating structure are parallel in nature (figure 3.6e) which further enhance contribution of electric dipole and suppresses toroidal excitation. The signature of suppression in toroidal excitation for d=5 μm could be seen in figure 3.6f, where there is no significant circulating magnetic field established between two

loops of resonator. Finally, at *d*=7 μm (figure 3.6g), there is relatively small mismatch in the current in the central branch to the antiparallel currents in the side branch of resonator, which

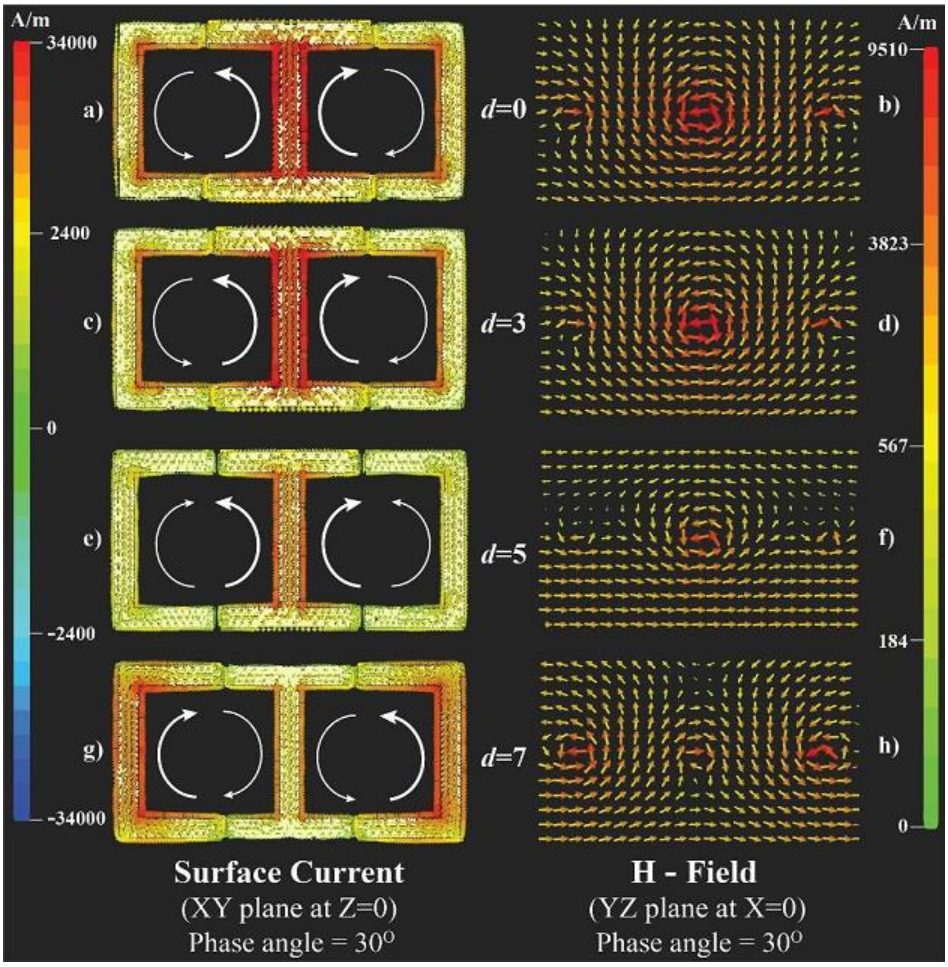

Figure 3.6: Surface currents (a, c, e, g) and H-field (b, d, f, h on YZ plane at X=0) estimated through numerical simulations for the resonator at asymmetric resonance, for different location of split gaps (*d* = 0, 3, 5, and 7 μm).

strengthen anti-aligned set of magnetic dipoles, hence enhances toroidal dipole excitation and simultaneously it weakens electric dipole. In this situation, toroidal coupling is established between two neighboring unit cells. As we could see in figure 3.6h circulating magnetic lines are uniformly distributed around the side branches of resonator.

Before making the concluding remark, we would like to highlight the point that the response of our metasurface is analogous to well-known Fano resonance.[107-109] Fano resonance is a

asymmetric line-shape resonance phenomenon arises from the bright field and dark field interference. As one could see from the measured response in figure 3.2, the resonant response of our metasurface is also associated with an asymmetric transmission window, a hall-mark of Fano resonance, which, in our case, arises as a result of coupling between the electric dipole, which is a ‘bright mode’, and the toroidal dipole, which is a ‘dark mode’.

3.7 Conclusion

In this work, investigation has been done on the tailored response of the sharp toroidal dipolar resonances in planar terahertz metadevice containing array of composite SRRs structure. Tuning of toroidal resonance in terms of amplitude, line-width, and quality factor has been accomplished by symmetrically tailoring the location of split gaps of resonating structure. These low loss, high-*Q* resonances offer another route to tailor loss mechanism that could be effective in designing devices for potential applications such as modulators, lasing spasers and ultrasensitive sensors. Our finding offers a simple scalable planar metasurface design for excitation of toroidal modes in the terahertz regime and a similar approach with planar metadevices could be applied for excitation of these exotic toroidal modes at higher frequencies.

Chapter 4

Toroidal Coupling of Fano Resonators in Metasurface

Radiative losses are crucial in optimizing the performance of metamaterial-based devices across the electromagnetic spectrum. Introducing structural asymmetry in meta-atom design leads to the excitation of sharp Fano resonances with reduced radiative losses. However, at larger asymmetries, the Fano resonance becomes highly radiative which results in the broadening of the asymmetric line shaped resonances. In this chapter, we experimentally demonstrate a scheme to couple mirrored asymmetric Fano resonators through interaction of anti-aligned magnetic dipoles which results in a *toroidal coupling* in two-dimensional planar metasurface. The quality (Q) factor and the *figure of merit* of coupled toroidal dipolar mode resonance is significantly higher than conventional Fano resonance. Moreover, we discover that the exponential decay of the Q factor of coupled toroidal dipolar mode resonance occurs at half the rate of that in the Fano resonance as the asymmetry of the system is enhanced which indicates significant tailoring and the suppression of the radiative loss channel in the toroidal configuration.

4.1 Introduction

Manipulating electromagnetic (EM) waves has led to the development of wide range of technologies to communicate, control, monitor, and detect the information concealed in the

form of EM waves. Metamaterial artificial structure based photonics devices which are designed to yield a desired resonant response to EM radiation offers various optical functionalities, such as slow light, negative refractive index, optical modulation, lasing spaser, and invisibility cloaking, which leads the path for technological advancement in near future.[22,25,29,74,110] Despite, these exotic features the performance of metamaterials is limited by radiative and non-radiative loss mechanisms.

In order to make efficient resonant metamaterial devices, the nature of their response should be of high quality factor. Non-radiative losses can be optimized by tailoring the conductivity of metamaterial resonators. On the other hand, dominant radiative losses can be controlled by optimizing the geometry of the metallic subwavelength structure to excite sharp asymmetric resonant response widely known as Fano resonances.[107,108,111] Fano resonances arise due to interference between narrow discrete mode and a broad spectrum.[112] It has been shown that such resonances can be excited merely by breaking the structural symmetry of the meta-atom.[113-115] Recent demonstrations have revealed magnetic-based Fano resonances at mid-infrared and optical frequencies.[116-118] At the Fano resonance, the radiating source is weakly coupled to the free space, which in turn drastically reduces the radiative loss in the metamaterial and plasmonic systems. Radiative loss due to Fano resonance could be engineered by tailoring the structural asymmetry which influences the linewidth and amplitude of resonance. Nearest neighbor coupling of meta-atoms provides an additional approach to further tailor the radiative loss of Fano resonance.

4.1.1 Asymmetric fano resonator for tailoring radiative-loss

Electromagnetic (EM) response of terahertz asymmetric split ring resonator (TASR) with respect to the incident EM wave having its electric field parallel to the non-gap arms of TASR

leads to a broad symmetric line shape dipolar resonance and narrow asymmetric line shape Fano resonance in the transmission spectra. Figure 4.1a shows the simulated normalized transmittance spectra in which broad resonance appears at 0.72 THz and Fano resonance appears at 0.479 THz. The surface current at these resonances have been shown in figure 4.1b, 4.1c. At dipolar resonance we observe parallel currents in both strips (figure 4.1b) which are strongly coupled to free space and, hence, this resonance is broad due to its highly radiative nature. At Fano resonance the radiation pattern, due to anti parallel current in both strips (figure 4.1c), interfere destructively, which in turn decreases the radiative loss. This type of current configuration is coupled weakly to free space, which leads to narrow down the line width of resonance, at the same time high current density is confined along metallic strips. The nature of resonance mode at Fano resonance is similar to inductive-capacitive (*LC*) resonance.

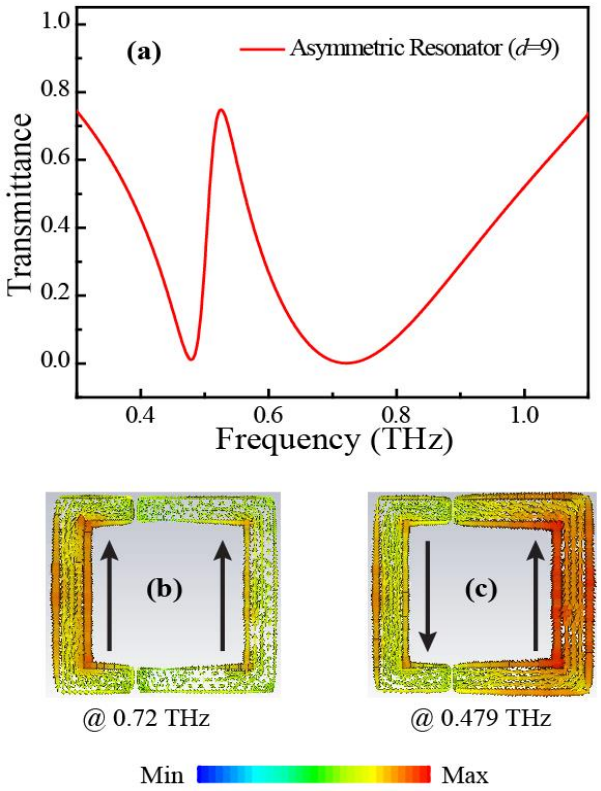

Figure 4.1: a) Simulated transmittance spectra of TASR, showing broad and narrow resonance. b, c) Simulated current intensity at broad (b), and narrow (c) resonances.

The high quality factor asymmetric Fano line shape resonance in the TASR arises from the structural asymmetry which leads to an interference between a sharp discrete resonance and a much broader continuum-like spectrum. At Fano resonance the difference in anti-parallel current density along both the strips can be visualized as an overlap of electric and magnetic dipoles. Therefore, the appearance of Fano resonance is related to the coupling between a broad "electric" and a sharper "magnetic" dipolar mode.

4.1.2 Toroidal coupling for loss engineering

In addition, to minimize the loss due to radiation it is extremely important to know the radiation pattern emitted by a radiating source. An arbitrary radiating metamaterial surface can be represented by an array of oscillating charge and loop currents, which involves the traditional concept of electric and magnetic multipoles respectively. Recently, realization of virtually unknown third family of electromagnetic multipole, the toroidal dipole, has become equally important for the complete multipole analysis of an arbitrary radiating source.[70,72,73] Dynamic toroidal dipole has the ability to enhance field confinement by concentrating time varying magnetic field in a small circular region. It can be visualized as a head to tail arrangement of magnetic dipoles along a circular path.[96] As we shift from lower to higher frequencies, the interaction energy of toroidal dipoles increases since their strength depends on time derivative of electromagnetic waves. Also, metamolecules with subwavelength dimensions weakly scatter the electromagnetic waves due to toroidal dipoles in comparison to the electric and magnetic dipoles. Several 3-D metamaterial designs with signature of toroidal excitation have recently been demonstrated.[17,80,84] Artificial media with strong toroidal dipole response exhibits many unique electromagnetic phenomena such as unconventional optical activity, and resonant transparency.[99,100,119] Moreover, radiating toroidal dipole can interfere destructively with radiating electric dipole to give non-radiating configuration, known as anapole.[70,120] This

added advantage can further improve the performance of a device by exciting resonance modes that support toroidal resonances. Therefore, both Fano and toroidal resonant excitation can produce radiation patterns that couple weakly to free space which subsequently enhances the field confinement within a small volume. However, it is important to distinguish their resonance response.

4.1.3 *Q*-factor and FoM as a measure of performance

The performance of a photonic device at electromagnetic resonance is determined by the *Q* factor of the resonance response. The *Q* factor of a resonator commonly indicates the rate of energy loss relative to the stored energy in the resonator. A resonator with higher *Q* factor possesses energy loss at lower rate, which increases the life time of photon inside resonant cavity. For highly sensitive chemical and biological sensing applications, it is desirable to have metasurface that can support high *Q* resonances.[122,123] At lower degree of asymmetry in the terahertz regime, Fano resonance tackles the problem of low *Q* factors by exciting extremely sharp asymmetric line shapes. However, at low asymmetry, the amplitude of excited Fano resonance is very small, which severely limits the application potential. To enhance the amplitude of Fano resonance the degree of asymmetry has to be increased which broadens the resonance and leads to sharp decline in the *Q* factor. Thus, toroidal coupling of Fano resonant mirrored metamolecules offers a solution to this problem by enhancing the *Q* factor and the FoM of the resonant response.

In this chapter, we experimentally demonstrate the excitation of terahertz toroidal resonances in mirrored Fano metamolecule pair. Toroidal coupling in asymmetric Fano resonator pair results in a strong excitation of a sharp resonance that possesses a *Q* factor, which is defined as the ratio of resonance frequency to the full width at half maximum (FWHM), significantly

higher than that of traditional Fano resonator array. Also, the measured toroidal resonance is of similar amplitude compared to the Fano resonance, which implies performance enhancement in terms of the figure of merit (FoM), which is product of *Q*-factor and the difference in peak to dip transmitted intensity (ΔI) at resonance, which quantifies the strength of toroidal coupling.[121] A magnetic dipole type excitation couples weakly to free space relative to the electric dipole type excitation. Putting these magnetic dipoles into head-to-tail arrangement results in net toroidal moment and further reduces the coupling of the metamaterial array to the free space, which leads to the enhancement of *Q* factor as a consequence of reduction in the radiative losses. We also observed the exponential decay in *Q* factor of both the Fano and the toroidal resonances with increase in the asymmetry of the resonators (see Sec. 4.3.4). However, the decay rate of the toroidal resonance *Q* factor occurs at half the rate of that of the Fano resonance which is indicative of the significantly smaller radiative loss in the toroidal metamaterials.

Therefore, near field coupling approach of tailoring radiative loss of Fano resonators through toroidal moment enhances the device performance which gives an efficient platform to study light matter interaction, as well as it enhances the mode volume of electromagnetic energy confined in the array of metasurface.

4.2 Toroidal coupling of fano resonators

For detailed investigation, we have considered Fano resonators which are square shaped terahertz asymmetric split ring resonator (TASR) with double split gaps. Plane wave radiation at normal incidence induces magnetic dipole type excitation in metallic resonator, which is similar to the inductive-capacitive (*LC*) resonance. In our experimental design, the array of equally spaced Fano resonators, having their magnetic moment vectors pointing in the same direction perpendicular to the metamaterial surface, are coupled through toroidal modes by

flipping over the neighboring resonators in alternate manner along one direction, such that their magnetic moment vector now points in the opposite direction. This alternate flipping over or mirroring of Fano resonators results in head to tail alignment of the magnetic moments of nearby resonators, which is responsible for the excitation of the toroidal resonance mode. The additional property of toroidal resonance over Fano resonance is to allow larger field confinement per unit volume, which arises due to tightly confined time varying magnetic field in circular region. Such strong field confinement opens prospects for their applications in lasing spaser, sensing and particularly micro-nanophotonics.[109,122] In the area of nonlinear optics for higher harmonic conversion efficiency of nonlinear devices there is requirement of strong field concentration in small cross-sectional area, which could be fulfilled by toroidal excitation.[124]

4.2.1 Fano and toroid metasurface fabrication

We have analyzed the EM response of an infinite 2-D metamaterial array having two different configuration of equally spaced terahertz asymmetric split ring resonator (TASR). The TASR consists of double split gap square shaped metallic strip, as shown in figure 4.2a. The outer dimension of individual resonator is 60μm × 60μm, arm width of the resonator is 6 μm and the split-gap size is 3μm. The resonator is made up of 200 nm thick aluminium (Al) metal on 500 μm thick *p*-type silicon substrate. The asymmetric nature of the TASR structure is due to positioning of both the splits, which are located 9 μm away from the center of the resonator. Excitation of TASR with incident electric field being parallel to the non-gap arms of TASR leads to broad symmetric line shape dipolar resonance and narrow asymmetric line shape resonances in the transmission spectra. The narrow resonance is also known as Fano resonance, which arises due to asymmetric nature of split ring resonator. In the later sections, we focus our discussion on sharp resonances. At the low frequency sharp resonance, the induced current density forms a closed loop along the strip, which is oscillating in nature with incident electric

field polarization. This closed loop oscillating current configuration acts like a magnetic dipole, which according to right hand rule may point in upward or downward direction perpendicular to the plane of the TASR metasurface. In this work, we arrange asymmetric resonators in two different configuration, which constitute non-identical metamaterial array. The first arrangement is named as “Fano” configuration, where metamaterial array contains equally spaced TASRs with periodicity of 75µm × 75µm. Another metamaterial array comprises of second arrangement of mirrored TASRs which is named as “Toroid” configuration having periodicity of 150µm × 75µm. This is formed by flipping over the neighbouring TASRs of “Fano” configuration alternatively along one direction (figure 4.2b).

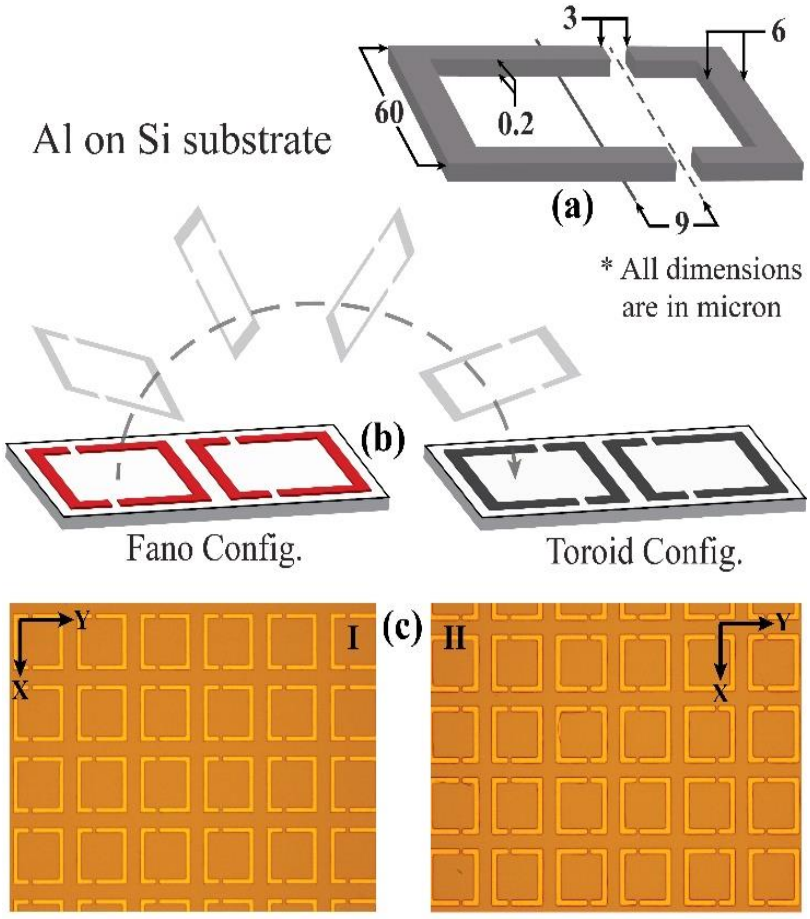

Figure 4.2: (a) Schematic of asymmetric resonator (all dimensions are in microns) (b) Artistic impression of the two different arrangements of resonators, where difference is explained via flipping one of the resonators by 180^0 (c) Microscopic image of fabricated samples.

We probe the impact of the toroidal coupling between equally spaced asymmetric resonators. Different periodicities just indicate the two different configurations named as “Fano” and “Toroid”, which overall gives an idea of arrangement of TASR in the metamaterial array. In both configurations all TASRs are equally spaced. The change in the effective lattice constant does not affect the comparison between the two resonance modes since the diffractive lattice modes do not interfere at the Fano and toroidal resonance frequencies.[125] The design consists array of only two neighbouring TASRs, as shown in figure 4.2b, where one arrangement could be changed to another by simply flipping the first TASR by 180^0. Figure 4.2c (I and II) shows the microscopic image of two different arrangements of TASRs fabricated experimentally through the photolithography process. If we assume the fabricated samples to be placed on XY plane as shown in the figure, then the microscopic image for the second arrangement clearly indicates alternate arrangement of TASRs along the Y-direction as compared to the first one.

4.2.2 Induced magnetic dipole for toroidal coupling

For both the samples to be on the XY plane as shown in figure 4.3a, 4.3b, the incident EM field excites the samples at normal incidence (along Z-direction), having its electric field ($\vec{\boldsymbol{E}}$) component perpendicular to the gap arm (along X-direction). Electromagnetic excitation of TASRs arranged in “Fano” configuration induces similar current configuration along metallic strip in neighbouring resonators (anticlockwise sense in figure 4.3a), which corresponds to the Fano resonance response. Closed loop electric current for each TASR gives rise to an array of magnetic dipoles ($\overrightarrow{\boldsymbol{m}}$) pointing in the same direction (along Z-direction) perpendicular to the metasurface array. On the other hand, “Toroid” configuration is formed by flipping over of first TASR, where the loop currents and magnetic dipoles ($\overrightarrow{\boldsymbol{m}}$) are opposite in nature for neighbouring TASRs, as depicted in figure 4.3b.

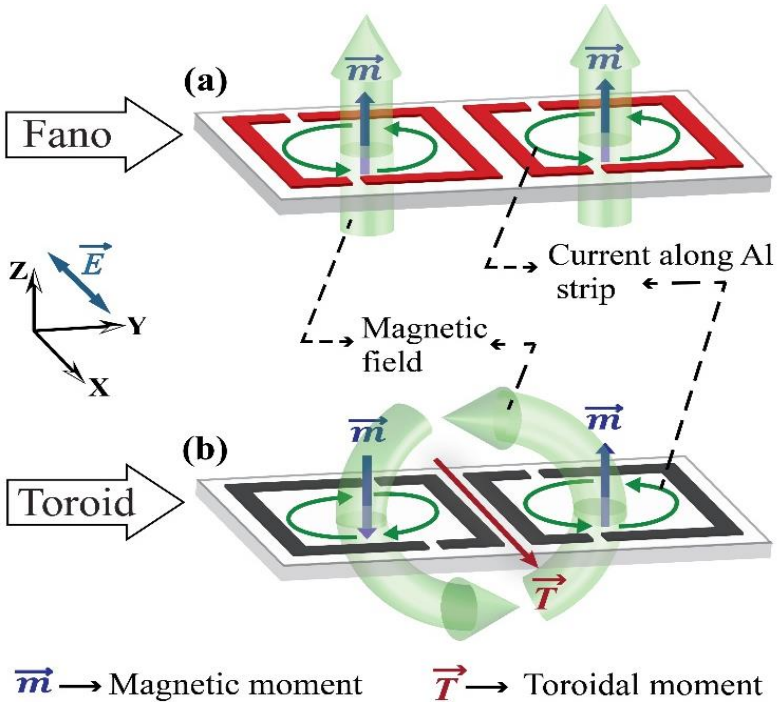

Figure 4.3: Artistic image of TASRs arranged in different configurations with induced surface currents and magnetic moments.

This head to tail alignment of magnetic dipole ($\vec{m}$) leads to coupling between the nearby TASRs via circulating magnetic fields. This concentrated time varying magnetic field in small circular region generates toridal dipolar ($\vec{T}$) resonance excitation, which according to right hand rule points in the X-direction. The moment of toroidal dipole ($\vec{T}$) signifies the strength of coupling between alternately flipped TASRs.

4.3 Tuning resonant features via nearest neighbour coupling

4.3.1 Numerical modelling and experimental analysis

To investigate the nature of sharp resonances, numerical simulations were carried out for both arrangements in frequency domain with periodic boundary condition by using commercially available software CST Microwave Studio, and Comsol Multiphysics. Toroidal component at

different frequency values have been calculated via multipole analysis.[26] In simulated model, the material parameters of Aluminium metal was described by the Drude model, where angular frequency dependent permittivity is given by $\varepsilon(\omega) = \varepsilon_{\infty} - \left[\omega_p^2 / \omega(\omega + i\Gamma) \right]$, with the plasma frequency ω_p (22.43×10^{15} rad/sec for Al) and damping rate Γ (124.34×10^{12} rad/sec).[105] Electromagnetic radiation induces circular loop currents in TASR, which is analogous to the *LC* resonance. Circulating currents give rise to a magnetic dipole which points according to the orientation of TASR. Flipping of SRR also results flipping of induced magnetic dipole. Figure 4.4a and 4.4b depicts simulated and experimental transmittance over extended range of frequency, which includes both broad symmetric line shape dipolar resonance and narrow

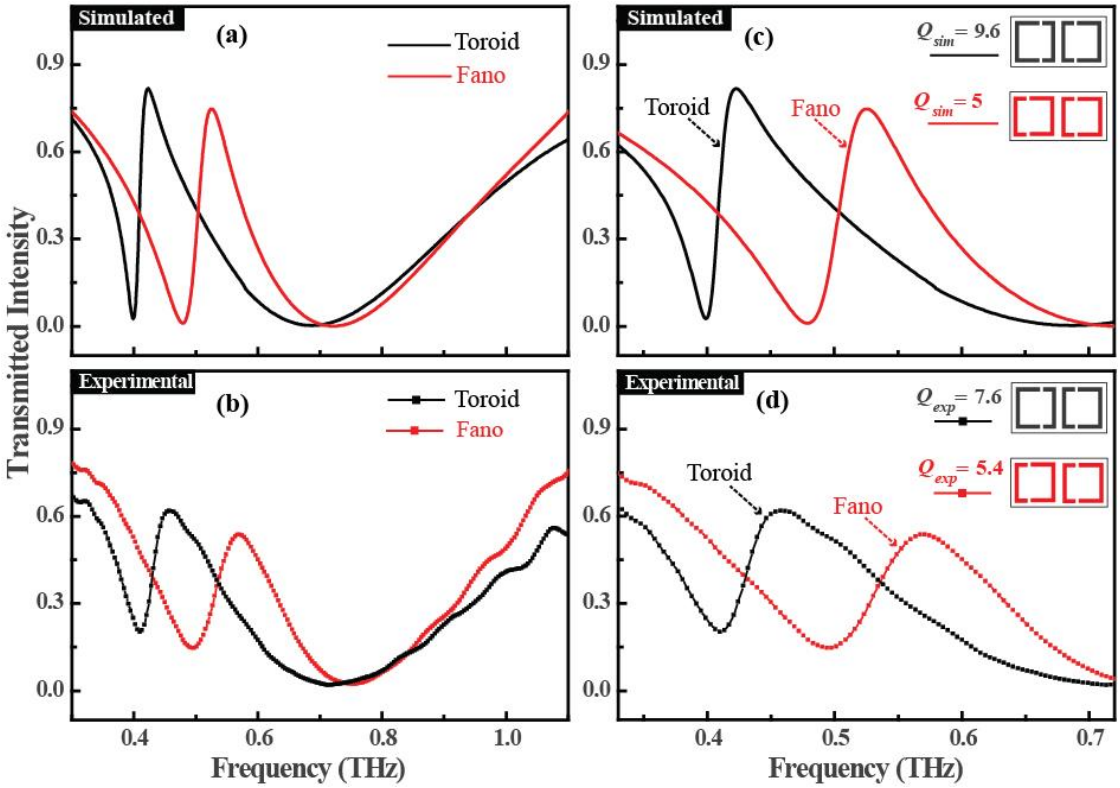

Figure 4.4: Simulated (a, c) and experimental (b, d) transmitted intensity spectra for toroid and Fano arrangements of TASRs, when E field is polarized perpendicular to the gap. The quality factors for the simulated (c), and experimental (d) asymmetric line shape narrow resonances are given in the inset.

asymmetric line shape Fano/toroidal resonance for both arrangements. Figure 4.4c and 4.4d shows the simulated and experimental transmitted intensity spectra, and *Q*-factor only for asymmetric line shape resonances excited in both configurations. The sharp Fano and toroidal resonances appear close to 0.48 THz and 0.4 THz, respectively. The linewidth of toroidal resonance is smaller as compared to the Fano resonance. The quality factor, for toroidal resonance (Q = 9.7) is almost twice that of Fano resonance (Q=5) (as shown in figure 4.4a), which indicates the effectiveness of coupling through the toroidal moment. Due to higher *Q* factor and relatively same amplitude of the resonances, toroidal excitation has higher figure of merit (FoM) value as compared to the Fano excitation. Experimentally, conventional terahertz time-domain spectroscopy (THz-TDS) setup has been used to measure the transmission spectra in far-infrared region.

4.3.2 Near-field coupling through multipole decomposition

We have also examined the near field coupling between resonators for both arrangements. Red shift of toroidal resonance (figure 4.4) signifies the enhanced coupling between the TASRs which alters the resonance frequency of the metamaterial array containing alternate arrangement of resonators. To establish the fact that the enhanced coupling is due to toroidal moment, we carried out multipole analysis to extract the toroidal component for both arrangements (see section 1.3 for more details).[72] Figure 4.5 shows transmitted intensity (inset plot), and toroidal component computed through multipole analysis. The behaviour of computed transmission intensity is nearly similar to that of the experimental results, which validates the modelling of the metamaterial array via multipole analysis. At respective resonances extremely sharp peak of T_x component for "Toroid" configuration clearly indicates the enhanced coupling between TASRs due to the toroidal moment, which is responsible for the enhanced *Q* factor response. There is no such signature of near field toroidal coupling in

the Fano arrangement. Near field coupling also enhances electromagnetic field concentration in the unit cell of metamaterial array, which has variety of applications as discussed earlier.

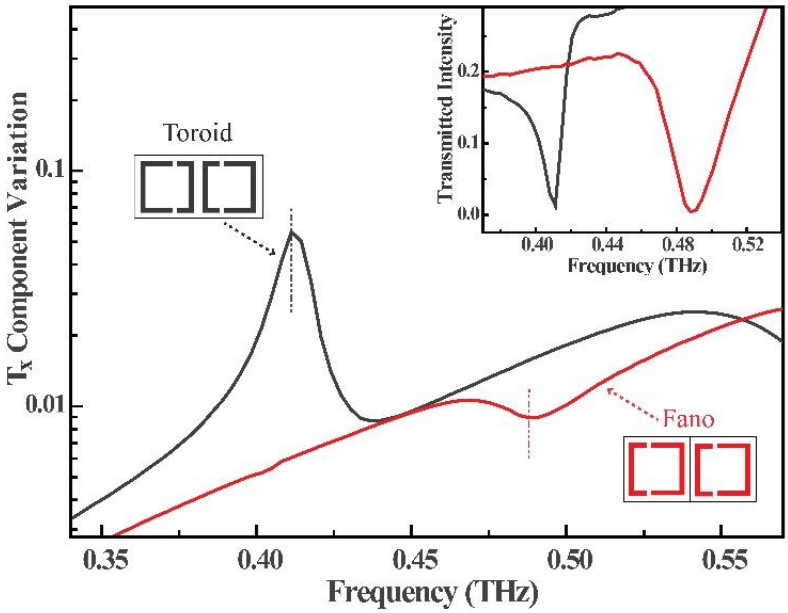

Figure 4.5: Transmitted intensity (inset plot) and toroidal dipole component computed from multipole analysis for two different configurations of TASRs.

4.3.3 Simulated current and electric field density

To further substantiate the effect of coupling we have simulated the surface currents along metallic strips and electric field intensity confined in capacitive splits for both arrangements, as shown in figure 4.6. Strong antiparallel current distribution in neighbouring resonators pronounce relatively stronger coupling for “Toroid” configuration (figure 4.6a, 4.6b). Also, antiparallel current distribution indicates that the coupling is through the toroidal moment. Stronger surface currents indicate high amount of magnetic energy confined in the metasurface array which is due to the additional mutual inductance in the toroidal configuration. This also leads to the red-shift of the toroidal resonance as compared to that of the Fano resonance. Similarly, figure 4.6c and 4.6d depicts stored electrical energy in capacitive splits, which is also relatively stronger for the “Toroid” configuration.

4.3.4 *Q*-factor and figure of merit (FoM) analysis

Further, to compare the behaviour of toroidal and Fano resonance, we analysed the response of both these confined modes by varying the asymmetry of the TASR (position of splits gaps)

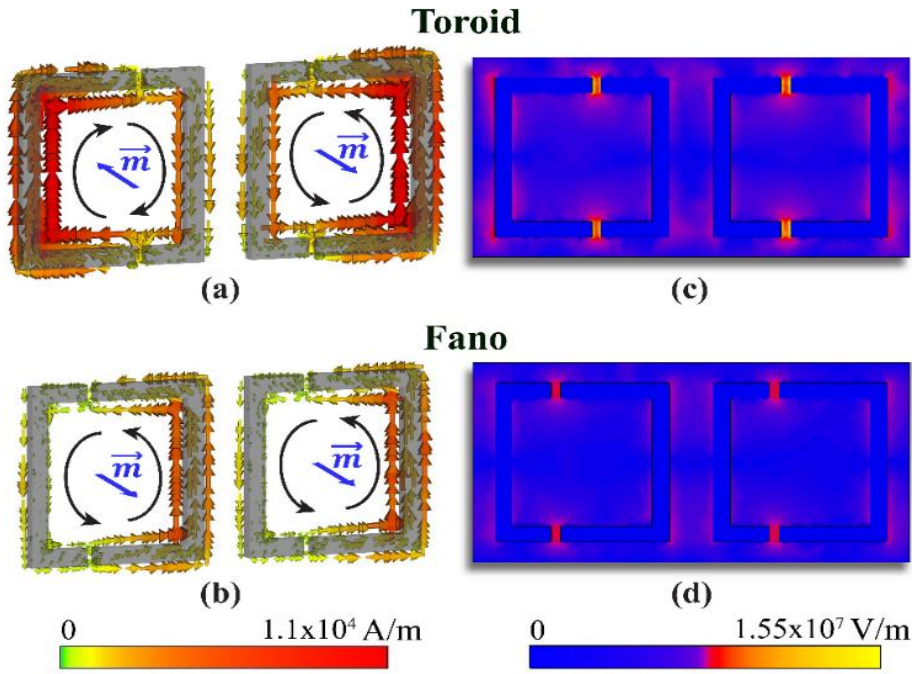

Figure 4.6: Simulated surface currents (a, b) and electric field intensity (c, d) confined in capacitive gaps of metallic resonator arranged in "Fano" and "Toroid" configurations.

indicated by *d*, for the two non-identical arrangements. Figure 4.7 depicts a comparison between the salient features, such as resonance line-width, *Q*-factor, and FoM, which are essential parameters to consider for the practical implementation of metadevices. Shifting of split gaps in TASR can also be addressed in terms of asymmetric parameter (α), defined as the ratio of differential length $(l_1 - l_2)$ of strips to the combined length $(l_1 + l_2)$ of strips of TASR. In transmitted intensity spectra (figure 4.7a, 4.7b), at different asymmetries the line-width of toroidal resonance (in "Toroid" configuration) is smaller than that of the Fano resonance. This line narrowing results in higher *Q*-factor for toroidal resonances as compared to Fano resonances (figure 4.7c) at different asymmetries (*d*) of TASR. The *Q*-factor values of toroidal

resonances are significantly higher compared to Fano resonances. With increasing asymmetry *Q*-factor decreases exponentially for both the resonances. An exponential fit has been performed using the below equation between *Q*-factor and the asymmetry *d* of TASR, where, theoretically, *A* denotes the peak *Q* factor at extremely low asymmetry and *C* denotes the saturated *Q*-factor at very high asymmetry respectively, and *B* represents the decay constant.

$$Q_{factor} = A\exp(-B.d) + C \qquad \text{... ... ... 4.1}$$

With increasing asymmetry decay constant for the *Q*-factor of Fano resonance (B=0.77) is nearly twice as that of toroidal resonance (B=0.37). Also the variation of FoM with increasing asymmetry in figure 4.7d indicates considerably higher values for toroidal resonances. Though the *Q*-factors are nearly identical for both configurations at the low asymmetry (*d*) of 1 µm, the FoM value for the toroidal resonance is nearly three times the Fano resonance. The peak FoM (13.14) of toroidal resonance (at *d*=4 µm, *Q*=32) is more than twice the peak FoM (4.98) value of the Fano resonance (at *d*=3 µm, *Q*=22). Even at larger asymmetries, where α = 17.1% at highlighted asymmetry of *d*=10 µm, FoM of toroidal resonance remains higher than the Fano resonance.

In both cases *Q* factor decays exponentially for asymmetric line shape response, which arises as a result of destructive interference of the fields scattered by the two metallic components of each metamolecule, i.e. at resonance the current in the one strips will be directed ‘up’ at the same time as the current in the another strip will be directed ‘down’. On an abstract level, the bright mode here is linked with electric dipole that couples strongly to free-space radiation (although coupling at resonance is reduced), whilst the dark mode is linked with magnetic dipole, which still couples to free-space radiation, but the coupling is significantly weaker than electric dipole. The position of the gaps (different values of *d*) control; how the symmetric ‘electric dipole’ mode couples to asymmetric ‘magnetic dipole’. For smaller degree of

asymmetry this coupling is strong enough to make the TASR current distribution sub-radiant, so *Q* factor of resonance is high at lower degree of asymmetry. As the degree of asymmetry increases the coupling between symmetric and asymmetric mode decreases which makes the

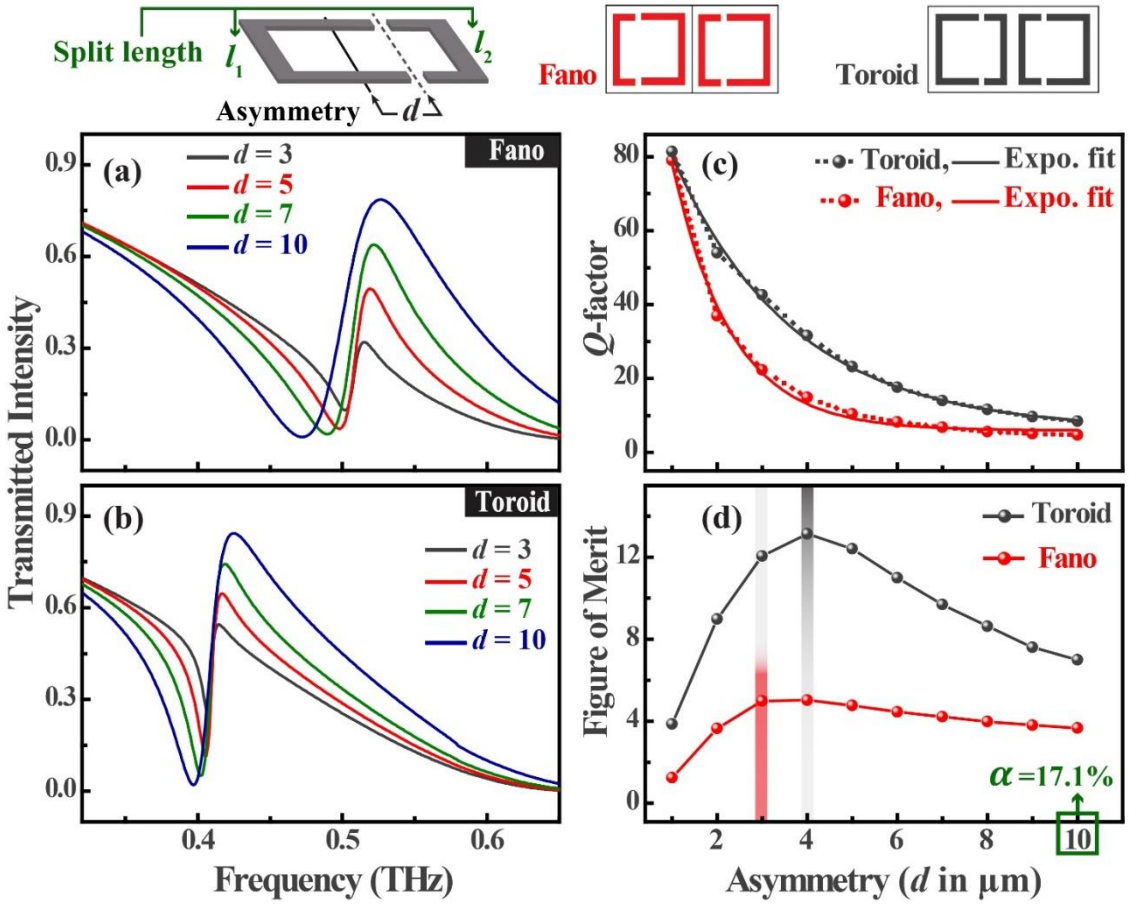

Figure 4.7: Simulated transmitted intensity (a, b), Q-factor (c), and figure of merit (d) for TASRs arranged in "Fano" and "Toroid" configuration, where asymmetry (position of split gaps) in TASR is indicated by d. Degree of asymmetry $\alpha = \left[\left(l_1 - l_2\right)/\left(l_1 + l_2\right)\right] \times 100$, where l_1 and l_2 are split lengths of TASR.

current distribution in the TASR radiative, which causes the decline of the *Q* factor. Therefore, apart from symmetry breaking in TASR, the degree of asymmetry also plays a key role in the excitation of high *Q* resonances. So, higher asymmetry leads to the lowering of the *Q* factor of resonance, as depicted by figure 4.7c.

4.4 Conclusion

In summary, we have clearly demonstrated that a mirrored arrangement of Fano resonators leads to sharp toroidal resonances with significant enhancement in quality factors. A clear difference between Fano and the toroidal resonances has been discussed in planar terahertz metasurfaces. We have experimentally demonstrated that coupling Fano resonators through toroidal moment plays an important role in narrowing the line width of asymmetric line shaped resonances, which will enhance the performance in terms of quality factor of metamaterial based photonic devices. In other words, for the same degree of asymmetry in TASRs, toroidal resonances offer another route to excite low loss, high-*Q*, higher FoM value resonances. Toroidal resonances are relatively superior non-radiative resonances as compared to the Fano resonances that could be exploited for metadevice applications in ultrasensitive sensing, lasing spasers, modulators, narrowband filters and nonlinear optics.

Chapter 5

Active Tuning and Switching of Toroidal Resonances

Toroidal dipole is a localized electromagnetic excitation that plays an important role in determining the fundamental properties of matter due to its unique potential to excite nearly non-radiating charge-current configuration. Toroidal dipoles were recently discovered in metamaterial systems where it has been shown that these dipoles manifest as poloidal currents on the surface of a torus and are distinctly different from the traditional electric and magnetic dipoles. In this chapter, an active switching scheme has been demonstrated in which the toroidal dipole could be dynamically switched to the fundamental electric dipole or magnetic dipole, through selective inclusion of active elements in a hybrid metamolecule design.

5.1 Introduction

Subwavelength metallic resonators provides an innovative approach to manipulate the electromagnetic response of macroscopic media.[110,126-128] The electromagnetic response originating from the individual subwavelength photonics resonators is due to induced charge/current distribution, which are further categorized in terms of electric, magnetic and toroidal multipoles.[101,129] Here, the nature of individual multipole signifies the extent of

coupling to free space, which plays an important role in tailoring the losses by radiative means.[56,57] In the burgeoning field of metamaterials, a well-established framework has been developed to play around the loss channels influenced by the electric and magnetic responses,[46,107] but recently there has been intense interest in toroidal electrodynamics for loss engineering.[70] Toroidal dipole is visualized as the currents flowing on the surface of torus (poloidal currents) along its meridians, where array of magnetic dipoles originating from poloidal currents are arranged in head-to-tail configuration along a torus. In metamaterials, several works discussed novel schemes that mimic the 3D torus configuration for the electromagnetic excitation of the toroidal dipole.[73,130] However, the electromagnetic response of artificial media with toroidal topology is also accompanied by electric and magnetic multipoles. The flexibility in tailoring the moment of toroidal dipole allows to explore one of the exotic feature in terms of non-radiating charge current configuration, commonly known as anapole, due to destructive interference of electric and toroidal dipole.[120,131] Recently, an idea of anapole-based nanolasers have been proposed, where stimulated emission amplifies an anapole mode in dielectric resonator.[83] Though, it is very difficult to achieve perfect anapole conditions, yet researches are more focused towards the toroidal dipole mode because it offers weak electromagnetic scattering compared to the electric and magnetic dipoles, and could lower the radiative loss due to electric dipole, which is dominant in almost all kinds of electromagnetically excited metasurfaces. In three-dimensional artificial media, the dynamic toroidal moment were exploited to observe well known electromagnetic phenomena such as resonant transparency[84] and circular dichroism.[132] Even in 2D metasurfaces, introduction of toroidal coupling enhances device performance in terms of quality factor (Q), which is defined as the ratio of resonance frequency to the full width at half maximum, and figure of merit (FoM $=Q \times \Delta I$, product of the Q-factor and the difference in peak to dip transmitted intensity (ΔI)) at electromagnetic resonance.[121]

5.2 Switching between fundamental multipoles

Line-width of an electromagnetic resonance depends on the nature and strength of the scattering phenomenon. Depending upon the excitation requirements, the electromagnetic response of the metamaterial array can be of electric, magnetic or toroidal type, which is achieved by passively modifying the unit cell configuration. For instance, electric dipole that scatters strongly due to their broad line-width, are used as antenna or local sensors to probe the near field.[124] Similarly, magnetic dipole, which has comparatively narrower line-width, is used as dielectric/strain sensor and most importantly in the excitation of the toroidal dipole.[133] Switching electromagnetic response between these characteristic dipoles will necessarily provide a promising route towards building new optical devices. Moreover, active tuning of toroidal excitation will definitely add other key functionalities to metamaterial based devices, which are important for potential applications.

5.3 Active modulation and switching scheme

We demonstrated an active metamaterial switch that could dynamically make transition from nearly non-radiative *toroidal configuration to electric or magnetic dipole excitations*. In this active scheme, an ultrathin silicon layer beneath the capacitive split gap of a metallic resonator in the unit cell of metamaterial array acts as a dynamic material that precisely controls the optical properties of the hybrid metamaterial with the help of external stimulus in the form of near infrared femtosecond pulses. The unit cell design consists of a planar asymmetric resonator pair arranged in the mirrored configuration, which supports a toroidal resonance excitation. By judiciously suppressing electromagnetic resonance of one or both resonators in mirrored configuration, one can dynamically switch from toroidal resonance to a magnetic dipole or an electric dipole resonance. Our result also manifests smooth transition and complete

modulation of toroidal resonance at very low pump fluence. For toroidal to electric dipole transition, the experimentally achieved maximum value of peak to peak amplitude modulation depth is 73%, which is defined as $(T_{off} - T_{on})/T_{off} \times 100$ for the entire spectral range, where T_{off} and T_{on}, respectively, stands for the transmission amplitudes during 'off' and 'on' stage of optical pump. We also obtained a point (in frequency) of nearly constant intensity transmission during the course of active tuning across a broad spectral range.

5.3.1 Design and fabrication

The active control mechanism of toroidal resonances is enabled by a hybrid metasurface containing silicon pads at the split gaps of terahertz split ring resonator structure. Figure 5.1a shows the microscopic image of the fabricated sample along XY plane, where the zoomed unit cell reveals the mirrored configuration of terahertz asymmetric split ring resonators (TASRs). The outer dimension of individual resonator is 60 µm × 60 µm, with arm width of 6 µm and the split-gap size equal to 3 µm. The asymmetric nature of the TASR structure is due to positioning of both the split gaps, which are located 10 µm away from the center of the resonator. The unit cell has periodicity of 150 µm × 75 µm in which mirrored TASRs are separated by a distance of 15 µm. The enlarged image of unit cell displays rectangular patches of silicon beneath the split gaps of the mirrored resonator, which upon photoexcitation generate free carriers that enables the active control of the toroidal response. The metamaterial samples were fabricated using two step lithography cycle followed by reactive ion etching (RIE). The metallic resonators are fabricated by thermally depositing 200 nm thick aluminium (Al) on silicon on sapphire (SoS) substrate composed of 600 nm thick silicon epilayer and 460 µm thick sapphire. RIE results in removal of undesired silicon from the structure, such that silicon remains beneath the metallic strip and at the split gaps of TASRs.

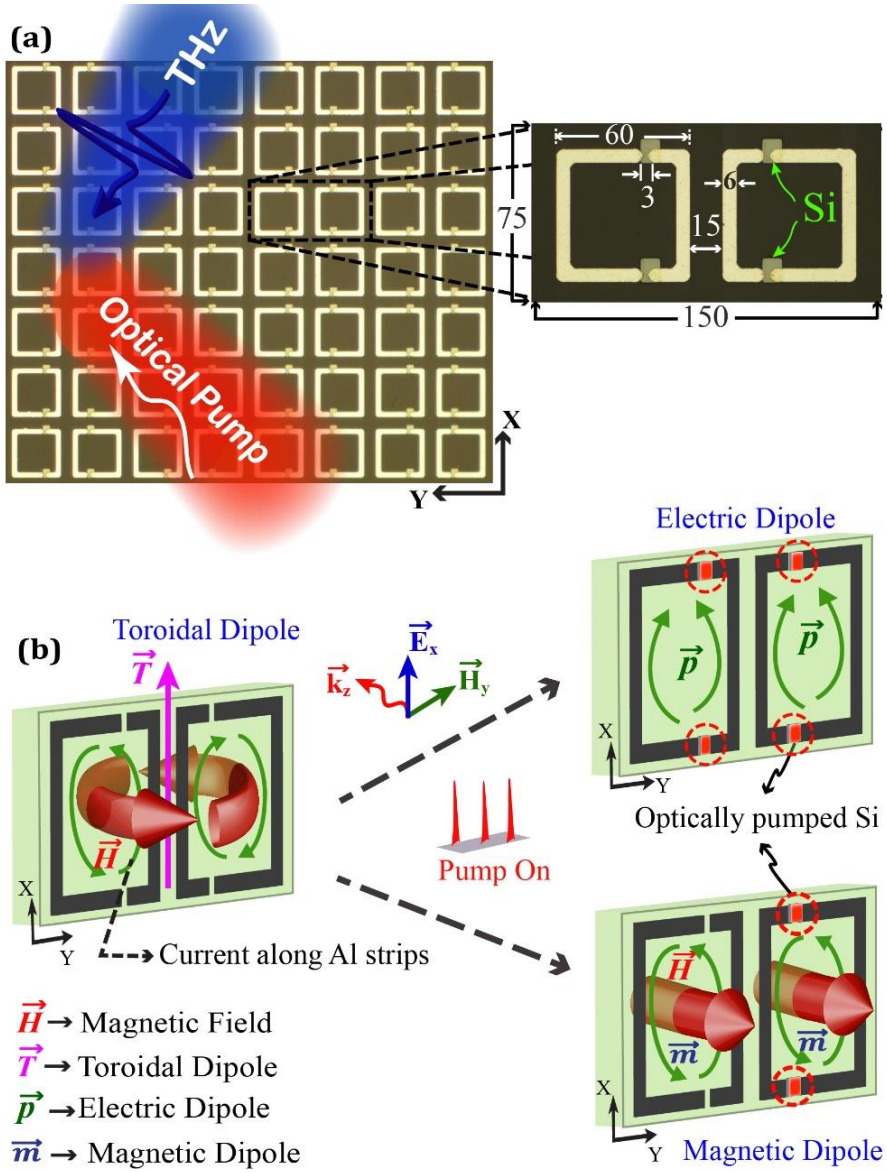

Figure 5.1: (a) Microscopic image of fabricated metamaterial sample, along the XY plane, illuminated with pump beam in presence of THz pulse, where zoomed image shows unit cell dimensions (in microns) of Si implanted TASRs arranged in mirrored configuration, (b) Switching in the response of unit cell from toroidal dipole to electric or magnetic dipole in presence of optical pump.

5.3.2 Mirrored TASRs for switching

In the absence of pump beam, THz excitation of *mirrored* TASRs with incident electric field polarization along X-direction $(\vec{E}_x)$(as shown in figure 5.1b), results in excitation of both

symmetric dipole mode (bright mode) at higher frequency and anti-symmetric toroidal dipole resonance mode (the dark mode) at lower frequency. In the state of toroidal dipole resonance, induced circulating oscillatory currents in mirrored configuration are opposite in nature (see image labelled as 'Toroidal Dipole' in figure 5.1b). Such a current distribution leads to tightly confined loops of oscillating magnetic field $(\vec{H})$ that curl around the fictitious arrow, which is a characteristic feature of the toroidal dipole vector $(\vec{T})$ in 3D space. As the pump beam illuminates the metasurface, photo excitation of silicon pads increase its conductivity that gradually alters the nature and strength of the toroidal resonances. At higher pump fluences, depending on the placement of silicon pads in split gaps of one or both TASRs, the excited current distribution, as shown by figure 5.1b, either switches to anti-symmetric magnetic dipole (dark mode) or purely symmetric electric dipole (bright mode) configuration.

5.4 Active modulation of toroidal resonance

5.4.1 Experimental results

Optical-pump and THz-probe (OPTP) spectroscopy has been used for the optical characterization of hybrid silicon TASR samples, wherein pulsed optical beam of 800 nm wavelength is incident for photoexcitation of metamaterial sample and the photo-response of excited metasurface is probed by shining THz pulse at normal incidence with a beam diameter of 3 mm. Amplified pulsed laser of pulse width 120 fs and repetition rate of 1 kHz respectively, has been used as the pump beam. Pump beam with beam diameter of 10 mm has been employed to ensure uniform photoexcitation excitation in the vicinity of THz-probe beam interaction with metasurface. With respect to every pump pulse, THz pulse is delayed by 12 picoseconds to capture the excitation phenomenon at a particular instant, when the free carrier density in photo-excited silicon layer is maximum.

Photo-active mediated switching of toroidal resonance has been realized here by illuminating fabricated sample at different pump fluence, which is defined as radiant energy received per unit surface area (μJ/cm^2). Figure 5.2a shows the experimental results depicting transmitted intensity response with increasing fluence of pump beam. In the absence of pump illumination, with incident THz beam polarized along the X-direction (E_x), the anti-symmetric toroidal dipole resonance mode first appears at frequency of 0.453 THz and symmetric electric dipole mode appears at frequency 0.82 THz. Since, the chosen scheme provides the freedom to tailor the anti-symmetric mode (the dark mode), we focused our discussion on the lower frequency toroidal resonance. With gradual increase in the pump power, the amplitude of toroidal resonance decreases, while no significant change is recorded in the broad symmetric mode. At increased pump powers, silicon which is primarily a semiconductor starts behaving like a quasi-metal due to large photocarrier generation. This change in behaviour of silicon conductivity shorts the capacitive split-gaps of TASR pair in the unit cell, which leads to complete disappearance of the toroidal resonance feature of the metasurface for higher pump powers beyond 50 mW (pump fluence of 63.6 μJ/cm^2). The only resonance that survives in the transmittance spectra is that of an electric dipole. For the estimation of normalized transmittance at different values of pump powers, measurements have been performed by alternatively scanning THz pulse through the fabricated photo-excited metamaterial sample and bare sapphire substrate which acts as the reference. The intriguing feature that we observed at different pump powers, is the point of near constant transmission at the frequency of 0.486 THz as shown by the dotted line in figure 5.2a. The signature of constant transmission point arises due to near perfect destructive interference between the sharp dark mode (toroidal) and bright mode (dipole) close to the frequency where the toroidal resonance originates. In the present metamaterial structure, a strong anti-symmetric dark toroidal resonance mode leads to

the observation of the near constant transmission. Such observations are rare due to typical weak excitations of dark mode resonances in most metamaterial and plasmonic systems.

5.4.2 Numerical simulation

To study the photo-active tuning of the toroidal resonances, we employed numerical simulation using a commercially available CST Microwave Studio frequency domain solver, based on finite integration method. During numerical simulations TASRs have been modelled as lossy aluminium metal with DC conductivity (σ_{DC}) of $3.56\times10^{7}\,\mathrm{S/m}$, sapphire ($\varepsilon_r = 11.7$) as a

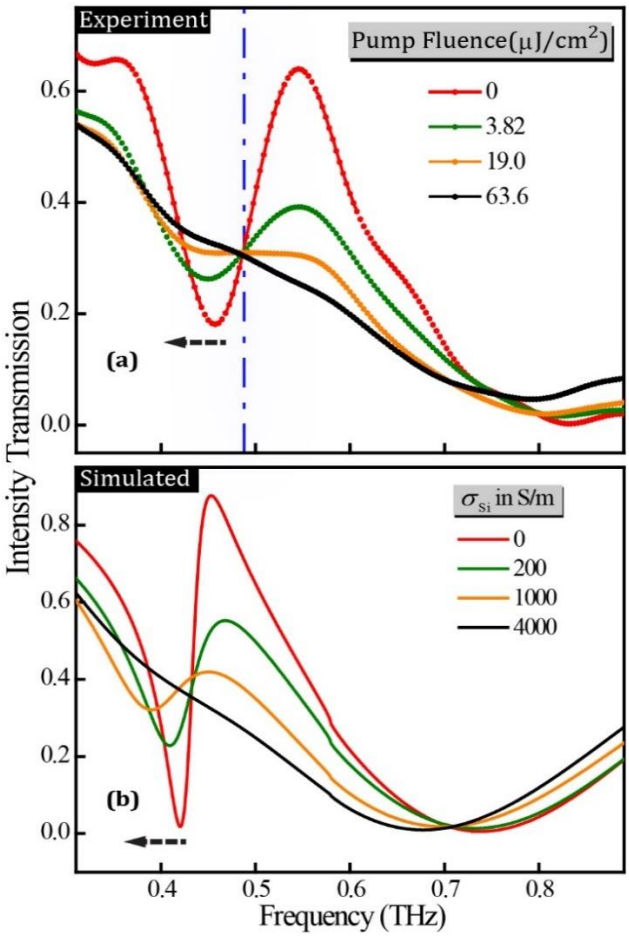

Figure 5.2: Transmitted intensity spectra of toroidal metasurface at different pump fluences for experimental (a) and at the corresponding conductivities for simulated (b) results, when electric field is polarized perpendicular to the gap arm of TASR. The dotted line shows the point of nearly constant transmission. Dotted arrow shows minute red shift in frequency of toroidal resonance.

transparent substrate, and silicon ($\varepsilon_r = 11.9$) layer sandwiched between aluminum and sapphire. In simulations, the conductivity of Si has been modelled using experimentally extracted photoconductivity of the unpatterned 600 nm silicon epitaxial layer on sapphire (SOS) for the corresponding fluence of the excitation pulse. Figure 5.2b shows the simulated normalized transmittance spectra of silicon implanted TASRs for the increasing conductivity (σ_{Si}) of silicon layer. $\sigma_{Si} = 0$ curve corresponds to a situation when there is no illumination of metasurface by the pump beam. As σ_{Si} increases, the amplitude of toroidal resonance decreases and the resonance almost disappears at $\sigma_{Si} = 4000$ S/m. Also, the minute red shift (shown by dotted arrow in figure 5.2a, 5.2b) in the frequency of toroidal resonance, because of optical pumping, in experimental as well as in simulated results can be explained by an analogous inductive-capacitive (LC) circuit model.

5.4.3 Model explaining red shift of toroidal resonance

At the instant of toroidal resonance, nature of current distribution in individual resonator of mirrored configuration is analogous to series *LC* resonator circuit, where splits gaps act as capacitor while metallic strips act as inductor (as shown in figure 5.3). Silicon pads beneath the splits gaps act as shunt resistance (R_{Si}), which dissipates energy stored in capacitive split gaps during optical excitation (as conductivity of silicon increases, R_{Si} decreases). Due to leakage of charge through shunt resistance capacitor fails to store electromagnetic energy. The effective value of circuit impedance (Z) and resonance frequency (f_{reso}) are modified by the shunt resistance. For simplicity L and C have been fixed to some default values as shown in figure 5.3.

Resonance frequency versus R_{Si} plot shows that frequency of resonance red shifts with decreases in the value of shunt resistance. The shift can be understood by *LC* circuit model

where optical pumping changes the effective resistance across the capacitive gaps. At low pump fluence (high effective resistance) the red shifts are very small. On the other hand, high pump fluences results in low effective resistance across the capacitive gaps, which weakens the amplitude of resonance significantly, so any change in frequency shift is not visible.

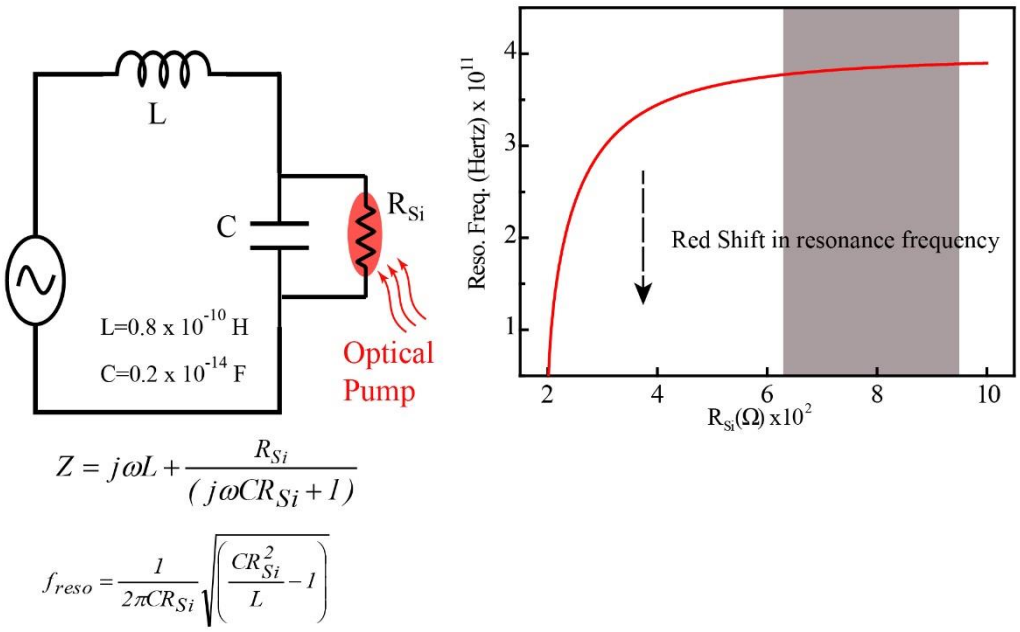

Figure 5.3: Model depicting red shift in the resonance frequency of LC resonator circuit due to decrease in the resistance across capacitor by optical pump.

5.4.4 Pump mediated tuning of toroidal coupling

Furthermore, we carried out multipole analysis (see section 1.3) to investigate the role of near field toroidal coupling for different transmittance curves, and to establish the fact that modulation of the anti-symmetric toroidal mode (at lower frequency) can be achieved by tailoring the conductivity of split-gaps of the TASRs in the unit cell.[72] Here, it is important to mention that our analysis is limited to toroidal coupling between the TASR pair that forms the unit cell. Figure 5.4 shows transmitted intensity (inset plot) and corresponding toroidal component ($\boldsymbol{T_x}$) computed through multipole analysis. Transmitted intensity (inset plot)

computed through multipole analysis shows similar trend as experiments, which validates the modelling of the metamaterial array via multipole analysis. The peak of toroidal moment for $\sigma_{Si} = 0$ corresponds to the strength of coupling between the two mirrored resonators in the absence of pump pulse. With an increase in the intensity of the photoexcitation, σ_{Si} increases, which leads to the reduction in the strength of toroidal coupling from $\sigma_{Si} = 100$ to 4000 S/m. This deterioration in toroidal coupling results in the broadening of resonance line-width as well as decrease in the amplitude of resonance (as shown in figure 5.2 and in inset of figure 5.4).

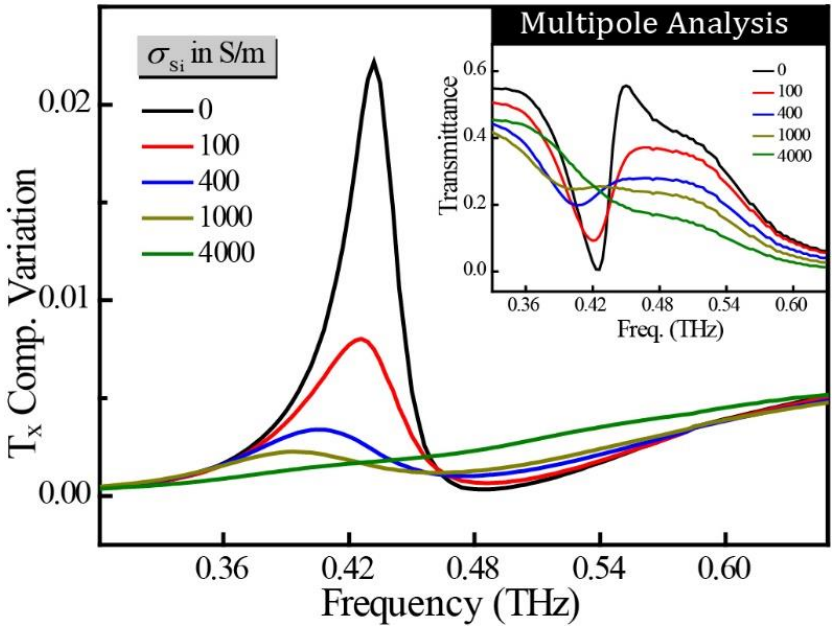

Figure 5.4: Transmitted intensity (inset plot) and X component of toroidal dipole moment computed through multipole analysis for the increasing conductivity of Si beneath split gaps of TASR.

5.4.5 *Q* factor / FoM dependence on silicon conductivity

Optical pumping of silicon (Si) implanted metasurface with 800 nm wavelength increases the conductivity of Si, which depends on the amount of fluence incident on metasurface. The effect of optical pumping on the toroidal resonance can be understood in terms of *Q* factor, (defined as the ratio of resonance frequency to the full width at half maximum) and figure of merit (FoM)

values estimated from transmitted intensity plot. We define the figure of merit (FoM) as product of the *Q*-factor and the difference in peak to dip transmitted intensity (ΔI) (FoM = $Q \times \Delta I$) at resonance. Figure 5.5 shows the variation of *Q*-factor/ FoM values with increasing conductivity of Si. There is slight variation in *Q* values but FoM decays exponentially due to decrease in amplitude of resonance. This indicates that, at higher pump fluences mirrored resonator cavity is weakly excited at resonance (damping is large) and it fails to store electromagnetic energy.

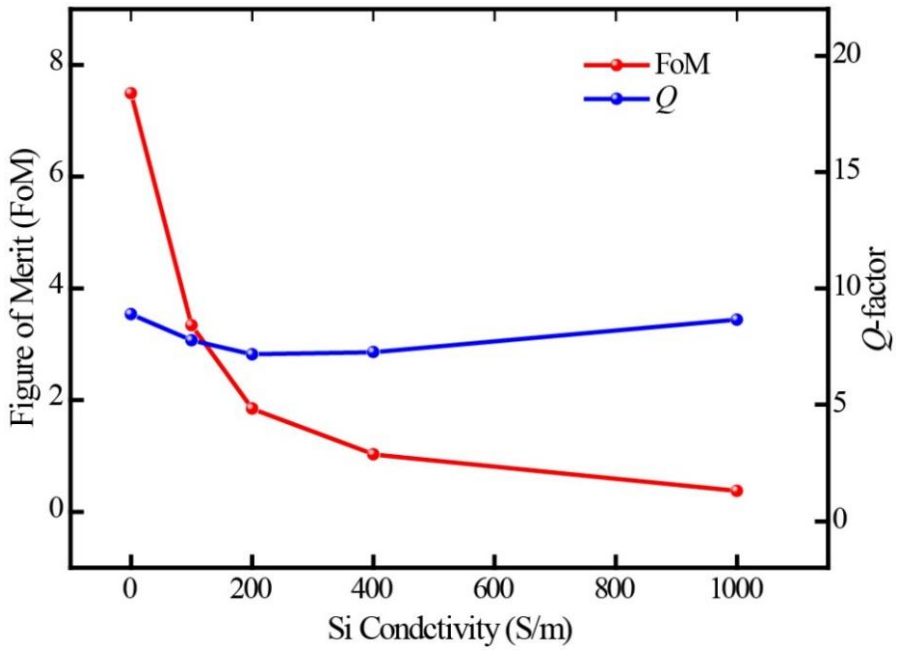

Figure 5.5: Simulated results depicting Q-factor/FoM dependence with increasing conductivity of Si in split gaps of mirrored TASRs.

Besides active tuning, we obtained a smooth transition of toroidal resonance trough and transmission peak, between the on-off positions of pump fluences. In terms of modulation depth, figure 5.6 depicts percentage variation in experimentally measured transmission amplitude at different values of pump fluences for the entire range of frequency spectrum. The change in amplitude is significantly large at the resonant transmission peak (0.545 THz) compared to that of resonance dip at 0.453 THz. Experimentally achieved peak to peak amplitude modulation depth between toroidal resonance trough (region shaded in blue) and the

associated transmission peak (region shaded in grey) is about 73%. Pump powers involved in the current scheme is reasonably low compared to the schemes reported previously in the literature for switching electromagnetic resonances in the THz regime.

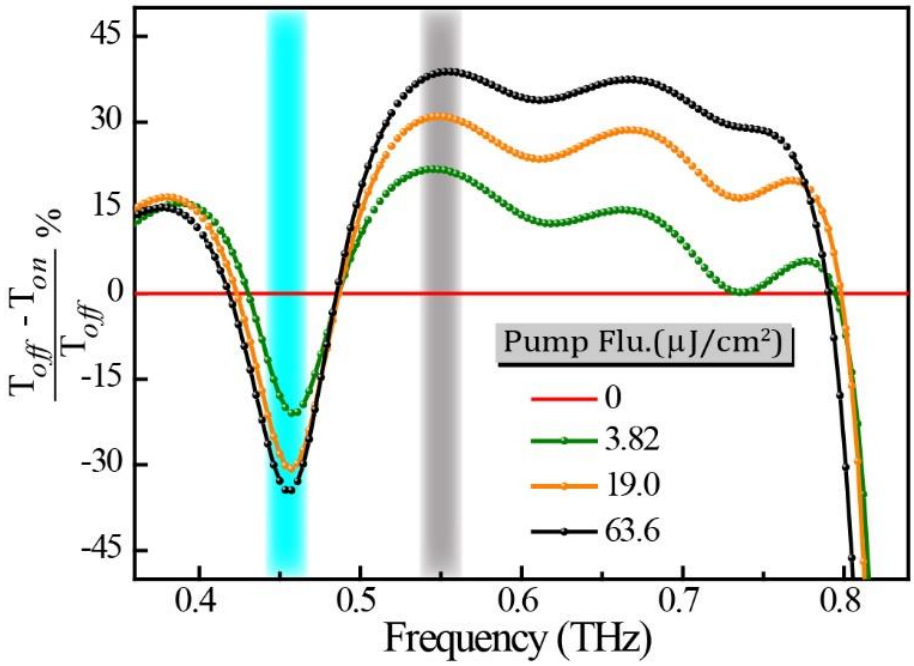

Figure 5.6: Percentage modulation of experimental transmission amplitude versus frequency plot at different value of the pump fluences. Amplitude modulation ($T_{off} - T_{on}$) at all fluences (0, 3.82, 19.0 and 63.6 μJ/cm^2) has been calculated with respect to corresponding transmission amplitude at zero pump fluence ($T_{off} \rightarrow 0$ μJ/cm^2). Region near resonance depth and transmission peak have been shaded in blue and grey color, respectively.

5.5 Active switching from toroidal dipole to electric or magnetic dipole

5.5.1 Toroidal to electric dipole switching

In the absence of the pump illumination, the anti-symmetric toroidal mode dominates the overall response at the lower frequency. When the pump beam is switched on, the dark anti-symmetric toroidal mode completely switches off at larger pump fluences and the purely symmetric electric dipole mode is observed at 0.68 THz (figure 5.2b). The symmetric bright

mode always exist in the transmission spectra. We actively switch the metamaterial from the two resonance state (toroidal + dipole) to a single resonant state which is a pure symmetric electric dipole. When the capacitive split gaps are shorted due to the large photoconductivity of silicon pads upon photoexcitation, the metamaterial structure becomes a perfect symmetrical single structure that supports only a bright, broad linewidth electric dipole resonance. Therefore, through optical pumping weakly radiating toroidal mode has been switched to a strongly radiating electric dipolar mode due to the shorting of the capacitive gaps of both TASRs. This switching phenomenon is on the scale of few nano seconds time scale depending on the relaxation dynamics of silicon.

5.5.2 Toroidal to magnetic dipole switching

In continuation, we also numerically examined the situation, where electromagnetic response of mirrored TASR configuration is switched between toroidal dipole (anti-parallel magnetic dipoles) to parallel magnetic dipole type excitation. Figure 5.7 shows the simulated amplitude transmission versus frequency spectra of the metasurface having Si pads below the split gaps of only one TASR in mirrored arrangement. As the conductivity of Si increases, the amplitude of toroidal dipole resonance decreases until we reach a σ_{Si} value of 1200 S/m. Increasing the silicon conductivity beyond this point excites new mode in form of parallel magnetic dipoles. The evolution of new resonance mode is at different frequency (~ 0.4 THz) from the frequency of toroidal resonance (~ 0.415 THz). At the two different conductivities of silicon (σ_{Si} = 0 and 8000 S/m), figure 5.8 shows relative induced moments of electric dipole (P_x), and toroidal dipole (T_x) along the X-direction and the magnetic dipole (M_z) along the Z-direction. Multipole calculations reveals a strong enhancement (more than two orders of magnitude) in strength of magnetic dipole (M_z), as toroidal resonance (grey region) switches to magnetic resonance (green region).

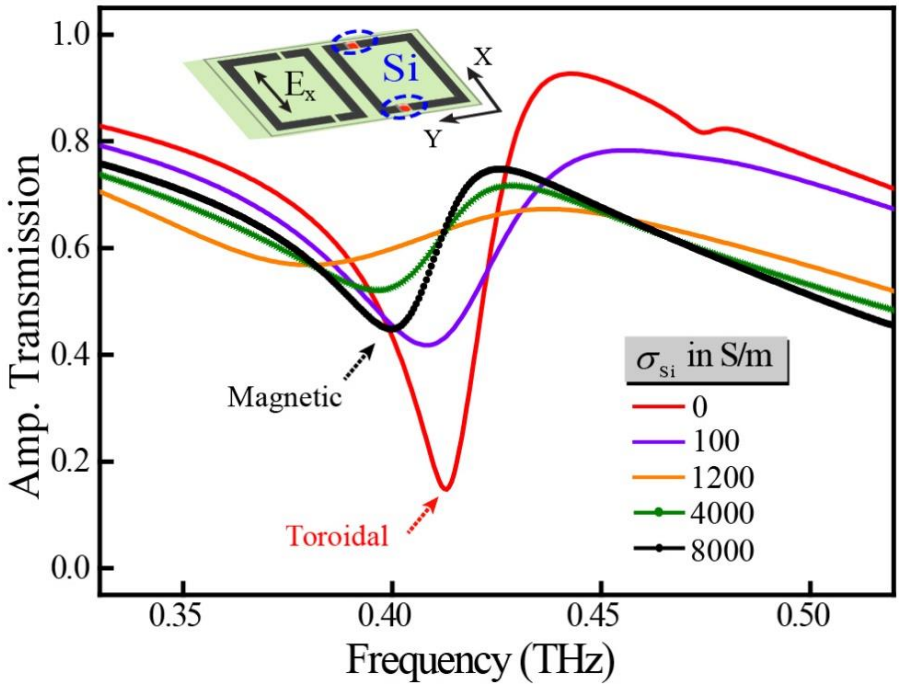

Figure 5.7: Simulated amplitude transmission versus frequency plot at different conductivities of Si pads lying below the split gaps of only one TASR in mirrored configuration.

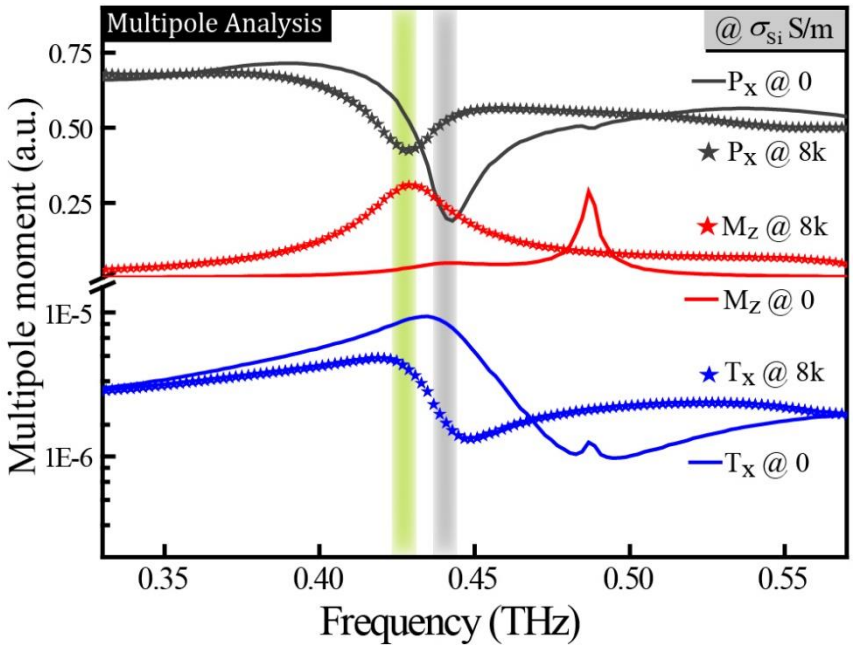

Figure 5.8: Numerically calculated contribution of electric (P_x) , magnetic (M_z) and toroidal (T_x) dipole moments at two different conductivities (σ_{Si} = 0 and 8000 S/m) of silicon pads lying below the split gaps of only one TASR in mirrored configuration. Shaded region represents the toroidal (grey region) and magnetic (green region) resonance.

5.5.3 Surface currents distribution in multipole switching

To get clear idea about switching the simulated surface currents at resonance for the two different conductivities of silicon are depicted in figure 5.9a, 5.9b, where $\vec{m}$ (magnetic dipole vector) corresponds to loop current of individual TASR in mirrored configuration. At $\sigma_{Si} = 0$ (see figure 5.9a) the strong excitation of both TASRs corresponds to toroidal dipole (anti-parallel magnetic dipoles). With increase in conductivity, one of the TASR with photo-excited silicon pads quenches the magnetic moment resonance at lower frequency (~ 0.4 THz)(see figure 5.9b), which eliminates toroidal coupling between the TASR pair and the only strong excitation is due to one TASR (without silicon pads), which is of magnetic dipole type. In fact, under the influence of strongly excited resonator (without silicon pads), TASR with silicon

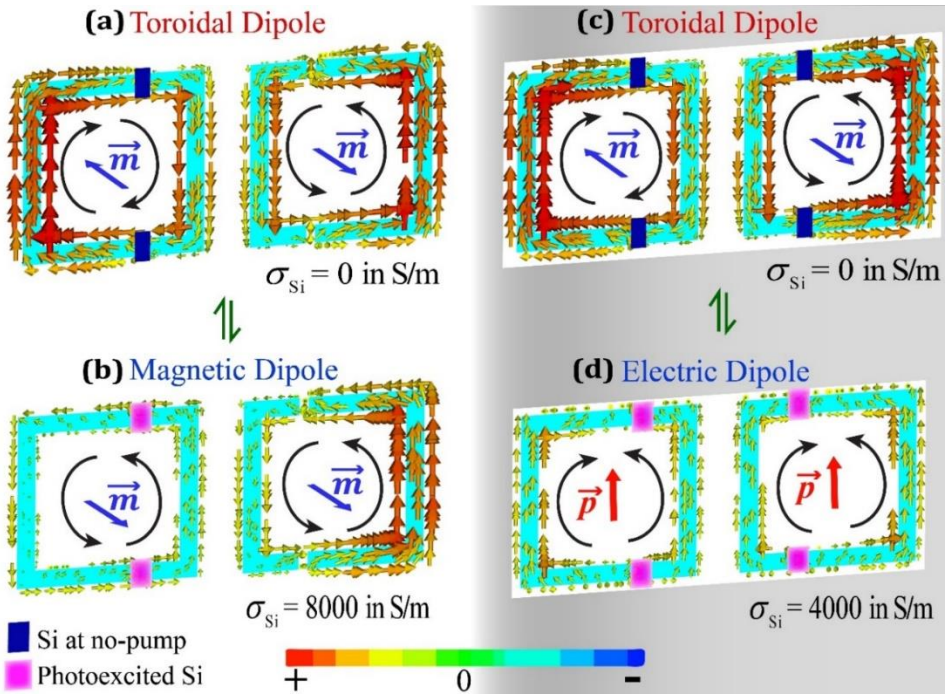

Figure 5.9: (a, b) Simulated surface currents at 0 and 8000 S/m conductivity of silicon pads lying below the split gaps of only one TASR in mirrored configuration. (c, d) Surface current distribution at 0 and 4000 S/m conductivity of Si pads lying below the split gaps of both TASR in mirrored configuration. Here $\vec{p}$ and $\vec{m}$ denote electric and magnetic dipole moments, respectively.

pads carries identical current distribution, but of very weak strength, thus having its $\vec{m}$ vector identical to strongly excited TASR. This makes the whole array resemble a magnetic dipole oriented in the same direction. To differentiate this scheme from the one with the fabricated sample, where silicon pads are present in gaps of the mirrored TASR pair during the 'off'(see figure 5.9c) and 'on'(see figure 5.9d) instance of pump beam, where the nature of currents in individual TASR switches from antiparallel to parallel (electric dipole excitation) behaviour. At this instant, the toroidal cavity fails to store electromagnetic energy which lowers the amplitude of resonance compared to a situation when there is no pump illumination.

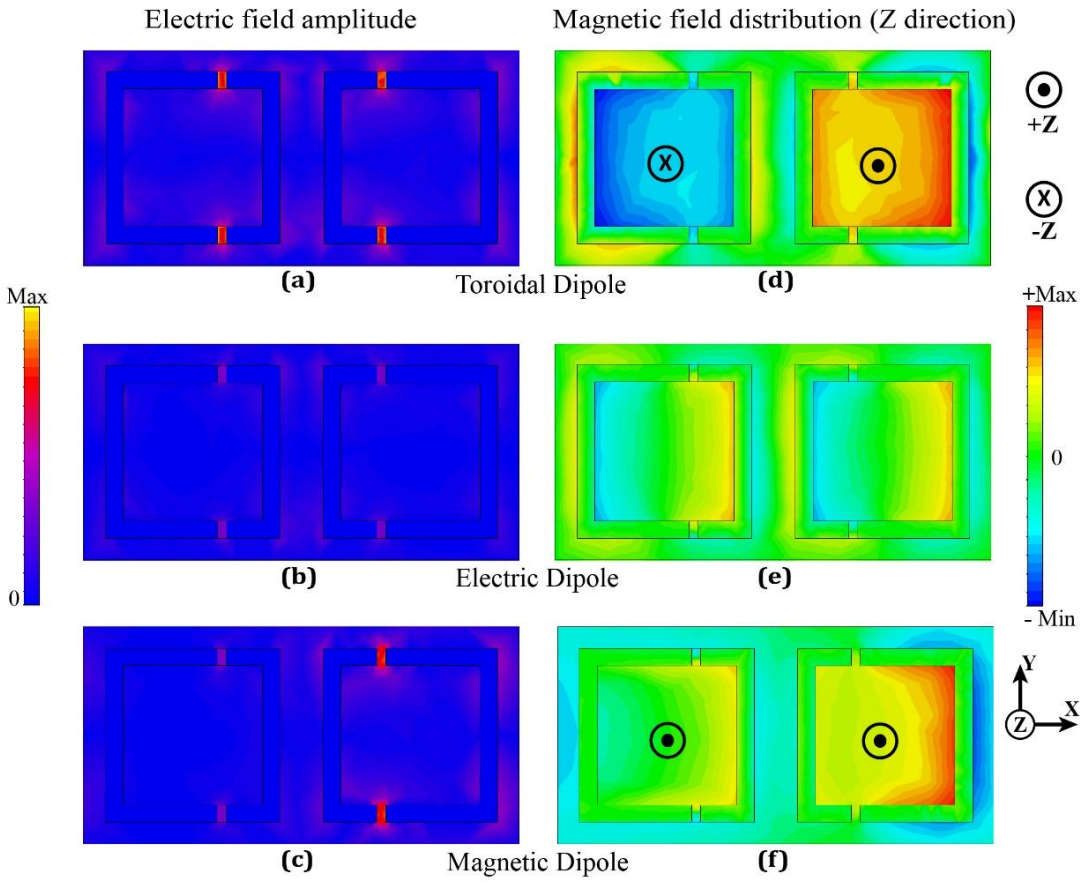

Figure 5.10: Simulated electric field amplitude (a, b, c) confined in the split gaps of mirrored TASRs and magnetic field distribution (d, e, f) inside coupled TASRs along the Z-direction, as electromagnetic excitation of mirrored TASRs switches from toroidal dipole (a, d) to electric dipole (b, e) or magnetic (c, f) dipole.

Switching between the different types of dipoles can be further understood by the simulated results for electric/magnetic field distribution in figure 5.10. Figure 5.10a, 5.10b, 5.10c shows electric energy confined in the split gaps of mirrored resonators as toroidal dipole switches to electric or magnetic dipole. Energy confined is maximum for the toroidal dipole and minimum for the electric dipole. Further, as the nature of electromagnetic response switches from toroidal to magnetic, the magnetic field concentration along the Z-direction (perpendicular to the plane of array), as shown by figure 5.10d and figure 5.10f, also switches from antisymmetric (+Z, -Z) to symmetric (+Z, +Z) for mirrored TASR pair. Thus, depending upon the selective location of the silicon pads in split gaps of mirrored TASRs, one can tailor the nature of electromagnetic radiation from a toroidal dipole to either a magnetic or an electric dipole.

5.6 Conclusion

In summary, electromagnetic excitation of multipoles is a useful tool to capture the inherent properties of electromagnetically active media. Actively controlled electromagnetic features of various multipoles, ranging from non-radiating to strongly radiating, in one device would certainly have a key role in designing resonance-based sensing, lasing and ultrafast switching devices. We have demonstrated the dynamic switching of toroidal response to the fundamental electric or magnetic response in a single metamaterial device, through selective inclusion of active elements in a hybrid metamolecule design. We also recorded significantly high peak to peak amplitude modulation of 73% as electromagnetic resonance switches from toroidal to electric dipole. Our approach provides a new and promising method for designing novel toroidal resonance based active devices and narrow band active filters at the terahertz frequency regime.

Chapter 6

Toroidal Metamaterial Sensing

Localized electromagnetic excitation in the form of toroidal dipoles has recently been observed in metamaterial systems. The origin of the toroidal dipole lies in the currents flowing on the surface of a torus. Thus, the exotic toroidal excitations play an important role in determining the optical properties of a system. Toroidal dipoles also contribute towards enabling high quality factor subwavelength resonances in metamaterial systems which could be an excellent platform for probing the light matter interaction. Here, we demonstrate sensing with toroidal resonance in a two-dimensional terahertz metamaterial in which a pair of mirrored asymmetric Fano resonators possess anti-aligned magnetic moments at electromagnetic resonance that gives rise to a toroidal dipole. Our proof of concept demonstration opens up an avenue to explore the interaction of matter with toroidal multipoles that could have strong applications in sensing of dielectrics and biomolecules. This scheme could also be useful in investigating the interaction of magnetic materials in the vicinity of toroidal metasurface.

6.1 Introduction

Over a long period, light matter interaction has attracted tremendous attention of the scientific community and has emerged as a powerful tool to manipulate the electromagnetic (EM) response of matter for almost entire range of EM radiation. Varieties of light matter interaction

based electromagnetic devices are currently being employed in the area of telecommunication, imaging, healthcare, and defense industry. Metamaterials, which are the composite array of sub-wavelength structures, are one such kind of devices that offers novel effects by controlling the response that originates from the interaction between meta-atoms and electromagnetic radiation.[110,126] Remarkable functionalities such as slow light effects,[95] negative refraction,[27] super lenses,[134] invisibility cloaks,[29] and sensing have been demonstrated using metamaterial based devices.[32,109,135] The unique advantage of metamaterial structure is to support electromagnetic resonance at specific frequency based on their structural size. Such a unique tuning ability can strengthen the adaptability of the metamaterial based electromagnetic devices in the near future.

Promising applications offered by metamaterials device designs is very much dependent on their performance. The low performance of these kinds of devices is mainly due to the radiative and non-radiative losses encountered in these systems.[136] Several schemes have been demonstrated to overcome the losses such as by optimizing the shape and size of sub-wavelength structure in the unit cell of metasurface,[111,137,138] by using low loss superconductor or by introducing gain medium.[139] The performance of all metamaterial and plasmonic based devices would certainly be enhanced by overcoming the losses. One of the direct device application of metamaterial is that of a sensor at optical,[140] infrared,[141] and terahertz (THz) frequencies.[142] In recent times, among different frequency bands, terahertz sensing has received a lot of attention due to their remarkable scientific and technological ability in multidisciplinary fields.[86,87] For ultrasensitive sensing applications, there is requirement of high quality (Q) factor resonances that have extremely narrow bandwidth. Moreover, the amplitude of resonance should be strong enough so that it is easier to detect them in a noisy environment. Together with high Q resonance there should be some region, for example split gap region in the split ring resonator, where field are confined during resonance that could be accessed by

the dielectric material, which has to be sensed. The resonances supported by metamaterial structures respond to the changes in the effective refractive index of the medium at their surface.[122,143] Thus, metamaterials provide a robust sensing platform since they could be easily fabricated on different type of thin substrates, which can also be flexible in nature.[144,145]

6.2 High *Q* toroidal excitation for sensing

In this chapter, we have demonstrated terahertz domain refractive index sensing with toroidal dipolar resonance in planar metamaterials, which is easy to fabricate in single step photolithography cycle. In metamaterial system, toroidal dipolar response was first demonstrated at microwave regime by using metasurface composed of 3D metamolecule structures.[73] It was recently discovered that even planar metasurfaces could support strong toroidal resonances, which are high-*Q* in nature and could provide sufficiently large field confinement necessary for sensing applications.[131,146] The overall response of the metamaterial array can be seen as the contribution due to different multipoles, where contribution due to specific toroidal multipole can be analytically computed by multipole analysis.[70,72] In a two-dimensional metasurface, toroidal response can be excited by using symmetry broken split ring resonator also known as asymmetric split ring resonator or Fano resonators.[107,146] Metamolecule array of toroidal metasurface consist of mirrored Fano resonator pair which are coupled through toroidal moment during electromagnetic excitation due to anti-aligned set of magnetic dipoles.[146] In planar metasurface, mirrored asymmetric resonator array, having similar degree of asymmetry, possesses significantly higher *Q* and figure of merit (FoM) values for toroidal resonance compared to traditional Fano resonator array.[146] High *Q* toroidal resonances support strong interaction between the electromagnetic wave and a specific analyte. Minute quantity of analyte on metasurface results in very small spectral shifts of toroidal resonance, which allows the detection of dielectric medium or biological local environment

near the metasurface. Additionally, sharp toroidal resonance offers better sensing performance compared to broad resonances, which typically lack the ability to detect small spectral shifts in the resonance frequency.[133,147] Thus, high-*Q* toroidal metasurface offers another important sensing platform with enhanced sensitivities which could give rise to an excellent photonic device for highly sensitive dielectric, chemical, liquid sensing and biological sensing applications.[148-150]

6.2.1 Design and fabrication

We performed terahertz time domain spectroscopy (THz-TDS) to measure the sensing parameters of high-*Q* planar toroidal metasurface. A close agreement between simulated and experimental response substantiate the role of toroidal resonance in THz sensing. Figure 6.1a shows the diagrammatic image of terahertz asymmetric split ring resonator (TASR), which consists of double split gap square shaped metallic strip. The outer dimension of individual resonator is 60 µm × 60 µm, with arm width of 6 µm and the split-gap size equal to 3 µm. The asymmetric nature of the TASR structure is due to positioning of both the split gaps, which are located 9 µm away from the center of the resonator. The TASR metamaterial samples were fabricated on high-resistivity (4 kΩ-cm), p-type silicon (0.5-mm thick) substrate using photolithography followed by deposition of a 200-nm thick aluminium (Al) film in thermal evaporator. During the experiments, a high-resistivity (4 kΩ-cm), 10-mm thick silicon plate was used for an optical contact behind the metamaterial surface to eliminate the Fabry Perot reflection from the back surface of the substrate, which enabled a scan length of 60 ps in the time domain, providing a measurement frequency resolution of 16.6 GHz. For the excitation of toroidal resonances in planar metasurface, the TASRs are arranged in mirrored configuration, separated by the distance of 15 µm, as shown in microscopic image (figure 6.1b) of the sample. Sample image shows that the TASRs are mirrored to each other along the Y-direction. The unit

cell area with periodicity of 150 µm × 75 µm is shown by the dotted rectangular curve, which on repetition along XY-plane forms the planar toroidal metasurface.

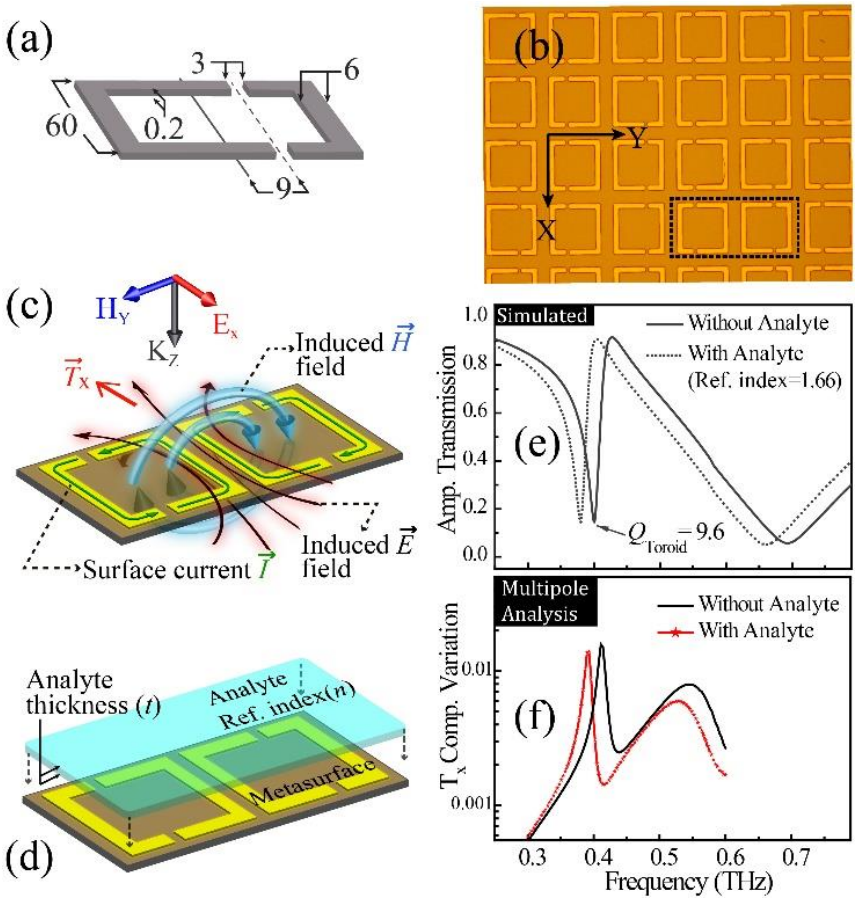

Figure 6.1: High *Q* planar toroidal metasurface. (a) Dimensional features of terahertz asymmetric split ring resonator (TASR) with all dimensions at micron scale. (b) Microscopic image of toroidal metasurface along XY-plane, with unit cell representation shown by dotted rectangular curve. (c) Artistic impression of toroidal dipole generated due to circulating magnetic field produced by surface currents induced in mirrored TASR configuration. (d) Unit cell of toroidal metasurface coated with analyte layer on the top. (e) Simulated frequency versus amplitude transmission spectra of metasurface with and without analyte layer. (f) Numerically calculated X-component of toroidal dipole moment versus frequency plot, via multipole analysis in the vicinity of toroidal resonance, for the case of with and without analyte layer on metasurface.

The metasurface is excited by the THz pulse at normal incidence, which has its electric field polarized parallel to the non-gap arm of TASR. Figure 6.1c shows the schematic of toroidal

excitation in the unit cell of metasurface due to mirrored TASRs configuration. At the instant of toroidal resonance surface currents $(\vec{I})$ excited in the pair of TASRs are opposite in nature which confines induced time varying magnetic field $(\overrightarrow{H})$ in a small circular region. This induced dynamic $\overrightarrow{H}$ field further induces dynamic electric field $(\vec{E})$, which as per right hand rule points along X-direction shown by the fictitious arrow of a toroidal dipole vector $(\overrightarrow{T_x})$. For sensing, when a photoresist layer of thickness *t* and refractive index (*n*) equal to 1.66 is spin coated on the top of the toroidal metasurface, as shown in figure 6.1d, a red shift in the frequency of toroidal resonance can be clearly observed, as depicted by the simulated amplitude transmission spectra of metasurface in figure 6.1e. The simulated *Q* factor of the toroidal resonance is ~ 9.6, which indicates the sharpness of resonance near resonance frequency. Even at larger degree of asymmetry in TASR, excited toroidal resonance is of sufficiently narrow linewidth and has large amplitude, which allows to precisely detect the red shift in the resonance frequency during the experiments. Further, to investigate the role of toroidal dipole in sensing activity, X-component of toroidal dipole has been calculated numerically near the spectral region of sharp resonance. In the presence of analyte medium, T_x component versus frequency plot in figure 6.1f clearly indicates the redshift in toroidal coupling between the mirrored resonators, which is responsible for the shift in toroidal resonance.

6.2.2 Photoresist sensing with confined field of metasurface

Planar toroidal metamaterials are spin coated with different thicknesses of photoresist. Profilometry was used to detect the thickness of photoresist layer by scratch method. Commercially available CST Microwave Studio was used to numerically simulate the coated

metasurface response. Figure 6.2a shows the simulated amplitude transmission spectra of toroidal metasurface where we observe red shifting of the toroidal resonance with increasing thickness of photoresist. Without photoresist film (t=0 μm), the toroidal dipole resonance first appears at frequency 0.402 THz, which for film thickness 1.5, 3.0, 9.0 and 13.5 μm are gradually red shifted by 12.5, 16.2, 24.0, and 25.8 GHz. It is also evident that beyond film thickness of 9 μm, the red shift in toroidal dipole resonance nearly saturates at frequency 0.376 THz. Figure 6.2b shows the experimentally measured response which agree well with the simulations. The red shift in resonance frequency mainly caused by the dielectric fill in the capacitive gaps of TASRs, which increases the net capacitance of TASRs and alters the

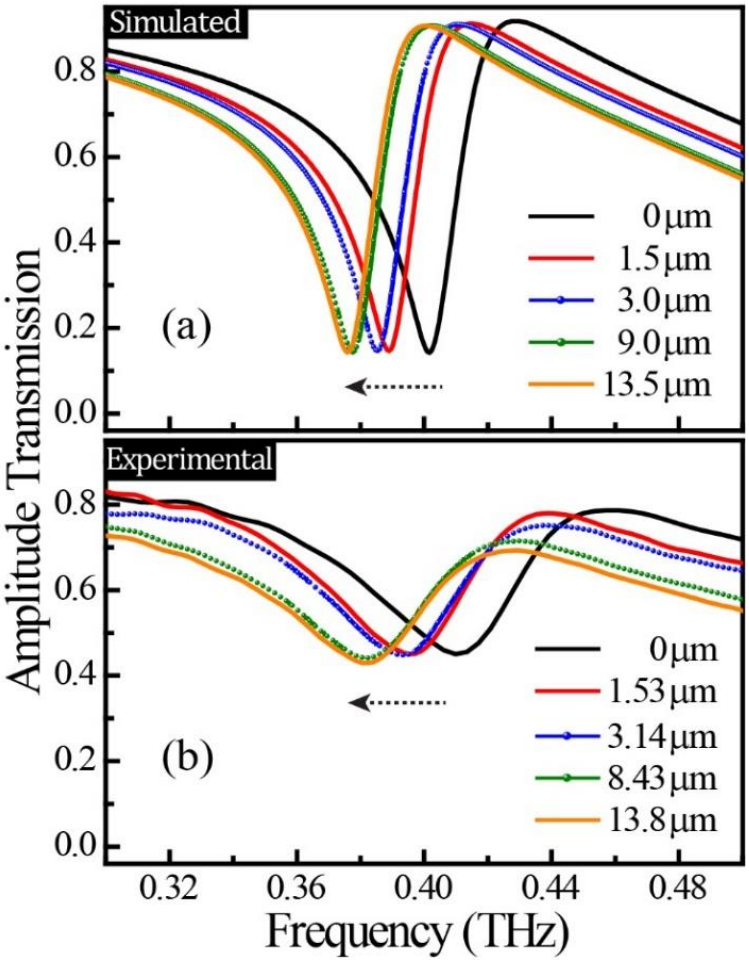

Figure 6.2: Spectral shift in toroidal resonance**.** (a) Simulated and (b) experimentally measured amplitude transmission spectra with different thickness of photoresist coated on the top of metasurface. Dotted arrow pointing towards the left shows the shift in the frequency of toroidal resonance.

resonance frequency. Also, fringing field effect at the capacitive gaps further plays a role in the red shift of toroidal resonance with increase in the thickness of photoresist layer. Once, the penetration of fringing fields above certain height from the metasurface disappears, no shift is observed in frequency of resonance even with the increase in the thickness of photoresist layer.

6.2.3 Fringing field effects in sensing

Further, to investigate the spatial extent of the fringing fields above the metasurface we have plotted the frequency shift with respect to the analyte thickness. For the simulated response, figure 6.3a shows the variations in frequency shifts along with exponential fit as the thickness

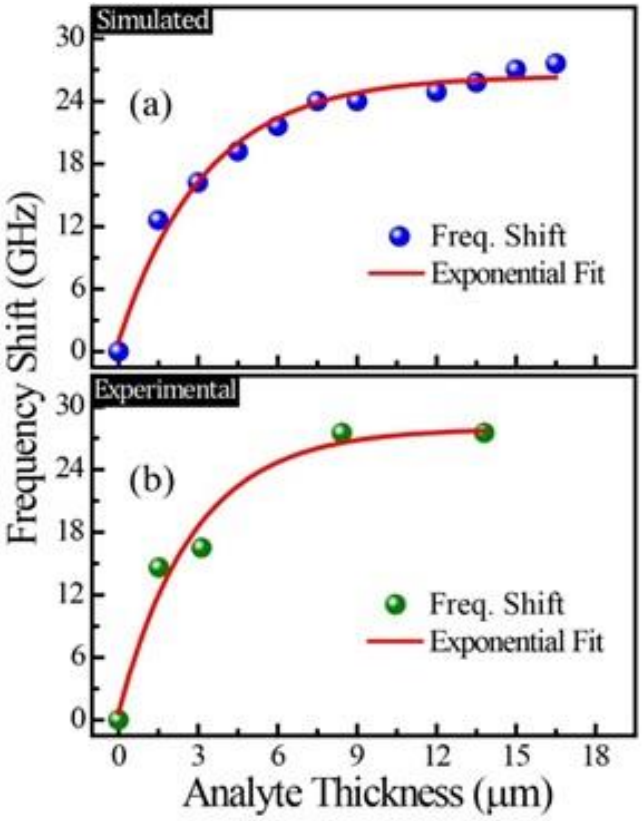

Figure 6.3: Exponential fit for frequency shifts. (a) Simulated and (b) experimentally measured frequency shift with increase in the thickness of analyte (photoresist) layer. Exponential fit has been performed equation $f_{shift} = f_{sat} + A*\exp(-R_0*t)$, where t is analyte thickness, f_{sat} is the maximum frequency shift at saturation point of fitted curve.

of analyte layer increases. The exponential fit curve nearly saturates beyond the thickness of 10 µm. This gives a fair idea of the penetration depth of fringing fields above the metasurface. Almost similar variation is observed for the measured response, as shown in figure 6.3b. Saturated frequency shift from the exponential fit curve for the measured response (27.9 GHz) differs by 1.5 GHz compared to simulated response (26.4 GHz), which is lower than the frequency resolution of our measurements (16.6 GHz).

6.3 Sensitivity for thin analyte layers

To experimentally determine the sensitivity for thin analyte layers, we coated new set of samples with 0.25 µm thick layer of Silicon dioxide (SiO_2) and Germanium (Ge), due to high contrast in their refractive index. Table I shows the resonance frequencies and corresponding refractive index for specific analyte material. To identify shift in toroidal resonance (where simulated and experimentally measured *Q* factor of the resonance mode used in sensing are 9.6 and 7.6, respectively), nitrogen (N_2) environment is used as the reference medium for both materials.[159] Significant shift in resonance frequency compared to N_2 environment, can be observed in simulated (see figure 6.4a) and experimental (see figure 6.4b) transmission spectra for thin film coating of SiO_2 (n_{SiO2}=1.98) and Ge (n_{Ge}=4).[157, 158] For thin films (~0.25 µm), experimentally estimated value of sensitivity from figure 6.4c is found to be around 6 GHz/refractive index unit (RIU), which matches well with simulated results (inset plot). This lower sensitivity value is for the ultrathin 250 nm thickness of the analyte. The equivalent sensitivity per micron of thickness of the analyte is 24 GHz/ RIU.

Table 6.1. Table depicting experimental resonance frequency of toroidal metasurface in presence of corresponding refractive index analyte medium (N_2, SiO_2, Ge) on metasurface

Analyte on metasurface	Resonance Frequency (GHz)	Refractive Index (n)
Nitrogen (N_2)	422.6	1
0.25 µm thick SiO_2 layer	415.3	1.98
0.25 µm thick Ge layer	404.3	4

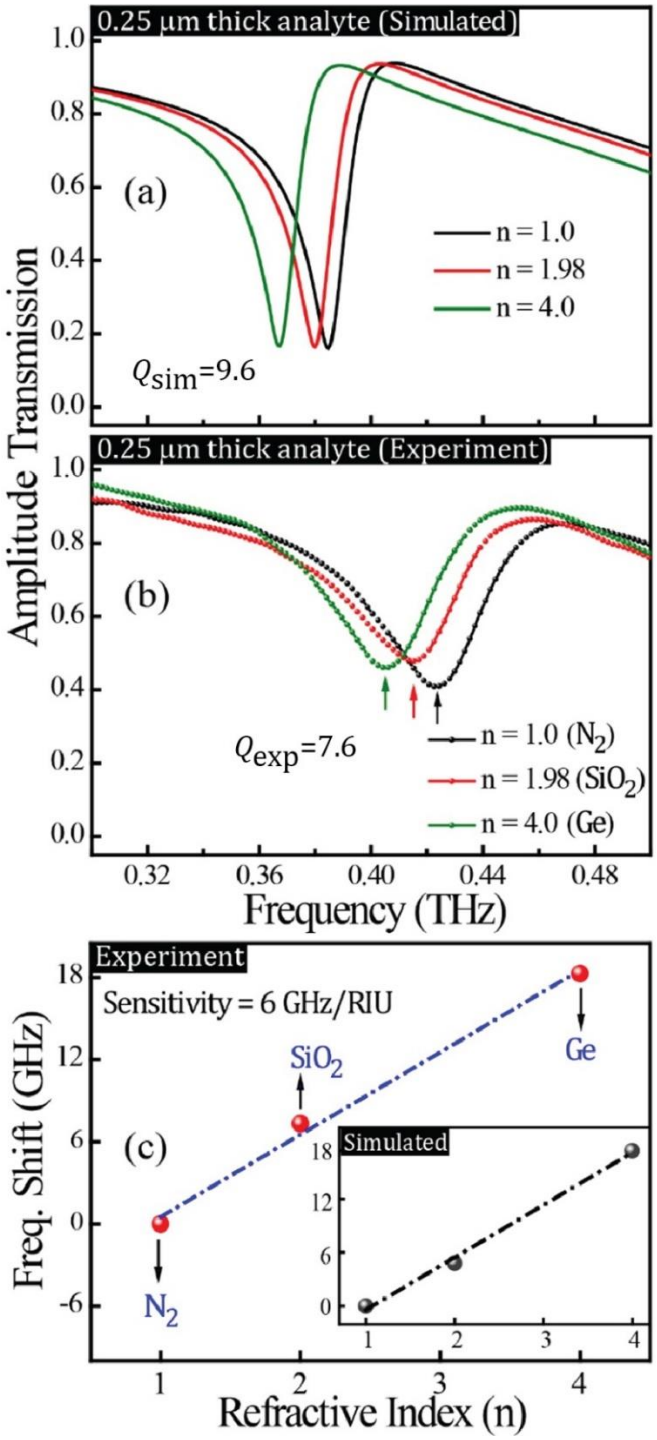

Figure 6.4: Sensitivity of 0.25 μm ultrathin analyte layer. (a) Simulated and (b) experimentally measured amplitude transmission spectra showing shift in toroidal resonance (where simulated and experimentally measured *Q* factor of resonance mode are 9.6 and 7.6, respectively) with different analytes, where nitrogen (N_2) environment is used as reference medium for 0.25 μm thick analyte layer of silicon dioxide (SiO_2) and germanium (Ge) coated on the top of metasurface. (c) Resonance frequency shift versus refractive index plot for samples coated with SiO_2 and Ge.

We also analyzed the sensitivity of the toroidal resonance for sufficiently thick analyte layers by varying the refractive index (*n*) of the analyte layer to be sensed. Figure 6.5a shows the shift in the resonance frequency of simulated toroidal dipolar response with increase in the refractive index (*n*) of constant thickness (4 µm) analyte layer. The variation in frequency shifts (as shown in figure 6.5b) appears to be linear in nature, so we performed linear fit to determine the sensitivity, which turns out to be 27.3 GHz/RIU. The measure of sensitivity value is estimated

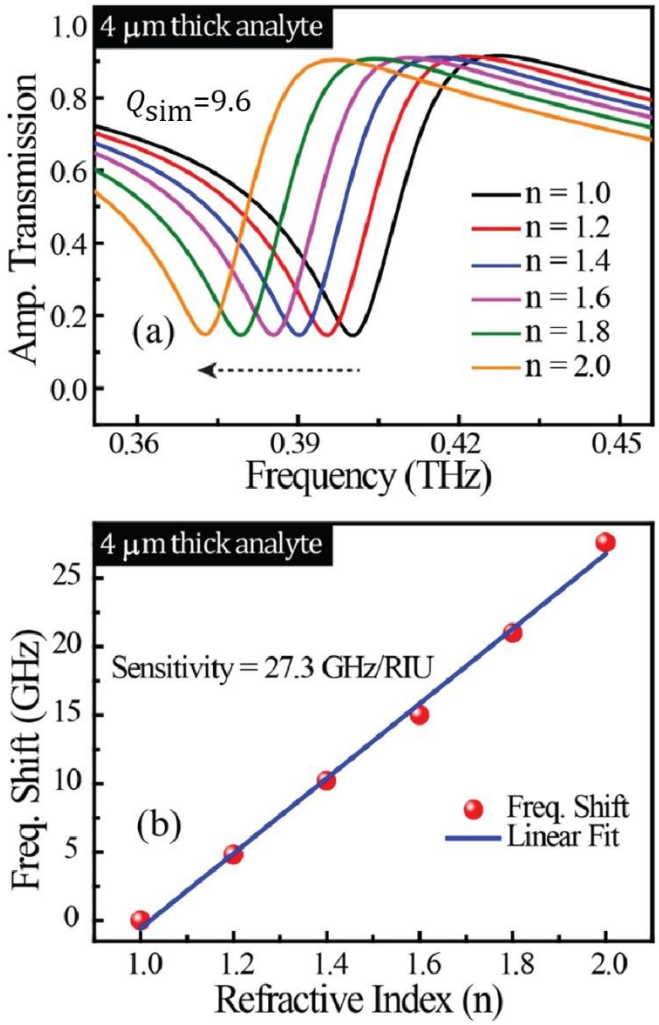

Figure 6.5: Sensitivity of toroidal resonance. Simulated (a) red shifted amplitude transmission spectra, and correspondingly derived, where *Q* factor of the resonance mode used for sensing is around 9.6. (b) frequency shift vs refractive index plot for 4 µm thick analyte layer, with increasing refractive index, coated on toroidal metasurface. Linear fit has been performed to determine sensitivity of metasurface.

in terms of wavelength (Δλ) per RIU, which is given by equation $\left|\frac{d\lambda}{dn}\right| = \frac{c}{f_o^2} * \frac{df}{dn}$, where c is speed of light, f_o is the resonance frequency, and n represents the refractive index of analyte. In terms of Δλ/RIU , the sensitivity value that we have obtained for the toroidal metasurface for 4 μm thick layer of analyte is 4.88×10^4 nm/RIU . The sensitivity values of planar toroidal metasurface are lower compared to previously reported values of Fano resonators array.[109]

6.4 Analyte and substrate thickness dependent sensitivity

Moreover, to probe the analyte and substrate thickness dependent sensitivity of toroidal metasurface, we calculated sensitivities for different thicknesses of analyte layer for toroidal metasurface on silicon (Si) and mylar substrate. Figure 6.6a shows the sensitivity plot for increasing thickness of analyte layer coated on toroidal metasurface on 25 μm thick Si and mylar substrate. Mylar substrate gives better sensitivity compared to Si substrate due to the lower refractive index of mylar (n_{mylar}=1.54).[156]

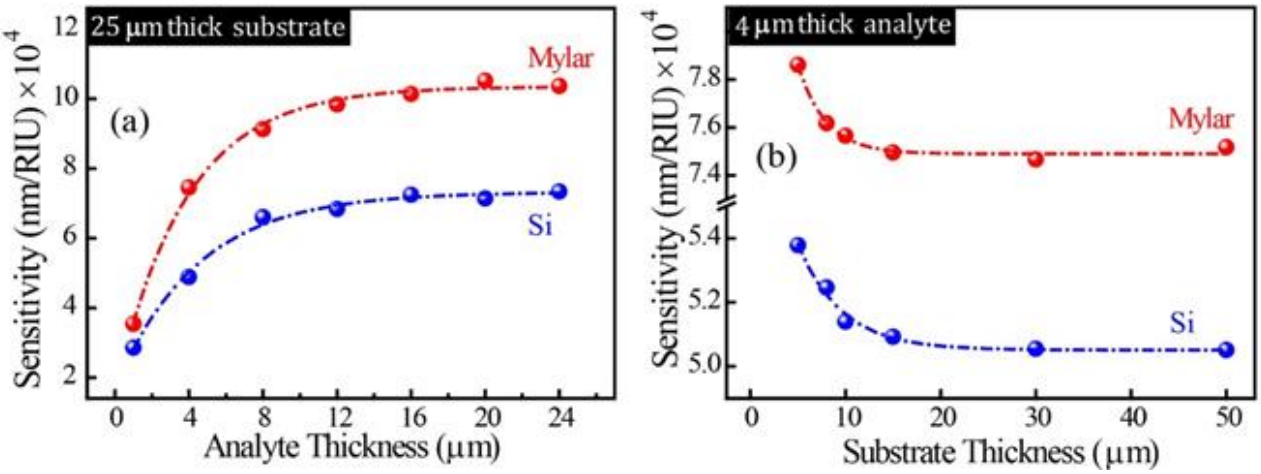

Figure 6.6: Simulated sensitivities plot with different thickness analyte layer with varying refractive index coated on toroidal metasurface fabricated on 25 μm thick silicon (Si) and mylar substrate. (b) 4 μm thick analyte layer of varying refractive index coated on metasurface patterned on substrate (Si, Mylar) with increasing thickness. Exponential fit (dotted curve) performed to determine the maximum sensitivity.

We note that the sensitivity of toroidal resonance increases and subsequently saturates with increase in the thickness of the analyte layer. The maximum sensitivity for toroidal metasurface is found to be 41 GHz/RIU (7.32×10^4 nm/RIU) for Si and 186 GHz/RIU (10.3×10^4 nm/RIU) for the mylar substrate. The sensitivity plot nearly tends to saturate beyond 13 μm thick analyte layer. Lastly, to probe the effect of substrate thickness on sensitivity, simulations have been performed for toroidal metasurface patterned on different thickness substrate (Si, mylar), and coated with constant thickness analyte layer of 4 μm. As shown in figure 6.6b, the sensitivity decays exponentially with increase in the thickness of substrate and nearly saturates beyond substrate thickness of 20 μm.

6.5 Conclusion

In brief, we demonstrate that toroidal resonances in planar metamaterials could be used as a platform for sensing applications. We have experimentally demonstrated high-*Q* sensing via sharp toroidal resonance at terahertz spectral range. High resolution terahertz measurements allow us to measure the minute shift in the resonance frequencies as ultrathin layers of dielectric film was coated on top of the toroidal metasurface. Compared to other sharp resonances in metamaterials, toroidal dipole resonance offers better sensitivity at larger asymmetry in TASRs, despite short scan duration on time scale. The impact of our work lies in identifying high-*Q* terahertz toroidal metasurface based sensing that would drive the path for innovative design and realization of photonic devices for dielectric, chemical and biomolecular sensing with spectral signatures in the terahertz regime.

Chapter 7

Summary and Future Research Directions

In recent years, optics and photonics have dramatically influenced the technological and economical advances, which have major impact on our day-to-day life. Photonics, which deals with the light manipulation through transmission, modulation, switching, sensing, is one of the rapidly growing field in the research community. Metamaterial is one of the well-known and widely explored research area in the field of photonics, because it gives flexible platform in tailoring electromagnetic radiation, and their resonance features could be extended to different range of electromagnetic spectrum. The aim of this thesis was to enhance the efficiency of planar metasurface by introducing near field toroidal coupling, that could be used as a suitable platform for investigating light matter interaction, and in developing real-world applications such as ultrasensitive sensing, active switching, and efficient modulation of terahertz waves. The work presented in this thesis manifests great prospects and pathways for new generation terahertz metaphotonic devices. In chapter 3, we first presented the excitation of sharp asymmetric resonance mode in a single four split gap resonator at the terahertz regime of electromagnetic spectrum. These sharp resonance modes resulted due to interference between electric dipole resonance (bright mode) and toroidal dipole resonance (dark mode). We also demonstrated passive control of amplitude and linewidth of resonance by tuning the strength

of toroidal coupling. In chapter 4, we have discovered a method to couple neighboring Fano resonators in planar metasurface through toroidal coupling by mirroring neighboring resonators along the direction perpendicular to the incident electric field polarization. This kind of arrangement drastically reduces the radiative loss, without affecting the amplitude of resonance. These results would enable selective engineering of radiative losses that has crippled the metamaterial community and act as a design principle for metamaterial based active and passive devices that have potential applications in the terahertz frequencies for high sensitivity sensing, non-linearity and lasing.

All the investigations presented in the initial chapters are based on passive scheme of tuning toroidal coupling mediated asymmetric resonance, while the results presented in the latter part of this thesis are based on the active scheme where photoexcitation is used to control the toroidal coupling. The theoretical scheme presented in chapter 5 introduces strategy to incorporate multi-resonance features dominated by different multipole excitation, such as electric dipole, magnetic dipole, and toroidal dipole, by selective inclusion of active elements in the mirrored configuration of the resonator array. Moreover, we experimentally demonstrated active tuning in the coupling strength mediated by toroidal moment that resulted in modulation of asymmetric resonance at different pump power. Finally, in chapter 6 we experimentally demonstrated the application of toroidal modes in dielectric sensing. Although, the sensitivity remained low compared to conventional Fano resonators when there is no toroidal coupling, but sharp resonances clearly detected resonance shift for few hundred nanometers thick dielectric layer on metasurface, with low scan duration on picosecond time scales.

The results presented in this thesis are proof of concept demonstrations and therefore, there is room for further investigations. Some of the proposed future research directions are listed below.

Multi-resonance featured planar metasurface and dynamic switching between different excitation modes proposed in this thesis can have significant impact in controlling the electromagnetic excitations in free space and matter that could have potential applications in designing efficient sensors, filters, and modulators. Thus, incorporating MEMS based cantilever actuation can easily allow switching between electric, toroidal and magnetic resonance modes by means of cantilever inclination.

Superconductors effectively enhance the *Q* factors of the low asymmetry Fano resonant metamaterials in a regime where radiative losses are effectively suppressed and thus the loss mechanism is dominated by ohmic loses. Thus, on incorporating high-T_c superconductors in a recently developed planer toroidal metamaterials, which effectively suppress radiative losses by forming a mirrored configuration, could potentially further enhance the maximum achievable *Q* factors.

Next set of studies would involve to develop new platform with high mode volume where semiconducting materials could be incorporated in order to enhance the switching speed, sensitivity and the stability of the device for the future generation low cost and ultrafast active photonic devices.

Appendix 1

Publications
Journal publications during PhD candidature

1) Manoj Gupta, Yogesh Kumar Srivastava, and Ranjan Singh (2018). "A Toroidal Metamaterial Switch", *Advanced Materials*, 30(4). doi:10.1002/adma.201704845

2) Manoj Gupta, Yogesh Kumar Srivastava, Manukumara Manjappa, and Ranjan Singh (2017). "Sensing with toroidal metamaterial", *Applied Physics Letters*, 110(12). doi:10.1063/1.4978672

3) Manoj Gupta, and Ranjan Singh (2016). "Toroidal versus Fano Resonances in High Q planar THz Metamaterials", *Advanced Optical Materials*, 4(12), 2119-2125. doi:10.1002/adom.201600553

4) Manoj Gupta, Vassili Savinov, Ningning Xu, Longqing Cong, Govind Dayal, Shuang Wang, Weili Zhang, Nikolay I. Zheludev, and Ranjan Singh (2016). "Sharp Toroidal Resonances in Planar Terahertz Metasurfaces", *Advanced Materials*, 28(37), 8206-8211. doi:10.1002/adma.201601611

Co-author contribution

1) Wen Xiang Lim., Song Han, Manoj Gupta, Kevin F. MacDonald, and Ranjan Singh (2017). "Near-infrared linewidth narrowing in plasmonic Fano-resonant metamaterials via tuning of multipole contributions", *Applied Physics Letters*, 111(6). doi:10.1063/1.4997423

2) Song Han, Manoj Gupta, Longqing Cong, Yogesh Kumar Srivastava, and Ranjan Singh (2017). "Toroidal and magnetic Fano resonances in planar THz metamaterials", *Journal of Applied Physics*, 122(11). doi:10.1063/1.5001246

Copy Right/ Reprint Permission

Major portion of chapter 3 has been reproduced from the article "Sharp Toroidal Resonances in Planar Terahertz Metasurfaces", Manoj Gupta, Vassili Savinov, Ningning Xu, Longqing Cong, Govind Dayal, Shuang Wang, Weili Zhang, Nikolay I. Zheludev, and Ranjan Singh, *Advanced Materials*, 28(37), 8206-8211 (2016). Copyright Wiley-VCH Verlag GmbH & Co. KGaA. Reproduced with permission.

Entire portion of chapter 4 has been reproduced from the article "Toroidal versus Fano Resonances in High Q planar THz Metamaterials", Manoj Gupta, and Ranjan Singh, *Advanced Optical Materials*, 4(12), 2119-2125 (2016). Copyright Wiley-VCH Verlag GmbH & Co. KGaA. Reproduced with permission.

Entire portion of chapter 5 has been reproduced from the article "A Toroidal Metamaterial Switch", Manoj Gupta, Yogesh Kumar Srivastava, and Ranjan Singh, *Advanced Materials*, 30(4), 1704845 (2018). Copyright Wiley-VCH Verlag GmbH & Co. KGaA. Reproduced with permission.

Entire portion of chapter 6 has been reproduced from the article "Sensing with toroidal metamaterial", Manoj Gupta, Yogesh Kumar Srivastava, Manukumara Manjappa, and Ranjan Singh, *Applied Physics Letters*, 110(12), 121108 (2017). Copyright American Institute of Physics (AIP). Reproduced with permission.

References

(1) Oldano, C.; Becchi, M. *Pramana* **1999**, *53*, 131.

(2) Young-Wan, K.; Hoon, C. D.; Jung-Il, J. I. N. *Polymer journal* **2012**, *44*, 1191.

(3) Almeida, E.; Bitton, O.; Prior, Y. *Nature Communications* **2016**, *7*, 12533.

(4) Lee, B.; Kwon, H.; Kim, S.; Rotermund, F. *Opt. Mater. Express* **2016**, *6*, 993.

(5) Yatsugi, K.; Matsumoto, N.; Nagashima, T.; Hangyo, M. *Applied Physics Letters* **2011**, *98*, 212108.

(6) Jiang, Y.; Soufiani, A. M.; Gentle, A.; Huang, F.; Ho-Baillie, A.; Green, M. A. *Applied Physics Letters* **2016**, *108*, 061905.

(7) Suzuki, D.; Oda, S.; Kawano, Y. *Nature Photonics* **2016**, *10*, 809.

(8) Isenberg, J.; Warta, W. *Applied Physics Letters* **2004**, *84*, 2265.

(9) Scheller, M.; Jördens, C.; Koch, M. *Optics Express* **2010**, *18*, 10137.

(10) Liu, Y.; Zhang, X. *Chemical Society Reviews* **2011**, *40*, 2494.

(11) Smith, D. R.; Pendry, J. B.; Wiltshire, M. C. K. *Science* **2004**, *305*, 788.

(12) Zheludev, N. I. *Science* **2010**, *328*, 582.

(13) Shelby, R. A.; Smith, D. R.; Nemat-Nasser, S. C.; Schultz, S. *Applied Physics Letters* **2001**, *78*, 489.

(14) Lipworth, G.; Ensworth, J.; Seetharam, K.; Da, H.; Lee, J. S.; Schmalenberg, P.; Nomura, T.; Reynolds, M. S.; Smith, D. R.; Urzhumov, Y. *Scientific Reports* **2014**, *4*, 3642.

(15) Meinzer, N.; Barnes, W. L.; Hooper, I. R. *Nature Photonics* **2014**, *8*, 889.

(16) Qu, J.; Kadic, M.; Naber, A.; Wegener, M. *Scientific Reports* **2017**, *7*, 40643.

(17) Wang, J.; Yuan, B.; Fan, C.; He, J.; Ding, P.; Xue, Q.; Liang, E. *Optics Express* **2013**, *21*, 25159.

(18) Wood, B. *Laser & Photonics Reviews* **2007**, *1*, 249.

(19) Silveirinha, M. G. *Physical Review B* **2007**, *75*, 115104.

(20) Chevalier, A.; Gomez, S.; Queffelec, P. *Journal of Applied Physics* **2014**, *116*, 124901.

(21) Bose, J. C. *Proceedings of the Royal Society of London* **1898**, *63*, 146.

(22) Viktor, G. V. *Soviet Physics Uspekhi* **1968**, *10*, 509.

(23) Pendry, J. B.; Holden, A. J.; Stewart, W. J.; Youngs, I. *Physical Review Letters* **1996**, *76*, 4773.

(24) Pendry, J. B.; Holden, A. J.; Robbins, D. J.; Stewart, W. J. *JOURNAL OF PHYSICS-CONDENSED MATTER* **1998**, *10*, 4785.

(25) Shelby, R. A.; Smith, D. R.; Schultz, S. *Science* **2001**, *292*, 77.

(26) Smith, D. R.; Padilla, W. J.; Vier, D. C.; Nemat-Nasser, S. C.; Schultz, S. *Physical Review Letters* **2000**, *84*, 4184.

(27) Shalaev, V. M. *Nature Photonics* **2007**, *1*, 41.

(28) Padilla, W. J.; Taylor, A. J.; Highstrete, C.; Lee, M.; Averitt, R. D. *Physical Review Letters* **2006**, *96*, 107401.

(29) Schurig, D.; Mock, J. J.; Justice, B. J.; Cummer, S. A.; Pendry, J. B.; Starr, A. F.; Smith, D. R. *Science* **2006**, *314*, 977.

(30) Zheludev, N. I. *Nature Materials* **2008**, *7*, 420.

(31) Zhang, X.; Liu, Z. *Nature Materials* **2008**, *7*, 435.

(32) Anker, J. N.; Hall, W. P.; Lyandres, O.; Shah, N. C.; Zhao, J.; Van Duyne, R. P. *Nature Materials* **2008**, *7*, 442.

(33) Zhu, W.; Xiao, F.; Kang, M.; Premaratne, M. *Applied Physics Letters* **2016**, *108*, 121901.

(34) Dayal, G.; Ramakrishna, S. A. *Optics Express* **2012**, *20*, 17503.

(35) Lazzarini, C. M.; Tadzio, L.; Fitzgerald, J. M.; Sánchez-Gil, J. A.; Giannini, V. *Physical Review B* **2017**, *96*, 235407.

(36) Chen, H.-T.; Padilla, W. J.; Zide, J. M. O.; Gossard, A. C.; Taylor, A. J.; Averitt, R. D. *Nature* **2006**, *444*, 597.

(37) Chen, H.-T.; Palit, S.; Tyler, T.; Bingham, C. M.; Zide, J. M. O.; O'Hara, J. F.; Smith, D. R.; Gossard, A. C.; Averitt, R. D.; Padilla, W. J.; Jokerst, N. M.; Taylor, A. J. *Applied Physics Letters* **2008**, *93*, 091117.

(38) Yang, Y.; Kravchenko, I. I.; Briggs, D. P.; Valentine, J. *Nature Communications* **2014**, *5*, 5753.

(39) Jung, J.; Lee, J.; Choi, D.; Choi, J.; Jeong, J.; Lee, E.; Neikirk, D. P. *IEEE Photonics Journal* **2015**, *7*, 1.

(40) Zhan, A.; Colburn, S.; Trivedi, R.; Fryett, T. K.; Dodson, C. M.; Majumdar, A. *ACS Photonics* **2016**, *3*, 209.

(41) Shelton, D. J.; Brener, I.; Ginn, J. C.; Sinclair, M. B.; Peters, D. W.; Coffey, K. R.; Boreman, G. D. *Nano Letters* **2011**, *11*, 2104.

(42) Li, G.; Zhang, S.; Zentgraf, T. *Nature Reviews Materials* **2017**, *2*, 17010.

(43) Yu, N.; Capasso, F. *Nature Materials* **2014**, *13*, 139.

(44) Droulias, S.; Jain, A.; Koschny, T.; Soukoulis, C. M. *Physical Review B* **2017**, *96*, 155143.

(45) Pan, W.; Huang, C.; Pu, M.; Ma, X.; Cui, J.; Zhao, B.; Luo, X. *Scientific Reports* **2016**, *6*, 21462.

(46) Güney, D. Ö.; Koschny, T.; Soukoulis, C. M. *Physical Review B* **2009**, *80*, 125129.

(47) Emani, N. K.; Khaidarov, E.; Paniagua-Domínguez, R.; Fu, Y. H.; Valuckas, V.; Lu, S.; Zhang, X.; Tan, S. T.; Demir, H. V.; Kuznetsov, A. I. *Applied Physics Letters* **2017**, *111*, 221101.

(48) Wu, C.; Arju, N.; Neuner, B.; Eyck, G. T.; Sinclair, M.; Brener, I.; Shvets, G. In *CLEO: 2013* 2013, p 1.

(49) Nanni, E. A.; Jawla, S. K.; Shapiro, M. A.; Woskov, P. P.; Temkin, R. J. *Journal of Infrared, Millimeter, and Terahertz Waves* **2012**, *33*, 695.

(50) Schmidt, R.; Webb, A. *ACS Applied Materials & Interfaces* **2017**, *9*, 34618.

(51) Spang, M.; Albach, M.; Uddin, N.; Thiede, A. *Miniature Dipole Antenna for Active Near-Field Sensor*, 2009.

(52) Al-Naib, I. *Journal of Infrared, Millimeter, and Terahertz Waves* **2018**, *39*, 1.

(53) Zel'dovich, I. B. *J. Exptl. Theoret. Phys* **1957**, *33*, 1531.

(54) Dubovik, V. M.; Cheshkov, A. A. *Sov. Phys. JETP* **1967**, *24*, 924.

(55) Dubovik, V. M.; Cheshkov, A. A. *Sov J Part Nucl* **1975**, *5*, 318.

(56) Afanasiev, G. N.; Yu, P. S. *Journal of Physics A: Mathematical and General* **1995**, *28*, 4565.

(57) Radescu, E. E.; Vaman, G. *Physical Review E* **2002**, *65*, 046609.

(58) Afanasiev, G. N. *Journal of Physics D: Applied Physics* **2001**, *34*, 539.

(59) Nanz, S. In *Toroidal Multipole Moments in Classical Electrodynamics: An Analysis of their Emergence and Physical Significance*; Springer Fachmedien Wiesbaden: Wiesbaden, 2016, p 5.

(60) Dubovik, V. M.; Tugushev, V. *Toroid moments in electrodynamics and solid-state physics*, 1990; Vol. 187.

(61) Zheludev, I. S.; Perekalina, T. M.; Smirnovskaya, E. M.; Fonton, S. S.; Yarmukhamedov, Y. N. *Pis'ma v Zhurnal Ehksperimental'noj i Teoreticheskoj Fiziki* **1974**, *20*, 289.

(62) Kittel, C. *Physical Review* **1946**, *70*, 965.

(63) Sannikov, D. G.; Zheludev, I. S. *Sov. Phys. Solid State* **1985**, *27*, 826.

(64) Khomskii, D. *Classifying Multiferroics: Mechanisms and Effects*, 2009; Vol. 2.

(65) Aleksandr, P. P.; Anatolii, K. Z. *Physics-Uspekhi* **2012**, *55*, 557.

(66) A Spaldin, N.; Fiebig, M.; Mostovoy, M. *The toroidal moment in condensed-matter physics and its relation to the magnetoelectric effect*, 2008; Vol. 20.

(67) Mettout, B.; Tolédano, P.; Fiebig, M. *Physical Review B* **2010**, *81*, 214417.

(68) Feng, H.-J.; Liu, F.-M. *Chinese Physics B* **2009**, *18*, 2481.

(69) Lemak, S.; Beloglazova, N.; Nocek, B.; Skarina, T.; Flick, R.; Brown, G.; Popovic, A.; Joachimiak, A.; Savchenko, A.; Yakunin, A. F. *Journal of the American Chemical Society* **2013**, *135*, 17476.

(70) Papasimakis, N.; Fedotov, V. A.; Savinov, V.; Raybould, T. A.; Zheludev, N. I. *Nature Materials* **2016**, *15*, 263.

(71) Fernandez-Corbaton, I.; Nanz, S.; Rockstuhl, C. *Scientific Reports* **2017**, *7*, 7527.

(72) Savinov, V.; Fedotov, V. A.; Zheludev, N. I. *Physical Review B* **2014**, *89*, 205112.

(73) Kaelberer, T.; Fedotov, V. A.; Papasimakis, N.; Tsai, D. P.; Zheludev, N. I. *Science* **2010**, *330*, 1510.

(74) Huang, Y.-W.; Chen, W. T.; Wu, P. C.; Fedotov, V. A.; Zheludev, N. I.; Tsai, D. P. *Scientific Reports* **2013**, *3*, 1237.

(75) Bouwkamp, C. J.; Casimir, H. B. G. *Physica* **1954**, *20*, 539.

(76) Thorne, K. S. *Reviews of Modern Physics* **1980**, *52*, 299.

(77) Papasimakis, N.; Fedotov, V. A.; Marinov, K.; Zheludev, N. I. *Physical Review Letters* **2009**, *103*, 093901.

(78) Dong, Z.-G.; Ni, P.; Zhu, J.; Yin, X.; Zhang, X. *Optics Express* **2012**, *20*, 13065.

(79) Ye, Q. W.; Guo, L. Y.; Li, M. H.; Liu, Y.; Xiao, B. X.; Yang, H. L. *Physica Scripta* **2013**, *88*, 055002.

(80) Fan, Y.; Wei, Z.; Li, H.; Chen, H.; Soukoulis, C. M. *Physical Review B* **2013**, *87*, 115417.

(81) Ding, C.; Jiang, L.; Sun, C.; Wu, L.; Xu, D.; Zhang, G.; Yao, J. *physica status solidi (b)* **2015**, *252*, 1388.

(82) Ögüt, B.; Talebi, N.; Vogelgesang, R.; Sigle, W.; van Aken, P. A. *Nano Letters* **2012**, *12*, 5239.

(83) Totero Gongora, J. S.; Miroshnichenko, A. E.; Kivshar, Y. S.; Fratalocchi, A. *Nature Communications* **2017**, *8*, 15535.

(84) Fedotov, V. A.; Rogacheva, A. V.; Savinov, V.; Tsai, D. P.; Zheludev, N. I. *Scientific Reports* **2013**, *3*, 2967.

(85) Weiland, T.; Timm, M.; Munteanu, I. *IEEE Microwave Magazine* **2008**, *9*, 62.

(86) Tonouchi, M. *Nature Photonics* **2007**, *1*, 97.

(87) Ferguson, B.; Zhang, X.-C. *Nature Materials* **2002**, *1*, 26.

(88) Fattinger, C.; Grischkowsky, D. *Applied Physics Letters* **1989**, *54*, 490.

(89) Fattinger, C.; Grischkowsky, D. *Applied Physics Letters* **1988**, *53*, 1480.

(90) Nahata, A.; Weling, A. S.; Heinz, T. F. *Applied Physics Letters* **1996**, *69*, 2321.

(91) Rice, A.; Jin, Y.; Ma, X. F.; Zhang, X. C.; Bliss, D.; Larkin, J.; Alexander, M. *Applied Physics Letters* **1994**, *64*, 1324.

(92) Krozer, V.; Loata, G.; Fuente, J. G. d. l.; Sanz, P. In *Proceedings, IEEE Tenth International Conference on Terahertz Electronics* 2002, p 109.

(93) Valentine, J.; Zhang, S.; Zentgraf, T.; Ulin-Avila, E.; Genov, D. A.; Bartal, G.; Zhang, X. *Nature* **2008**, *455*, 376.

(94) Landy, N. I.; Sajuyigbe, S.; Mock, J. J.; Smith, D. R.; Padilla, W. J. *Physical Review Letters* **2008**, *100*, 207402.

(95) Zheludev, N. I.; Kivshar, Y. S. *Nature Materials* **2012**, *11*, 917.

(96) Dubovik, V. M.; Tugushev, V. V. *Physics Reports* **1990**, *187*, 145.

(97) Naumov, I. I.; Bellaiche, L.; Fu, H. *Nature* **2004**, *432*, 737.

(98) Ceulemans, A.; Chibotaru, L. F.; Fowler, P. W. *Physical Review Letters* **1998**, *80*, 1861.

(99) Guo, L.-Y.; Li, M.-H.; Huang, X.-J.; Yang, H.-L. *Applied Physics Letters* **2014**, *105*, 033507.

(100) Li, H.-m.; Xue, F. *Journal of Applied Physics* **2017**, *122*, 044501.

(101) Marinov, K.; Boardman, A. D.; Fedotov, V. A.; Zheludev, N. *New Journal of Physics* **2007**, *9*, 324.

(102) Sawada, K.; Nagaosa, N. *Physical Review Letters* **2005**, *95*, 237402.

(103) Basharin, A. A.; Kafesaki, M.; Economou, E. N.; Soukoulis, C. M.; Fedotov, V. A.; Savinov, V.; Zheludev, N. I. *Physical Review X* **2015**, *5*, 011036.

(104) Schurig, D.; Mock, J. J.; Smith, D. R. *Applied Physics Letters* **2006**, *88*, 041109.

(105) Ordal, M. A.; Long, L. L.; Bell, R. J.; Bell, S. E.; Bell, R. R.; Alexander, R. W.; Ward, C. A. *Appl. Opt.* **1983**, *22*, 1099.

(106) Grischkowsky, D.; Keiding, S.; van Exter, M.; Fattinger, C. *Journal of the Optical Society of America B* **1990**, *7*, 2006.

(107) Luk'yanchuk, B.; Zheludev, N. I.; Maier, S. A.; Halas, N. J.; Nordlander, P.; Giessen, H.; Chong, C. T. *Nature Materials* **2010**, *9*, 707.

(108) Singh, R.; Al-Naib, I. A. I.; Koch, M.; Zhang, W. *Optics Express* **2011**, *19*, 6312.

(109) Singh, R.; Cao, W.; Al-Naib, I.; Cong, L.; Withayachumnankul, W.; Zhang, W. *Ultrasensitive THz sensing with high-Q Fano resonances in metasurfaces*, 2014; Vol. 105.

(110) Pendry, J. B.; Holden, A. J.; Robbins, D. J.; Stewart, W. J. *IEEE Transactions on Microwave Theory and Techniques* **1999**, *47*, 2075.

(111) Fedotov, V. A.; Rose, M.; Prosvirnin, S. L.; Papasimakis, N.; Zheludev, N. I. *Physical Review Letters* **2007**, *99*, 147401.

(112) Fano, U. *Physical Review* **1961**, *124*, 1866.

(113) Li, Z.; Cakmakyapan, S.; Butun, B.; Daskalaki, C.; Tzortzakis, S.; Yang, X.; Ozbay, E. *Optics Express* **2014**, *22*, 26572.

(114) Hao, F.; Sonnefraud, Y.; Dorpe, P. V.; Maier, S. A.; Halas, N. J.; Nordlander, P. *Nano Letters* **2008**, *8*, 3983.

(115) Cao, Y. P.; Wang, Y. Y.; Geng, Z. X.; Liu, J.; Yang, Y. P.; Chen, H. D. *Journal of Applied Physics* **2015**, *117*, 063107.

(116) Sun, L.; Ma, T.; Yang, S.-C.; Kim, D.-K.; Lee, G.; Shi, J.; Martinez, I.; Yi, G.-R.; Shvets, G.; Li, X. *Nano Letters* **2016**, *16*, 4322.

(117) Shafiei, F.; Monticone, F.; Le, K. Q.; Liu, X.-X.; Hartsfield, T.; Alù, A.; Li, X. *Nature Nanotechnology* **2013**, *8*, 95.

(118) Panaro, S.; Nazir, A.; Proietti Zaccaria, R.; Razzari, L.; Liberale, C.; De Angelis, F.; Toma, A. *Nano Letters* **2015**, *15*, 6128.

(119) Raybould, T.; Fedotov, V.; Papsimakis, N.; Youngs, I.; Chen, W. T.; Tsai, D. P.; Zheludev, N. In *CLEO: 2015*; Optical Society of America: San Jose, California, 2015, p FM1C.5.

(120) Miroshnichenko, A. E.; Evlyukhin, A. B.; Yu, Y. F.; Bakker, R. M.; Chipouline, A.; Kuznetsov, A. I.; Luk'yanchuk, B.; Chichkov, B. N.; Kivshar, Y. S. *Nature Communications* **2015**, *6*, 8069.

(121) Cong, L.; Manjappa, M.; Xu, N.; Al-Naib, I.; Zhang, W.; Singh, R. *Advanced Optical Materials* **2015**, *3*, 1537.

(122) Chen, T.; Li, S.; Sun, H. *Sensors* **2012**, *12*, 2742.

(123) Liu, C.; Agarwal, K.; Zhang, Y.; Chowdhury, D. R.; Azad, A. K.; Cho, J.-H. *Advanced Optical Materials* **2016**, *4*, 1302.

(124) Metzger, B.; Hentschel, M.; Schumacher, T.; Lippitz, M.; Ye, X.; Murray, C. B.; Knabe, B.; Buse, K.; Giessen, H. *Nano Letters* **2014**, *14*, 2867.

(125) Xu, N.; Singh, R.; Zhang, W. *Applied Physics Letters* **2016**, *109*, 021108.

(126) Yen, T. J.; Padilla, W. J.; Fang, N.; Vier, D. C.; Smith, D. R.; Pendry, J. B.; Basov, D. N.; Zhang, X. *Science* **2004**, *303*, 1494.

(127) Grigorenko, A. N.; Geim, A. K.; Gleeson, H. F.; Zhang, Y.; Firsov, A. A.; Khrushchev, I. Y.; Petrovic, J. *Nature* **2005**, *438*, 335.

(128) Rosenblatt, G.; Orenstein, M. *Physical Review Letters* **2015**, *115*, 195504.

(129) Petschulat, J.; Menzel, C.; Chipouline, A.; Rockstuhl, C.; Tünnermann, A.; Lederer, F.; Pertsch, T. *Physical Review A* **2008**, *78*, 043811.

(130) Liu, Z.; Du, S.; Cui, A.; Li, Z.; Fan, Y.; Chen, S.; Li, W.; Li, J.; Gu, C. *Advanced Materials* **2017**, *29*, 1606298.

(131) Basharin, A. A.; Chuguevsky, V.; Volsky, N.; Kafesaki, M.; Economou, E. N. *Physical Review B* **2017**, *95*, 035104.

(132) Raybould, T. A.; Fedotov, V. A.; Papasimakis, N.; Kuprov, I.; Youngs, I. J.; Chen, W. T.; Tsai, D. P.; Zheludev, N. I. *Physical Review B* **2016**, *94*, 035119.

(133) Tao, H.; Strikwerda, A. C.; Liu, M.; Mondia, J. P.; Ekmekci, E.; Fan, K.; Kaplan, D. L.; Padilla, W. J.; Zhang, X.; Averitt, R. D.; Omenetto, F. G. *Applied Physics Letters* **2010**, *97*, 261909.

(134) Soukoulis, C. M.; Kafesaki, M.; Economou, E. N. *Advanced Materials* **2006**, *18*, 1941.

(135) Dayal, G.; Solanki, A.; Chin, X. Y.; Sum, T. C.; Soci, C.; Singh, R. *Journal of Applied Physics* **2017**, *122*, 073101.

(136) Boltasseva, A.; Atwater, H. A. *Science* **2011**, *331*, 290.

(137) Singh, R.; Al-Naib, I.; Cao, W.; Rockstuhl, C.; Koch, M.; Zhang, W. *IEEE Transactions on Terahertz Science and Technology* **2013**, *3*, 820.

(138) Al-Naib, I.; Hebestreit, E.; Rockstuhl, C.; Lederer, F.; Christodoulides, D.; Ozaki, T.; Morandotti, R. *Physical Review Letters* **2014**, *112*, 183903.

(139) Ye, D.; Chang, K.; Ran, L.; Xin, H. *Nature Communications* **2014**, *5*, 5841.

(140) Liu, N.; Tang, M. L.; Hentschel, M.; Giessen, H.; Alivisatos, A. P. *Nature Materials* **2011**, *10*, 631.

(141) Cubukcu, E.; Zhang, S.; Park, Y.-S.; Bartal, G.; Zhang, X. *Applied Physics Letters* **2009**, *95*, 043113.

(142) Driscoll, T.; Palit, S.; Qazilbash, M. M.; Brehm, M.; Keilmann, F.; Chae, B.-G.; Yun, S.-J.; Kim, H.-T.; Cho, S. Y.; Jokerst, N. M.; Smith, D. R.; Basov, D. N. *Applied Physics Letters* **2008**, *93*, 024101.

(143) Lee, S. H.; Choi, J.; Kim, H.-D.; Choi, H.; Min, B. *Scientific Reports* **2013**, *3*, 2135.

(144) Xu, X.; Peng, B.; Li, D.; Zhang, J.; Wong, L. M.; Zhang, Q.; Wang, S.; Xiong, Q. *Nano Letters* **2011**, *11*, 3232.

(145) Liu, X.; MacNaughton, S.; Shrekenhamer, D. B.; Tao, H.; Selvarasah, S.; Totachawattana, A.; Averitt, R. D.; Dokmeci, M. R.; Sonkusale, S.; Padilla, W. J. *Applied Physics Letters* **2010**, *96*, 011906.

(146) Gupta, M.; Singh, R. *Advanced Optical Materials* **2016**, *4*, 2119.

(147) O'Hara, J. F.; Singh, R.; Brener, I.; Smirnova, E.; Han, J.; Taylor, A. J.; Zhang, W. *Optics Express* **2008**, *16*, 1786.

(148) Li, J.; Tian, Z.; Chen, Y.; Cao, W.; Zeng, Z. *Appl. Opt.* **2012**, *51*, 3258.

(149) Reinhard, B.; Schmitt, K. M.; Wollrab, V.; Neu, J.; Beigang, R.; Rahm, M. *Applied Physics Letters* **2012**, *100*, 221101.

(150) Ng, B.; Hanham, S. M.; Giannini, V.; Chen, Z. C.; Tang, M.; Liew, Y. F.; Klein, N.; Hong, M. H.; Maier, S. A. *Optics Express* **2011**, *19*, 14653.

(151) Schneider, A.; Stillhart, M.; Günter, P. *Optics Express* **2006**, *14*, 5376.

(152) Vidal, S.; Degert, J.; Tondusson, M.; Freysz, E; Oberlé, J. *Journal of the Optical Society of America B* **2014**, *31*, 149.

(153) Zhang, J; Hong, Y; Braunstein, S. L. *IEE Proceedings - Optoelectronics* **2004**, *151*, 98.

(154) Charipar, N. A; Kim, H; Mathews, S. A; Piqué, A. AIP Advances **2016**, *6*, 015113.

(155) G N Afanasiev, G. N.; Stepanovsky, Y. P. Journal of Physics A: Mathematical and General **1995**, *28*, 4565.

(156) Krishnamurthy, S.; Reiten, M. T.; Harmon, S. A.; Cheville, R. A. *Applied Physics Letters* **2001**, 79, 875.

(157) Randall, C. M.; Rawcliffe, R. D. *Applied Optics* **1967**, *6*, 1889-1895.

(158) Azad A. K.; Zhao, Y.; Zhang, W. *Applied Physics Letters* **2005**, *86*, 141102.

(159) Sang, B. H.; Jeon, Tea-In. *Optics Express* **2016**, *24*, 29040.